Calhoun
Institutional Archive of the Naval Postgraduate School

Calhoun: The NPS Institutional Archive

DSpace Repository

Theses and Dissertations 1. Thesis and Dissertation Collection, all items

2006-12

Effect of internal solitary waves on mine detection in the western Philippine Sea east of Taiwan

Hsieh, Chung-Ping

Monterey, California. Naval Postgraduate School

---

http://hdl.handle.net/10945/2446

Downloaded from NPS Archive: Calhoun

DUDLEY
KNOX
LIBRARY

Calhoun is a project of the Dudley Knox Library at NPS, furthering the precepts and goals of open government and government transparency. All information contained herein has been approved for release by the NPS Public Affairs Officer.

Dudley Knox Library / Naval Postgraduate School
411 Dyer Road / 1 University Circle
Monterey, California USA 93943

http://www.nps.edu/library

NAVAL POSTGRADUATE SCHOOL

MONTEREY, CALIFORNIA

THESIS

EFFECT OF INTERNAL SOLITARY WAVES ON MINE DETECTION IN THE WESTERN PHILIPPINE SEA EAST OF TAIWAN

by

Hsieh, Chung-Ping

December 2006

Thesis Advisor:	Peter C. Chu
Second Reader:	Melvin D. Wagstaff

Approved for public release; distribution is unlimited

THIS PAGE INTENTIONALLY LEFT BLANK

REPORT DOCUMENTATION PAGE

Form Approved OMB No. 0704-0188

Public reporting burden for this collection of information is estimated to average 1 hour per response, including the time for reviewing instruction, searching existing data sources, gathering and maintaining the data needed, and completing and reviewing the collection of information. Send comments regarding this burden estimate or any other aspect of this collection of information, including suggestions for reducing this burden, to Washington headquarters Services, Directorate for Information Operations and Reports, 1215 Jefferson Davis Highway, Suite 1204, Arlington, VA 22202-4302, and to the Office of Management and Budget, Paperwork Reduction Project (0704-0188) Washington DC 20503.

1. AGENCY USE ONLY ***(Leave blank)***	**2. REPORT DATE** December 2006	**3. REPORT TYPE AND DATES COVERED** Master's Thesis

4. TITLE AND SUBTITLE Effect of Internal Solitary Waves on Mine Detection in the Western Philippine Sea East of Taiwan

5. FUNDING NUMBERS

6. AUTHOR(S) Hsieh, Chung-Ping

7. PERFORMING ORGANIZATION NAME(S) AND ADDRESS(ES)
Naval Postgraduate School
Monterey, CA 93943-5000

8. PERFORMING ORGANIZATION REPORT NUMBER

9. SPONSORING /MONITORING AGENCY NAME(S) AND ADDRESS(ES)
N/A

10. SPONSORING/MONITORING AGENCY REPORT NUMBER

11. SUPPLEMENTARY NOTES The views expressed in this thesis are those of the author and do not reflect the official policy or position of the Department of Defense or the U.S. Government.

12a. DISTRIBUTION / AVAILABILITY STATEMENT
Approved for public release; distribution is unlimited.

12b. DISTRIBUTION CODE

13. ABSTRACT (maximum 200 words)

Upper layer temperature in the western Philippine Sea near Taiwan was sampled using a coastal monitoring buoy with fifteen thermistors attached from July 28–August 7, 2005. Internal waves and internal solitons (IS) were identified using the empirical orthogonal function analysis. Without the IW and IS, the power spectra, structure functions, and singular measures (representing the intermittency) of the temperature field satisfy the power law with multi-scale characteristics at all depths. The IW does not change the basic characteristics of the multifractal structure. However, the IS changes the power exponent of the power spectra drastically, especially in the low wave number domain. It breaks down the power law of the structure function and increases the intermittency parameter. The physical mechanisms causing these different effects need to be further explored further.

The Comprehensive Acoustic Simulation System was applied to determine how the IS affect the mine detection by computing the transmission loss (TL) and the ray traces of range-dependent and range-independent cases during the IS period. The maximum TL difference is 20 dB. As a result, the mine detection probability will dramatically be reduced to 1% of the original detection probability.

14. SUBJECT TERMS: Western Philippine Sea, Internal Waves, Internal Solitary Waves, Mine Detection, Multi-Fractal Characteristics, Power Spectra, Structure Function, Singular Measures, Comprehensive Acoustic Simulation, CASS/GRAB model.

15. NUMBER OF PAGES 138

16. PRICE CODE

17. SECURITY CLASSIFICATION OF REPORT Unclassified	**18. SECURITY CLASSIFICATION OF THIS PAGE** Unclassified	**19. SECURITY CLASSIFICATION OF ABSTRACT** Unclassified	**20. LIMITATION OF ABSTRACT** UL

NSN 7540-01-280-5500

Standard Form 298 (Rev. 2-89)
Prescribed by ANSI Std. 239-18

THIS PAGE INTENTIONALLY LEFT BLANK

Approved for public release; distribution is unlimited.

EFFECT OF INTERNAL SOLITARY WAVES ON MINE DETECTION IN THE WESTERN PHILIPPINE SEA EAST OF TAIWAN

Chung-Ping Hsieh
Lieutenant, R.O.C. Taiwan Navy
B.A., R.O.C. Naval Academy, 1998

Submitted in partial fulfillment of the
requirements for the degree of

MASTER OF SCIENCE IN PHYCSICAL OCEANOGRAPHY

from the

NAVAL POSTGRADUATE SCHOOL
December 2006

Author:	Hsieh, Chung-Ping
Approved by:	Peter C. Chu Thesis Advisor
	Melvin D. Wagstaff Second Reader
	Mary L. Batteen Chairman, Department of Oceanography

THIS PAGE INTENTIONALLY LEFT BLANK

ABSTRACT

Upper layer temperature in the western Philippine Sea near Taiwan was sampled using a coastal monitoring buoy with fifteen thermistors attached from July 28–August 7, 2005. Internal waves and internal solitons were identified using the empirical orthogonal function analysis. Without the IW and IS, the power spectra, structure functions, and singular measures (representing the intermittency) of the temperature field, satisfy the power law with multi-scale characteristics at all depths. The IW does not change the basic characteristics of the multifractal structure. However, the IS changes the power exponent of the power spectra drastically, especially in the low wave number domain. It breaks down the power law of the structure function and increases the intermittency parameter. The physical mechanisms causing these different effects need to be explored further.

The Comprehensive Acoustic Simulation System was applied to determine how the IS affect the mines detection by computing the transmission loss (TL) and the ray traces of range-dependent and range-independent cases during the IS period. The maximum TL difference is 20 dB. As a result, the mine detection probability will dramatically be reduced to 1% of the original detection probability.

THIS PAGE INTENTIONALLY LEFT BLANK

TABLE OF CONTENTS

LIST OF FIGURES

THIS PAGE INTENTIONALLY LEFT BLANK

LIST OF TABLES

THIS PAGE INTENTIONALLY LEFT BLANK

ACKNOWLEDGMENTS

First, I dedicate this thesis to my parents, especially my father who was the most influential person in my life during my formative years. He taught me to be a considerate, a leader, a thinker, and a friend. I miss you very much.

Second, I would like to thank my sisters and brother-in-law who take care of my mom. Without their love, help, and understanding, I could not have accomplished my studies at NPS.

Finally, I thank Professor Peter Chu for his patience, guidance, encouragement, and insight through the entire process and Mr. Melvin. Wagstaff for helping me deal with the CASS/GRAB Model, acoustics, and mine warfare problems. Mr. Chenwu Fan and Dr. Sunhyea Park I thank for their assistance in Matlab programming. I also extend heartfelt gratitude to all members in the Naval Ocean Analysis and Prediction Laboratory (NOAP). Their hospitality and hard work encouraged my interest in academic work.

THIS PAGE INTENTIONALLY LEFT BLANK

I. INTRODUCTION

During the Cold War, the United States Navy and the Soviet Navy were the blue water Navies. They expended most of their efforts toward building their ships' weapons systems, sensors and electronic countermeasures to be suitable for operation in the deep ocean. After the Cold War with suffering three major combat ships' casualties by mines in the littoral region, the Persian Gulf, the U.S. Navy learned a lesson about the importance of operations in the littoral region and they then shifted their budget into researching and developing the new weapons systems, sensors and countermeasure technologies effective in those areas.

While many countries are still pouring a lot of money to build a blue water Navy, the significance of the littoral region for homeland defense is recognized. The People's Liberation Army-Navy (PLA-Navy) of China aims to develop itself into a true blue-water Navy that can project power beyond the first island chain (Aleutians, Kuriles, Ryukyus, Taiwan, Philippines and Great Sunda Islands) in the early 21st century. The PLA-Navy's new strategic threats include a possible conflict with the United States and Japan over Taiwan, as well as other potential conflicts with China's neighbors over disputed territories in the East and the South China Sea. By 2020 the PLA-Navy may deploy a naval force with regional capabilities second only to the U.S and Japan in East Asia. The Republic of China (R.O.C), Taiwan, has been under threat from China for many years and it still exists. The geographic gap between the two is just a continental shelf covered by shallow water, the Taiwan Strait. The PLA-Navy is rapidly increasing its size by building new modern combat ships and submarines and gaining new technology and weapons, in order to balance the power of the United States. But they have not forgotten to make a threat on the nearby countries of R.O.C Taiwan and Japan in this littoral region. The threat comes mainly from the new technology diesel submarines and all kinds of mines.

Sensors, ships' platforms, and the tactics used in the deep ocean are designed for the acoustically range-independent environment. In the shallow littoral region, with its reverberation limitation, surface and bottom, and more complicated ocean environment than in the deep ocean, the range-dependent methods are adopted.

The new modern submarines, with their combination of improvements in noise reduction technology and Air Independent Propulsion (AIP), are very quiet and can stay under the ocean even longer than before. It is more and more difficult to use only hull-mounted sonar to detect and then force a submarine to surface. The PLA-Navy received two 877EKM and two 636 Kilo class diesel-electric submarines (Figure 1) from Russia in 1994 and 1996. These submarines are deployed in the PLA East Sea Fleet based at Zhoushan, Zhejiang. In 2002, the PLA-Navy ordered an additional eight 636M Kilo class submarines. The purchase of the additional Kilo class submarines reflects the PLA-Navy's urgency to build a modernized underwater force that is capable of supporting its military actions against Taiwan and deterring any intervention by the U.S Navy. Deliberate submarine activities that linger in the South China Sea, the East coast of Taiwan, the Philippine Sea and the East China Sea deliberately are reported more frequently. This causes the instability of the regional peace and increasing military tension between China and other countries.

Figure 1. The PLA Navy's Project 636 Kilo class diesel-electric submarine is regarded as one of the world's quietest conventional submarines. (From www. SinoDefence.com)

Mines are relatively cheaper, easily acquired by any nation in mass quantities, and not as sophisticated as torpedoes. Mines are designed to operate through the water column, either on the surface (floating mines), at various depths, or on the bottom (anchored mines). They can easily be deployed in any water by ships, by planes or even by submarines. Once deployed, they become very difficult to retrieve. The floating contact mines are the simplest ones. These mines float freely with currents and are very dangerous to all surface ships, not only to the opponent's combat ships, but also to merchant ships that pass through these uncertain waters. These mines usually need to be detected visually and cleared by the minesweepers and Explosive Ordnance Disposal (EOD) units. A more complex type of mine is the modern Influence Mine (Figure 2) that can be activated by magnetic anomaly, water pressure difference, and acoustic wave anomaly. The low target strength of sea mines requires sonar with higher frequencies than those used in submarine detection. The influences mines usually anchor to the ocean floor and tether at various depths in the water, or sit on the bottom making detection much more difficult.

(a) (b)

Figure 2. (a) M-2 moored mines carried by surface ships designed to block seaport and routes to attack ships. (b) M-4 acoustic moored mine has strong resistance to the background noise and is designed to attack medium sized surface ships and submarines. (From SinoDefence.com)

The PLA-Navy is well prepared to conduct offensive and defensive mining operations within its coastal seas, the Yellow Sea, the East China Sea, the Taiwan Strait, and the South China Sea, and has a large inventory of mines available, including older Soviet-supplied mines and domestically produced versions of these. Most PLA-Navy surface ships are equipped with mine rails and are capable of laying mines as a secondary mission. The PLA-Navy is working on improving its mine warfare capabilities through the development and acquisition of new technology that includes rocket propulsion and radio detonation to enhance targeting. It is also working on training exercises using surface ships, submarines, and aircraft in coastal areas in order to be well-prepared to conduct both mine-laying and minesweeping operations in these areas.

The PLA-Navy submarines can lay mines today (Figure 3). This stand-off capability will improve survivability and could enable the PLA-Navy to maintain a minefield against opposing forces seeking to clear channels through the field, depending on the antisubmarine warfare (ASW) capabilities of the opposition.

Figure 3. The PLA-Navy's EM52 (T-1) is a submarine laid fast-rising rocket-propelled bottom mine. It is laid in the sea bottom and will rise to the surface using its rocket propulsion and without guidance. (From SinoDefence.com)

Both the modern traditional diesel submarines and the cheaper and easily deployed mines in the littoral region are all related to the sonar detection. Active Mid Frequency (MF) and High Frequency (HF) sonar systems, active and passive towed array sonar, and the Unmanned Undersea Vehicles (UUVs) are the new state-of- the-art of methods to counter the diesel submarines and the mines. HF sonar can have higher resolution images to distinguish the mines from the objects under the sea. Towed side scan sonar and UUVs can extend the hull mounted sonar detection range and keep the Navy ships far away from uncertain dangerous mine zones to avoid direct damage. After locating the mines in the water from the UUV's video images, clearance of the mines becomes relatively easier.

Nonlinear internal solitons (IS) are often observed in coastal oceans with large displacement of pycnocline that changes the temperature field and in turn affects the acoustic propagation. The ISWs' effect on sound propagation has been investigated extensively in the continental shelves such as the Yellow Sea (Zhou et al., 1991) and north of Lisbon (Rodriguez et al., 1998) and the East China Sea during the Asian Seas International Acoustics Experiment (ASIAEX) (Dahl et al., 2004), and along and across the shelfbreak such as the South China Sea during ASIAEX (Lynch et al., 2004). Zhou et al. (1991) claimed that ISW could be an important loss mechanism for shallow water sound propagation. However, Rodriguez et al. (2000) showed that ISW causes successive signal attenuation and signal increase (called acoustic focusing).

In this thesis, the internal solitons were indentified in the western Philippine Sea by the thermistors chain attached under the Costal Monitoring Buoy (CMB) from the U.S Navy in July2005. After analyzing the data and comparing the two periods with wave and without wave via the structure function, and singular measures, the model were applied.

The U.S Navy standard MF and HF acoustic model for range-dependent propagation, the Comprehensive Acoustic Simulation System (CASS), use the Gaussian Ray Bundle (GRAB) eigenray model and operates in the 600 Hz to 100 kHz frequency range. This reverberation model works well in modeling in a range-dependent environment and in its ability to predict acoustic performance of the signal excess (SE) in the littoral regions when given accurate inputs of the wind speed, bottom type and in situ measurements of bathymetry and sound speed profiles.

It is costly both in time and budget, and dangerous to deploy ships to unknown littoral waters to operate under the threat of mines and submarines. The CASS/GRAB model is then applied to the U.S. Navy to model the ocean acoustic wave propagation in designated waters to get better theater scenario before the sea operation. The R.O.C Taiwan Navy is also under the threat of mines in the ocean around the islands, especially the passages of the main harbors. The Navy ocean data bank is abundant with all kinds of ocean data collected not only from the Navy research ships but also from the National and University research ships. If combined with the CASS/GRAB model, the R.O.C. Taiwan Navy will have huge improvements in the prediction of acoustic propagation when applied to mine hunting and submarine detection. In this thesis, the CASS/GRAB model was also applied to determine how the internal solitary wave affects the acoustic wave propagation.

In Chapter II, the description of the western Philippine Sea oceanography is discussed. The details of collecting data from the thermistor chains and the CMB are described in Chapter III. The data analysis via the structure function and singular measures and the comparison are given in Chapter IV. In Chapter V, the CASS/GRAB has detailed descriptions as well as the input parameters applied to the model. In chapter VI, the comparison between the range-dependent and the range-independent cases are determined to see how the internal solitons affect the transmission loss in acoustic wave propagation. The mine's and submarine's target strength determination and detection applications are discussed in Chapter VII. The final conclusions are listed in Chapter VIII.

II. ENVIRONMENT OF THE WESTERN PHILIPPINE SEA

A. GEOLOGY AND TOPOGRAPHY

The West Philippine Sea (WPS) (Figures 4 and 5) is a part of the western boundary of the western Pacific Ocean, lying southeast of Taiwan and northeast of the Philippines, and is composed of the Shikoku Basin, the West Mariana Basin and the Philippine Basin. The sea floor was formed by the tectonic activity of the Philippine Plate subducting to the Eurasian Plate. Between these two plates, geologic faults and fracture zones, the Philippine trench, and ridges, the Philippine archipelago was formed.

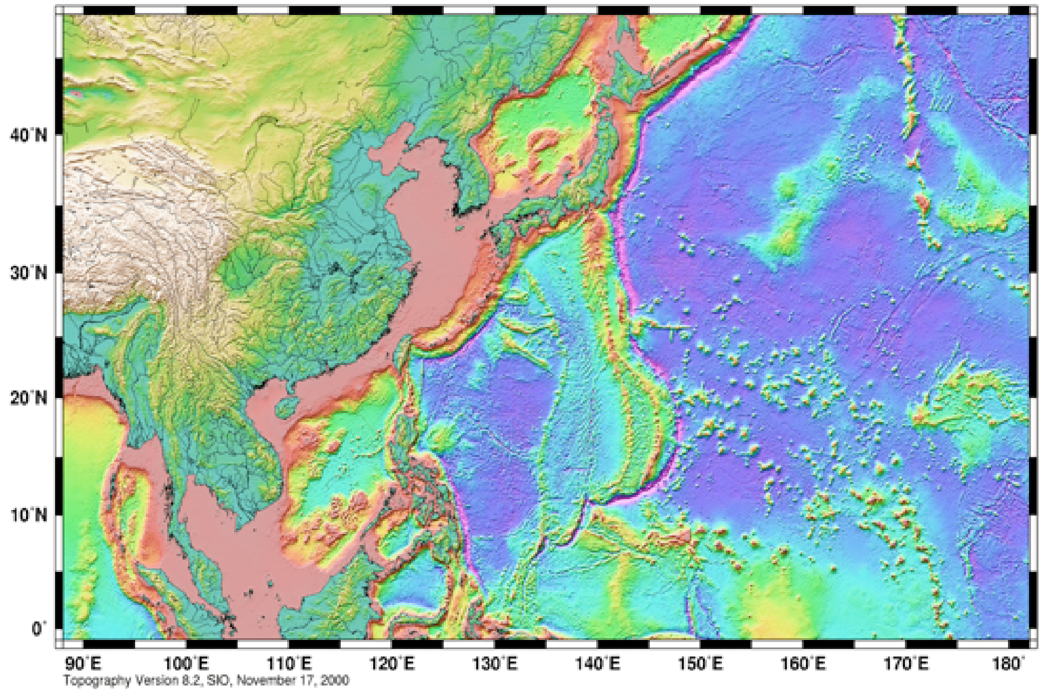

Figure 4. The geography and bathymetry of East Asia and the western Pacific Area.

The composition of the water in the Philippine Sea can be divided into three water layer regimes (Ikuo, Kaneko, 2001 et. al) (Figure 6), the intermediate layer (above 500 dbar), the deep layer (1500 dbar) and the bottom layer (3500 dbar). The intermediate layer of water comes mainly from the North Pacific Intermediate water (NPIW) at 20°N and 26°N and the North Equatorial Current (NEC), and part of the Antarctic Intermediate

Water (AAIW) extends farther north through the northward flowing Mindanao Undercurrent (MUC) and joins the Kuroshio Current (KC). The dominant water in the intermediate layer is the persistent yearly westward Pacific North Equatorial Current, and it bifurcates into the southward flowing Mindanao Current (MC) and the northward flowing KC (Black Stream).

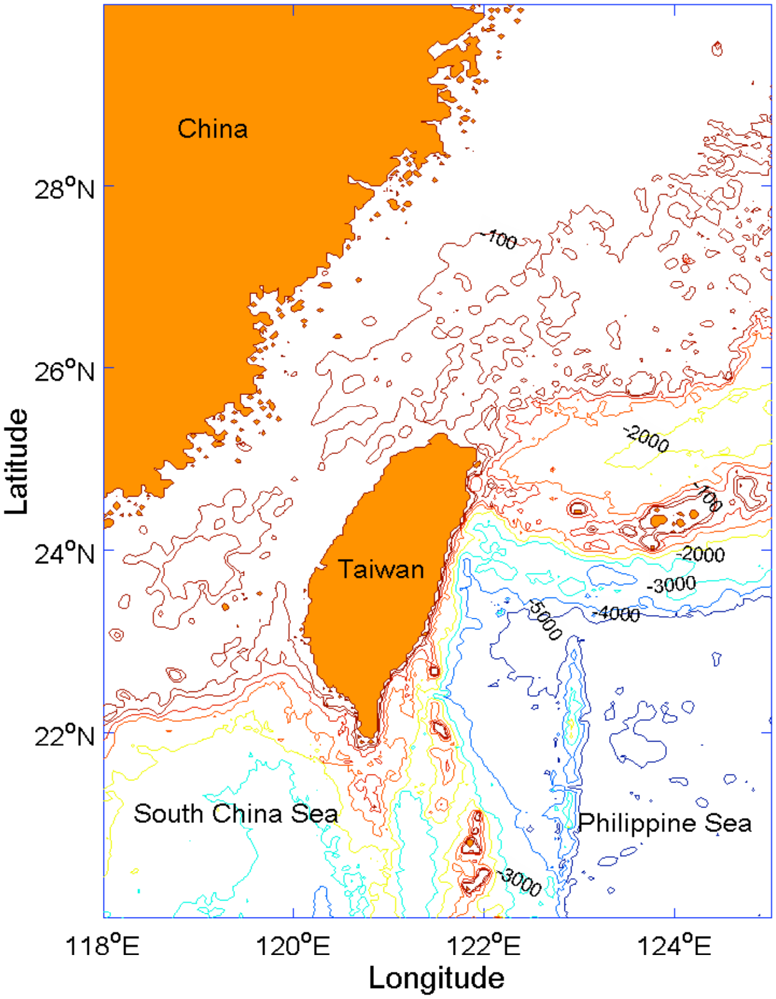

Figure 5. Topography of the western Philippine Sea and surrounding area.

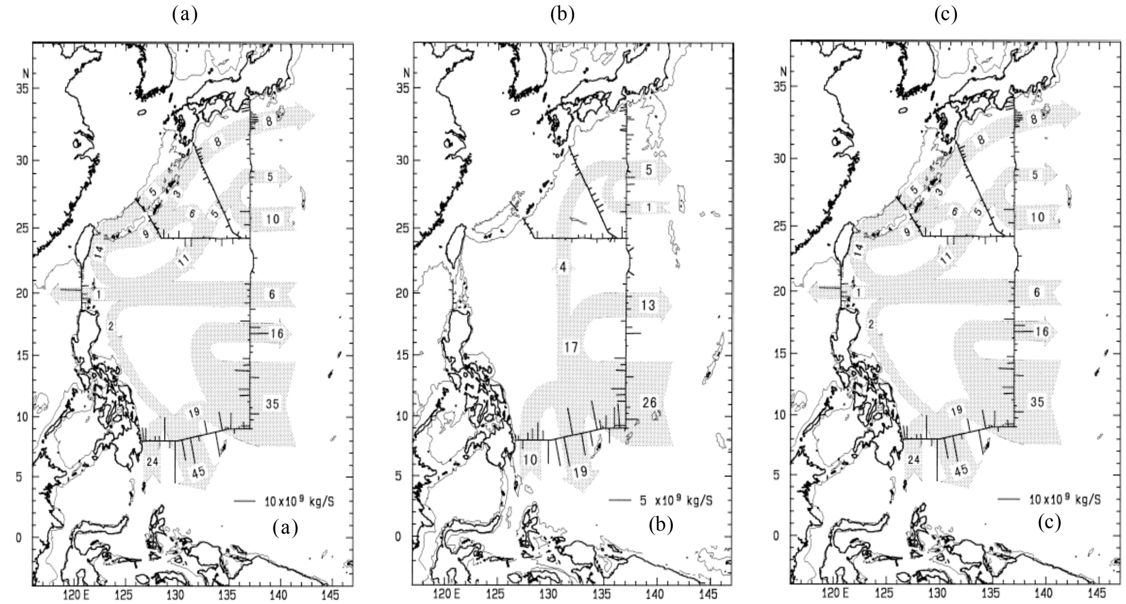

Figure 6. The West Philippine Sea water inputs in (a) the intermediate layer, (b) the deep layer and (c) the bottom area. (From Ikuo et al., 2001)

The well-formed western boundary, KC, brings warm, salty, high oxygen equator water that flows through the northeast of the Philippines, the east coast of Taiwan, Ryukyu Island and then southeast of Japan. Before reaching Taiwan, the Kuroshio encounters the Luzon strait, which is the deepest passage from the Pacific Ocean to the South China Sea, and intrudes, as an anticyclone loop, a warm-core eddy (WCC), the Kuroshio loop or Kuroshio intrusion into the northeast of the South China Sea. The intrusion is intensified in winter due to the dry and cold northeast monsoon from November to March and ceases by late spring when the South China Sea water enters this region due to the southwest monsoon from June to October. The South China Sea water has also been reported to flow out from Luzon Strait and enters into the West Philippines Sea. The outflowing South China Sea water flows only a short distance then is blocked by the northward flowing Kuroshio Current.

The major difference between deep layer water and intermediate water is the lack of the NPIW at 20°N. There are two inflows that are NEC from the North Pacific Deep Water (NPDW) in the Eastern Pacific and deep water from the South Pacific Ocean that enters into the Philippine Sea and run in a clockwise gyre flow out the Philippine Sea at

15°N. The bottom layer water is similar to the deep water layer in that the inflows are in the south and the outflows are in the north part of the Western Philippine Sea.

B. OCEANOGRAPHY

The sea surface temperature (Figure 7) of the WPS is highly affected by the southwest and northeast monsoons in different seasons and the surface water circulation. During winter, the southward flowing colder and fresher water collides with the warmer water from the south. The mixing of the cold and warm water results in relatively cooler water temperature in the WPS. During summer, the colder water from the north is diminished. The WPS is covered with warmer equatorial water as high as 32.85°C.

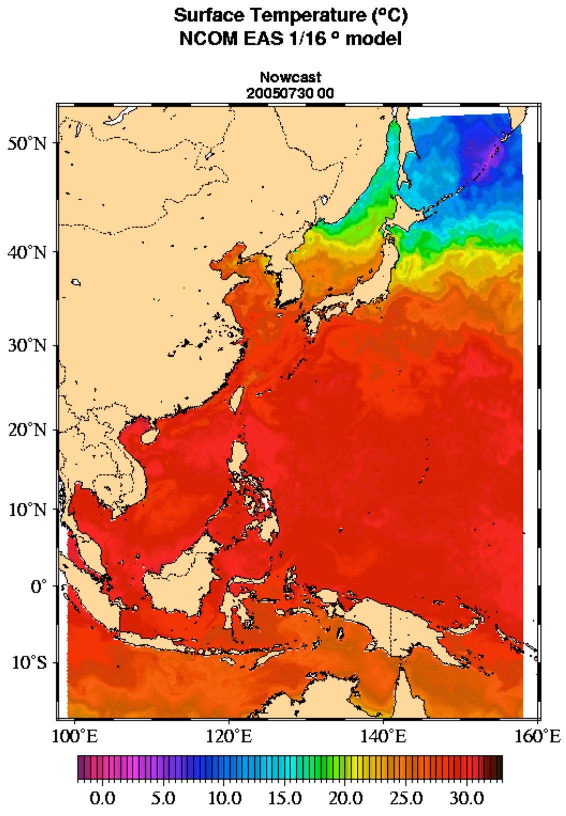

Figure 7. The Sea Surface Temperature during the internal solitary event in the West Philippine Sea. (From Naval Research Laboratory- Stennis Space Center)

The North Tropical Water (NPTW) is characterized by high salinity (34.75 < S < 35.25 psu) and high oxygen concentration (>4.0 ml/l) as a result of excessive evaporation

(Qu et al. 1998). The water extends westward from its formation area in the NEC. The southward flowing MC is identified as maximum salinity (>35.25 psu) with homogeneous oxygen concentration (~3.3 ml/l) and extends into the Celebes Sea. The dominant water, NPIW, in the northern WPS has salinity (< 34.4 psu) and oxygen concentration ($2.5< O_2 < 3$ ml/l). The typical WPS water near the surface has relatively higher salinity than the water near the surface in the South China Sea (Figure 8). The salinity maximum (S_{max}) and minimum (S_{min}) are more distinctive in the WPS. The maximum salinity water has higher potential temperature, and the minimum salinity water has lower potential temperature. The strong NPIW (near the S_{min}) enters into SCS along the northern part of Luzon at the intermediate layer. The intermediate water in the SCS flows out to the WPS along the southern coast of Taiwan after being blocked by the KC. The outflowing SCS water forms the western part of the KC, along the east coast of Taiwan, at intermediate depth, and has relatively higher minimum salinity (S_{min}).

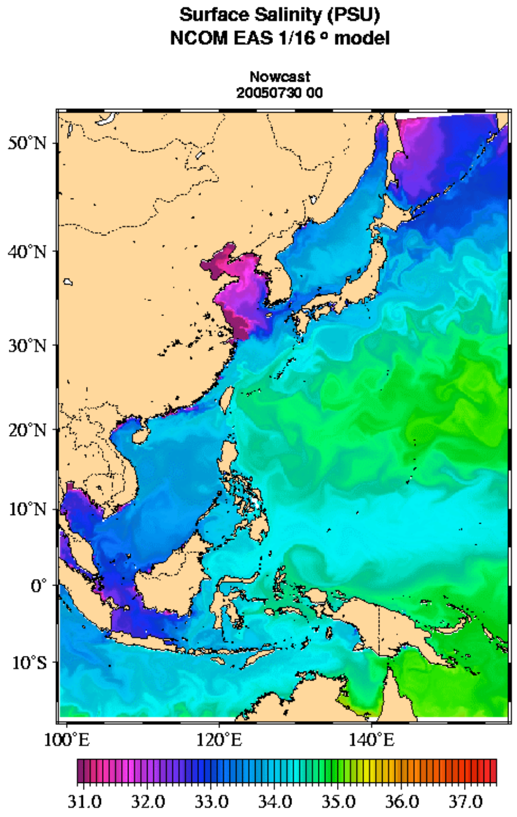

Figure 8. The Sea Surface Salinity during the internal solitary event in the West Philippine Sea. (From Naval Research Laboratory-Stennis Space Center)

THIS PAGE INTENTIONALLY LEFT BLANK

III. INTERNAL SOLITONS OBSERVED FROM A DRIFTING COASTAL MONITORING BUOY WITH ATTACHED THERMISTORS

A. COASTAL MONITORING BUOY AND THERMISTOR CHAIN DATA

A coastal monitoring buoy (CMB) was deployed by the U.S. Naval Oceanographic Office in WPS (Figure 9) from July 28–August 7, 2005. The original design is to collect the data every 10 minutes near the air-ocean interface. Above the ocean surface, the surface winds, air temperature, and air pressure are measured. Below the ocean surface, the temperature is observed at 1, 3, 5, 10, 15, and 20 meters. Fifteen thermistors (Figure 10) are attached to a wire rope extending from the code of CMB (20 m deep) to 140 m with a high frequency sampling rate (every 15 seconds). The purpose is to observe details of the upper layer structure. Figure 11 shows a contour plot of temperature ranging from 21°C to 29°C with 1.0°C increments on a vertical cross-section along the track (Figure 12). The total length of the cross-section is 229.14 km. The CMB travels 3.82 m every 15 seconds.

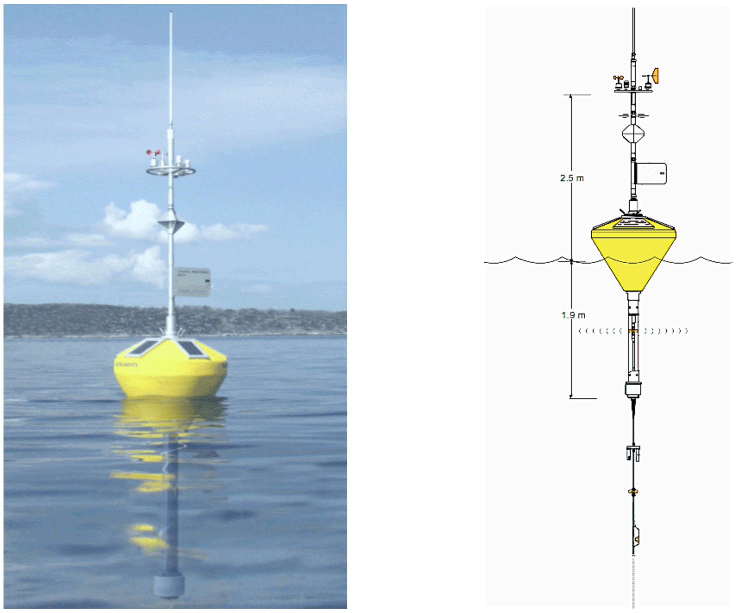

Figure 9. The Data Buoy DB 4280 was deployed from July 28 to August 7, 2005 to record the meteorological conditions and oceanographic measurements above a depth of 20 meters. (From www.aanderaa.no)

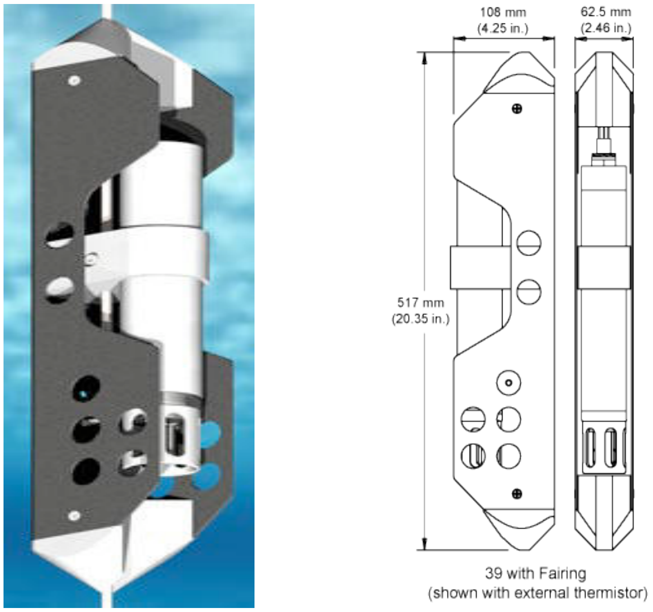

Figure 10. SBE39 Temperature and Pressure Recorder recorded the temperature and pressure every 15 seconds at 15 different depths. (From www.seabird.com)

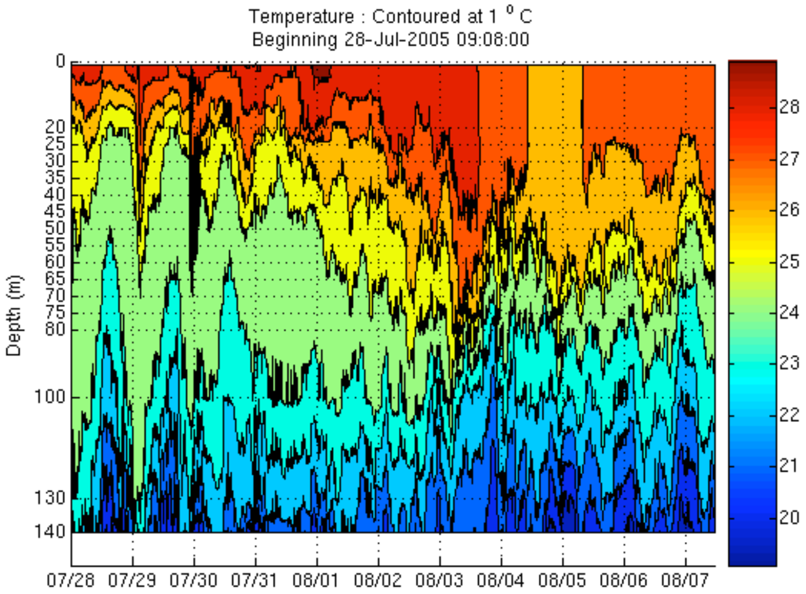

Figure 11. Time-depth plot of temperature. Note that the temperature ranging from 21°C to 29°C with 1.0°C increments on a vertical cross-section along the track during the recorded period.

The time-depth cross section of temperature along the CMB track shows a multi-scale variability with a highly irregular nature. The surface mixed layer is very thin (depth around 5 m) on July 28 with a temperature of about 28.5°C. Below the surface mixed layer, two thermoclines appear with the first thermocline at 50 m. The vertical gradient in the first thermocline is around 0.1°C/m. A relatively uniform sublayer (24°C) exists below the first thermocline from 50 to 130 m. Below the uniform sublayer, there is a second thermocline with a vertical temperature gradient around 0.04°C/m. As time approaches, the surface mixed layer deepens and the first thermocline descends. These processes contain small scale fluctuations. The surface mixed layer reached 70 m on August 5, when an evident cooling occurred with the mixed layer temperature reducing to 25.5°C. At the same time, the two thermoclines merged into a single thermocline with a vertical gradient of 0.06°C/m.

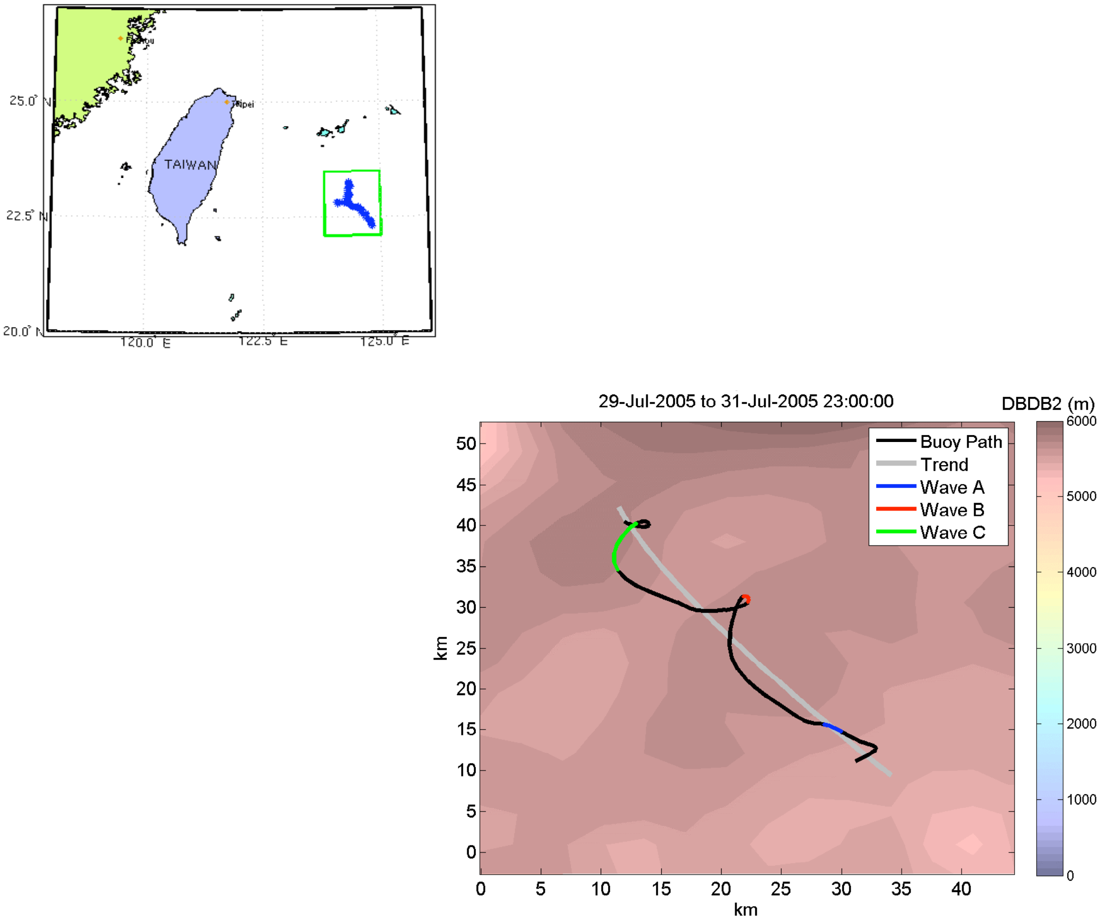

Figure 12. Track of CMB (from July 28 to August 7, 2005) deployed by the Naval Oceanography Office.

The buoyancy frequency (N) is computed by

$$N^2 = -\frac{g}{\rho(z)}\frac{\partial \rho(z)}{\partial z} \simeq -\alpha_T g \frac{\partial \overline{T}(z)}{\partial z} + \alpha_S g \frac{\partial \overline{S}(z)}{\partial z} . \qquad (1)$$

Here, α_T and α_S are the thermal expansion and saline contraction coefficients, respectively, with $\alpha_T = 2.41 \times 10^{-4}$ $(^{\circ}\mathrm{C})^{-1}$ and $\alpha_S = 7.45 \times 10^{-4}$ $(\mathrm{psu})^{-1}$ under the condition that $T = 20^{\circ}$C and $S = 35$ psu. Based on the Navy's climatological (T, S) data [i.e., Generalized Digital Environmental Model (GDEM)] for July and August data for the region identified as the box in Figure 12, we found that the $-\alpha_T \partial \overline{T}(z) / \partial z$ term is about an order of magnitude larger (averaged over the water column) than the $\alpha_S \partial \overline{S}(z) / \partial z$ term in (1). Thus, we can reasonably disregard the salinity, incurring at worst a 10% error. Since we have observational data from CMB on July 28–August 7, 2005, the mean temperature profile $\overline{T}(z)$ is calculated at each CMB sensor and thermistor over the whole path. The buoyancy frequency (Figure 13) calculated from the temperature only (Fig.5) has values around 5–7 cycles per hour (CHP). Since in the upper 25 m layer, the temperature was observed by CMB sensors and in the layer below 25 m depth, the temperature was observed by thermistors, high values of the buoyancy frequency (near 8 CPH) at 25 m may be caused by the use of different instruments.

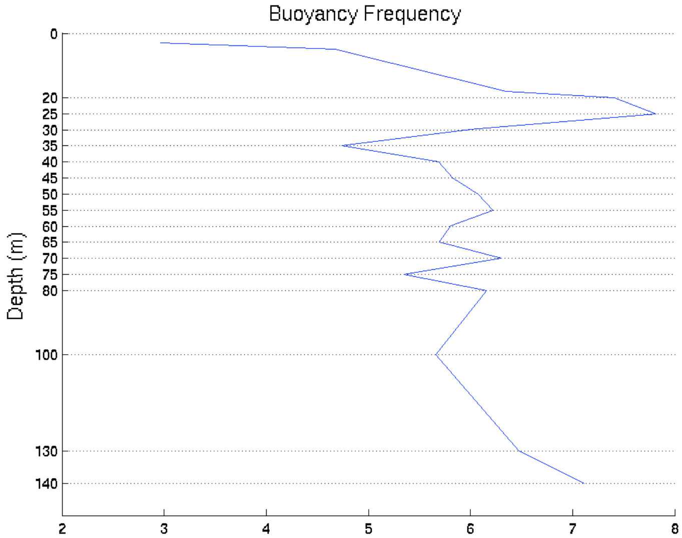

Figure 13. Buoyancy Frequency (N) calculated from CMB and attached thermistor temperature records during July 28–August 7, 2005.

Since we have observational data from CMB during July 28–August 7, 2005, the mean temperature profile $\overline{T}(z)$ is calculated at each CMB sensor and thermistor over the whole path. The buoyancy frequency calculated from the temperature only has values around 5 to 7 cycles per hour (CPH). Since in the upper 25 m layer, the temperature was observed by CMB sensors, and in the layer below 25 m depth, the temperature was observed by thermistors, high values of the buoyancy frequency may be caused by the use of different instruments.

B. TEMPERATURE ANOMALY

During the temperature sampling from CMB thermistors (Figure 14), thermal fluctuation in the upper layer can be divided into three types: internal-wave (IW) and turbulence, internal-soliton (IS) and turbulence, and dominant turbulence (no evident wave case). Here, we choose three 5-hr durations to represent the three types (a) The IW-turbulence, Wave-A (1000–1500 GMT July 29, Figure 15a), (b) IS-turbulence, Wave-B (0700-1200 GMT July 30, 2005, Figure 15b), (c) weak IW-turbulence, Wave-C (0200-0700 GMT July 31, Figure 15c), and turbulence-dominated, Wave-D (0000–0500 GMT August 1, Figure 15d) are selected for comparison.

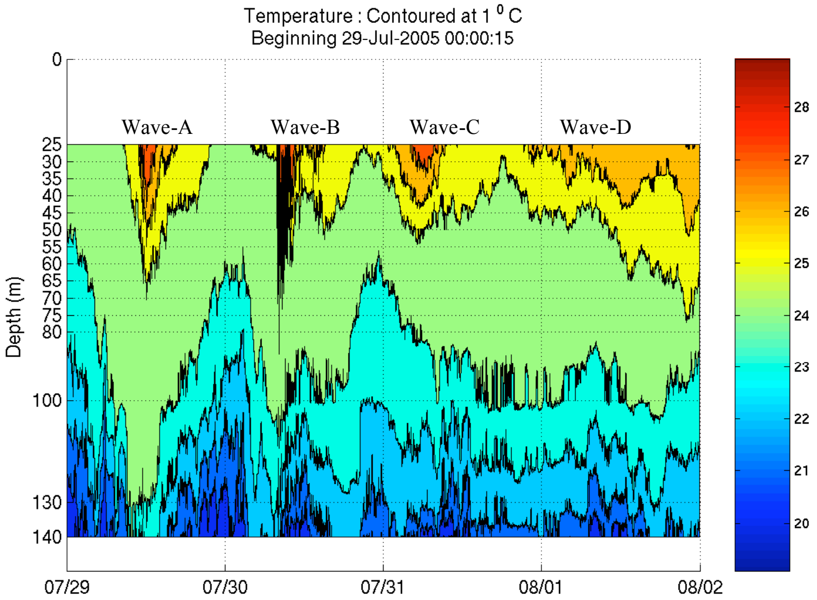

Figure 14. Time-depth cross section of temperature of Wave-A, B ,C and D.

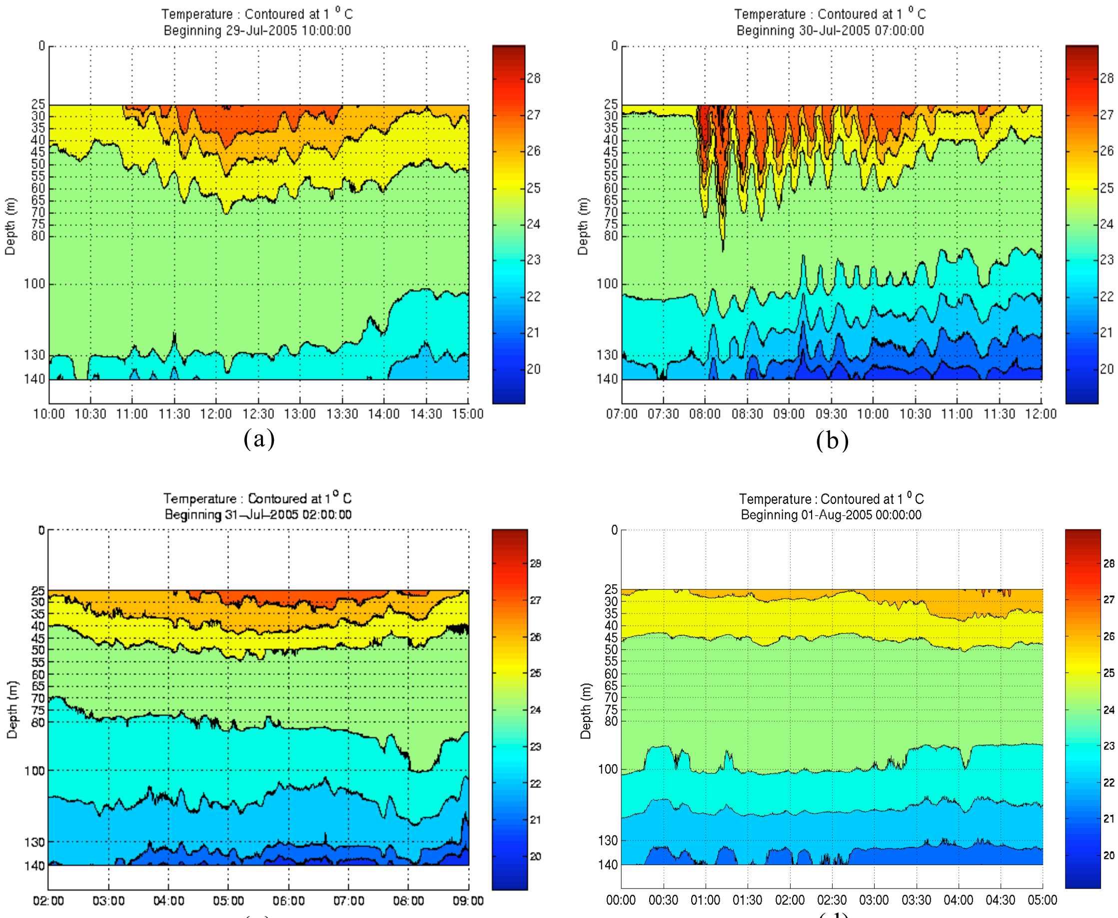

(a) (b)

(c) (d)

Figure 15. Temperature contour of the (a) IW-turbulence, Wave-A (1000–1500 July 29), (b) IS-turbulence,Wave-B (0700–1200 July 30), (c) Weak IW-turbulence, Wave-C (0200–0700 July 31), and (d) turbulence-dominated, Wave-D (0000–0500 August 1).

To identify these types, we calculate the temperature anomaly, which is the deviation of the observed temperature from the mean temperature,

$$T'(t,z) = T(t,z) - \overline{T}(z)\,, \tag{2}$$

For the IW-turbulence type, Wave-A (1000–1500 GMT July 29, Figure 16a), maximum temperature fluctuation decreases with depth from $\pm 1.6^{o}C$ at the surface to $\pm 0.4^{o}C$ at 100 m deep and then increases with depth to $\pm 1^{o}C$ at 140 m deep. The weak IS turbulence, Wave-C (0200–0700 July 31, Figure 16c), has the larger temperature fluctuation ($\pm 1.2^{o}\mathrm{C}$) at depth of 25–35m, decreases to the minimum ($\pm 0.3^{o}\mathrm{C}$) at 55–80 m depth, and then increases with depth to the maximum value ($\pm 1.6^{o}\mathrm{C}$) at depth 140 m.

For the IS-turbulence type, Wave-B (0700–1200 GMT July 30, Figure 16b), the maximum temperature fluctuation increases with depth from $\pm 1.8^{o}C$ at the surface to $\pm 2.9^{o}C$ at 60 m deep, then decreases with depth to $\pm 0.8^{o}C$ at 100 m deep, and finally increases with depth to $\pm 2.1^{o}C$ at 140 m deep.

For the dominant-turbulence type, Wave-D (0000–0500 GMT August 1, Figure 16d), the maximum temperature fluctuation decreases with depth from $\pm 1.3^{o}C$ at the surface to $\pm 0^{o}C$ at 60-65 m deep, and then increases with depth to $\pm 0.9^{o}C$ at 140 m deep.

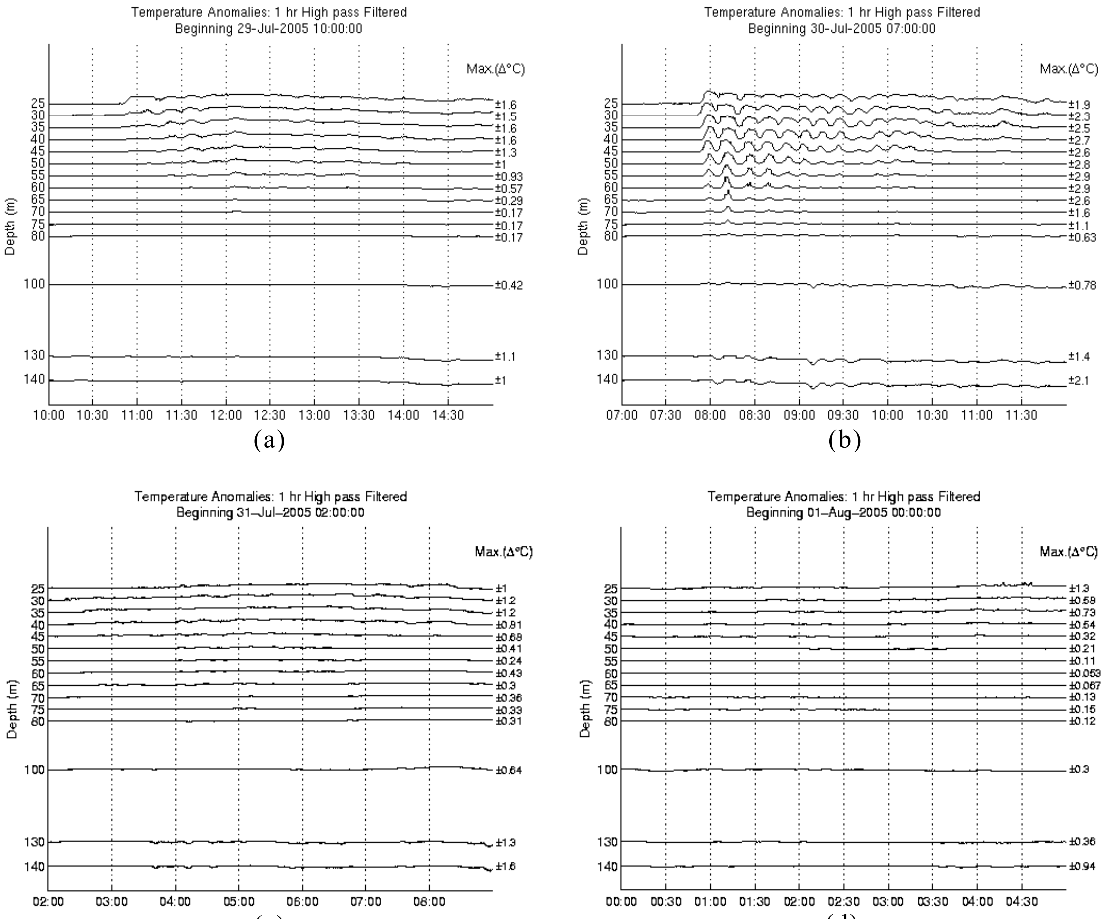

(a) (b)

(c) (d)

Figure 16. Temperature anomaly of (a) Wave-A (IW-turbulence), (b) Wave-B (IS-turbulence), (c) Wave-C (weak IW-turbulence), and (d) Wave-D (turbulence-dominated).

The observed temperature profile oscillates during the IW-turbulence case, Wave-A (Figure 17a) and Wave-C (Figure 17c), and the IS-turbulence case, Wave-B (Figure 17b), but not in the turbulence-dominated case, Wave-A (Figure 17d). The oscillation is evident in the upper layer above 50 m in the IW-turbulence case and above 80 m in the IS-turbulence case. The amplitude of the oscillation is much larger in the IS-turbulence case (maximum amplitude around 4°C) than the IW-turbulence case (maximum amplitude around 2°C).

For the IS-turbulence case, Wave-B (Figure 17b) shows the time evolution of the temperature profiles from fifteen thermistors, seven minutes apart from 0752 to 0827 GMT July 30, 2005. Among them, the black curve is the mean temperature profile over the whole CMB track [i.e., $\bar{T}(z)$].

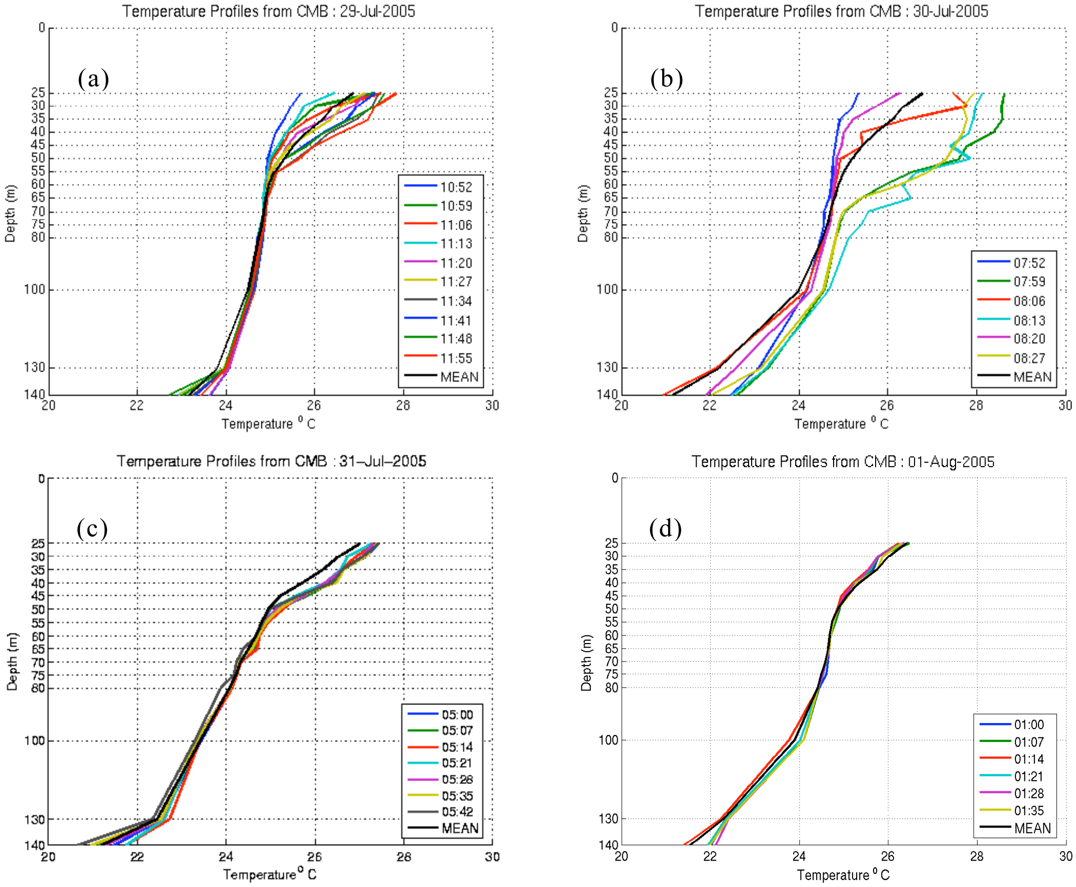

Figure 17. Temporally varying temperature profiles observed from CMB thermistors on (a) Wave-A (IW-turbulence), (b) Wave-B (IS-turbulence), (c) Wave-C (weak IW-turbulence), and (c) Wave-D (turbulence-dominated).

The temperature profile at 0752 GMT (blue curve) represents the cool upper layer with a temperature of 25.3°C at 25 m depth (the minimum among the five profiles). Seven minutes later (0757 GMT), the profile (green curve) represents a warm upper layer with a temperature of 28.7°C at 25 m depth (the maximum among the five profiles). Fourteen minutes later, the profile (red curve) shifts to the cool upper layer.

C. ISOPYCNAL DISPLACEMENT

With the temperature observation only, the isopycnal displacement is calculated by (Desaubles and Gregg, 1981)

$$\eta(t,z) = -\frac{T'(t,z)}{d\bar{T} / dz} \tag{3}$$

To better compare with the temperature anomaly, we plot the time variation of $\eta(t,z)$ at four different depths of 45, 50, 55, and 60 meters (25–40 and 65–80 m figures list in Appendix G). During the IW-turbulence case, Wave-A (Figure 18a), the isopycnal displacement oscillates with time and has maximum downwelling (20 m) at all four depths. During the IS-turbulence case, Wave-B period at 0800–0900 GMT (Figure 18b), the amplitude of isopycnal displacement $\eta(t,z)$ is around 50 meters at 45 m and 50 m depths and increases to nearly 100 meters at 60 m depth with a frequency of around 4 CPH. During the weak IW-turbulence case, Wave-C (Figure 18c), the isopycnal displacement is smaller than Wave-A period with maximum amplitude of around 6–8m. During the turbulence-dominated case, Wave-D (Figure 18d), the isopycnal displacement is very small with maximum amplitude around 4–6 m.

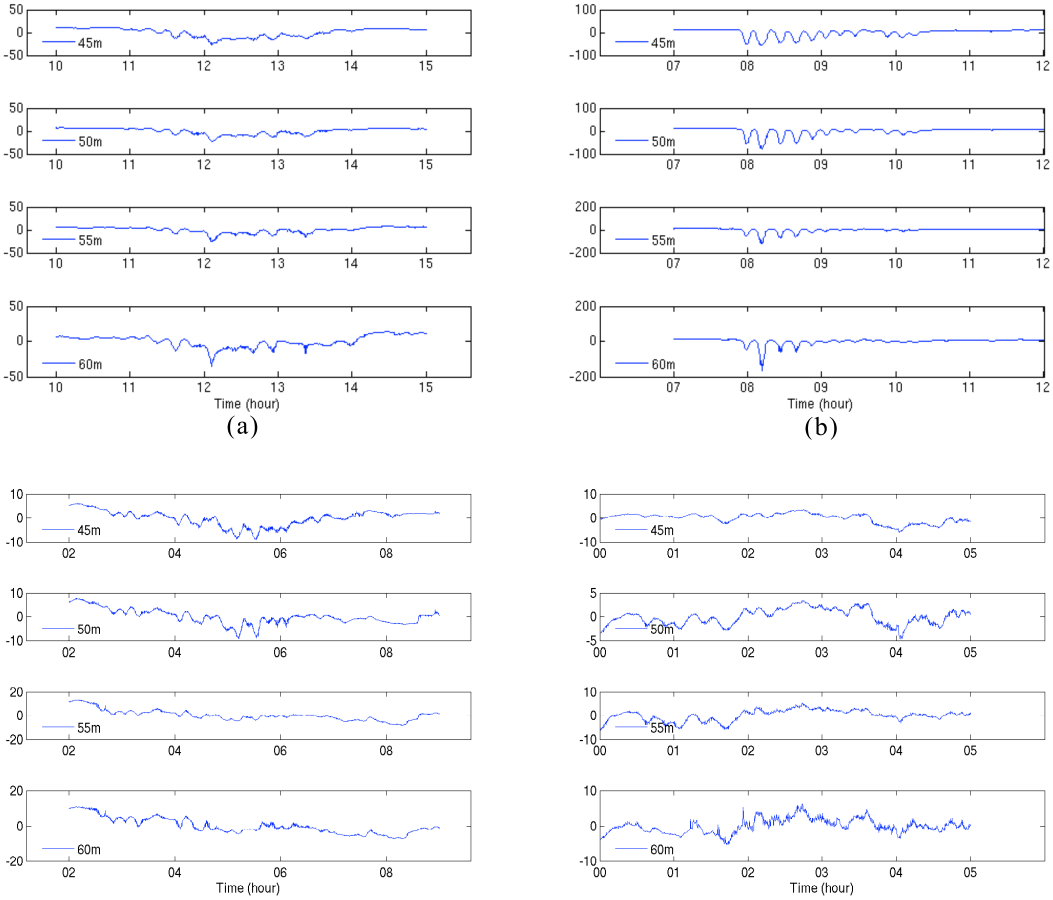

(a) (b)

(c) (d)

Figure 18. Isopycnal displacement measured by thermistors at depths of 45, 50, 55, and 60 meters on (a) Wave-A (IS-turbulence), (b) Wave-B (IS-turbulence), (c) Wave-C (weak IW-turbulence), and (d) Wave-D (turbulence-dominated).

Similar to the temperature profile, the isopycnal displacement profile oscillates during the IW-turbulence case, Wave-A (1000–1500 GMT July 29, Figure 19a) and IS-turbulence case (0700–1200 GMT July 30, Figure 19b), but not in weak IS-turbulence, Wave-C (0200–0700 GMT July 31, Figure 19c) and the turbulence-dominated case (0000–0500 GMT, August 1, Fig. 10c). The oscillation is evident in the upper layer above 50 m in the IW-turbulence case and above 80 m in the IS-turbulence case. The amplitude of the oscillation is much larger in the IS-turbulence case (maximum amplitude around 100 m) than the IW-turbulence case (maximum amplitude around 20 m).

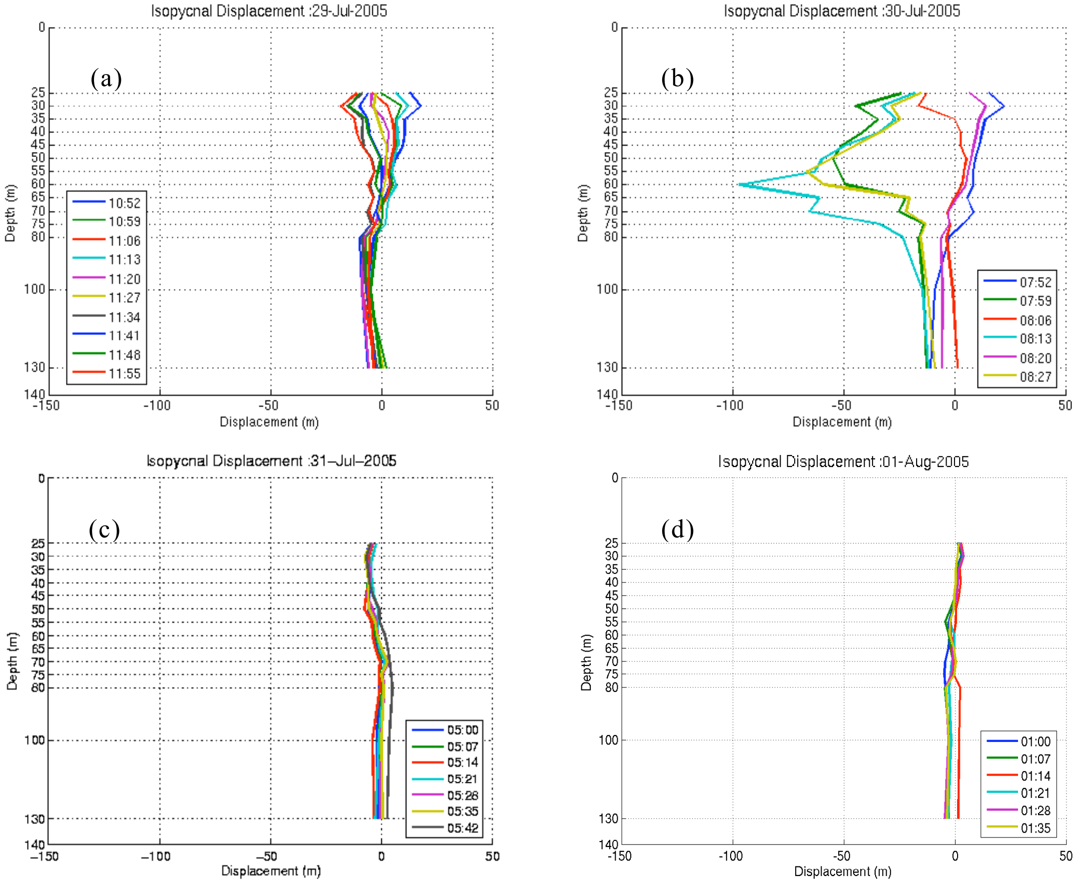

Figure 19. Isopycnal displacement with seven-minute intervals of (a) Wave-A (IW-turbulence), (b) Wave-B (IS-turbulence), (c) Wave-C (weak IW-turbulence), and (d) Wave-D (turbulence-dominated).

D. EMPIRICAL ORTHOGONAL FUNCTION ANALYSIS ON ISOPYCNAL DISPLACEMENT

The empirical orthogonal function (EOF) method is used to investigate first-order different features in the IW-turbulence and IS-turbulence cases using the data $\eta(t,z)$ at all time instances (one per every 15 s) and depths. The first EOF is able to account for 86.0% of the variance for the IW-turbulence case (Figure 20) and for 74.7% of the variance for the IS-turbulence case (Figure 21). The higher EOF modes (mode-2 to mode-4) contain nearly 20% variance of the isopycnal displacement and are not responsible for the IW and IS with a frequency of around 4 CPH, but are important for stirring and mixing scalar substances on the shelf [*Chu et al.*, 2003c].

The truncated isopycnal displacement is represented by

$$\tilde{\eta}(z,t)=\bar{\eta}(z)+A_1(t)\eta_1(z)\,. \tag{4}$$

Here, $\bar{\eta}(z)$ is the mean isopycnal displacement for the subset, $\eta_1(z)$ is EOF1 and $A_1(t)$ is the principal component of EOF1.

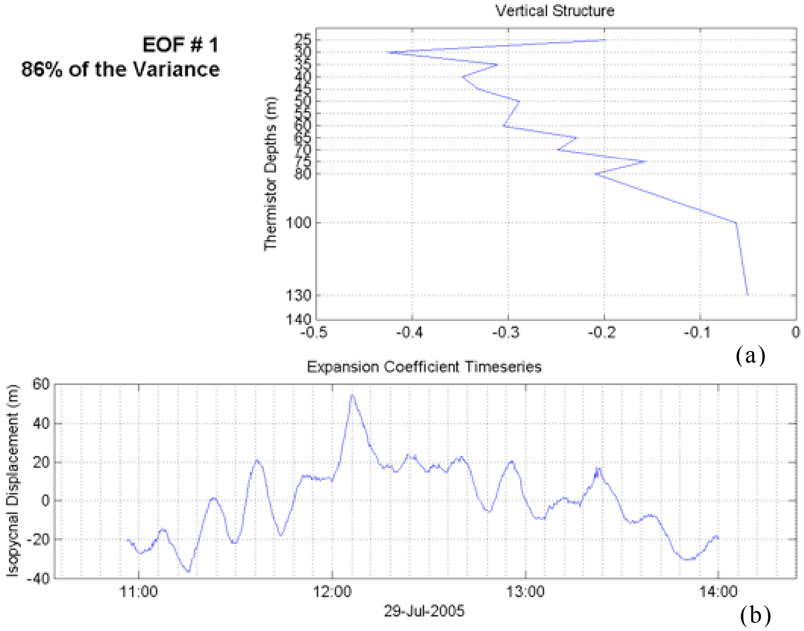

Figure 20. EOF (a) Mode-1 and (b) associated PC$_1$ of the isopycnal displacement on July 29, 2005, Wave-A (IW-turbulence).

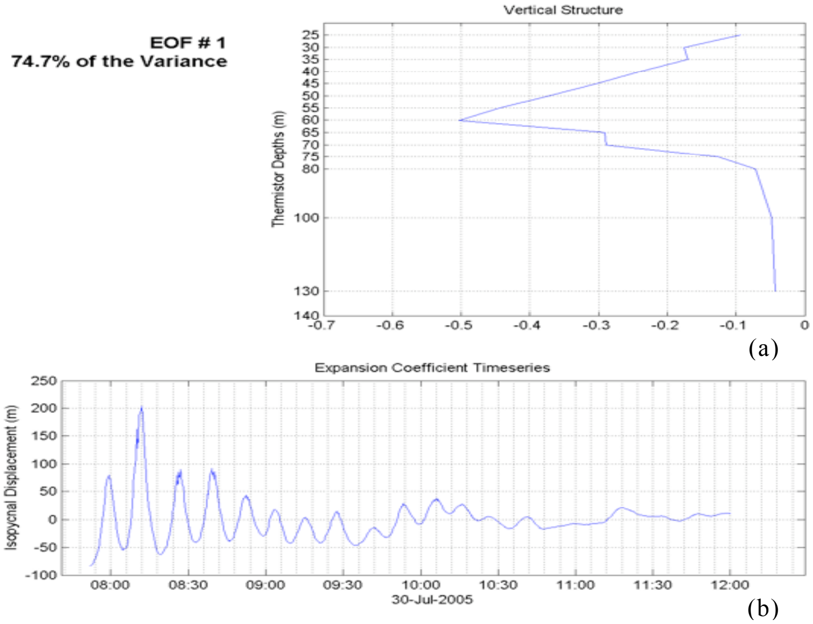

Figure 21. EOF (a) Mode-1 and (b) associated PC$_1$ of the isopycnal displacement on July 30, 2005, Wave-B (IS-turbulence).

Similarity and dissimilarity are found in EOF1 [$\eta_1(z)$] between the IW-turbulence and IS-turbulence cases. EOF1 in both cases shows the first baroclinic mode (similarity), but the maximum variability is located at different depths (dissimilarity) with 30 m for the IW-turbulence case and 60 m for the IS-turbulence case. However, dissimilarity is found in $A_1(t)$ between the IW-turbulence and IS-turbulence cases. For the IW-turbulence case, $A_1(t)$ fluctuates on two time scales with 4 CPH as a high frequency and around 5 CPH as a low frequency (Figure 20b). However, for the IS-turbulence case, $A_1(t)$ fluctuates on one time scale with a frequency of around 4 CPH (Figure 21b). The maximum amplitude of $A_1(t)$ is more than three times larger in the IS-turbulence case than in the IW-turbulence case.

THIS PAGE INTENTIONALLY LEFT BLANK

IV. STATISTICAL ANALYSIS UPPER OCEAN THERMAL STRUCTURE

A. POWER SPECTRA

The energy spectra of the isopycnal displacement (ϕ_η) is related to the temperature variance spectra (ϕ_T) by

$$\phi_\eta = \left\langle \frac{d\bar{T}}{dz} \right\rangle^{-2} \phi_T \, . \tag{5}$$

Since the statistical features of isopycnal displacement and temperature are related to each other, we only investigated the differences of the statistical structure of temperature fields among IW-turbulence, IS-turbulence, and turbulence-dominated cases.

Determination of the stationarity is the first step toward understanding the inherent thermal variability and statistical properties identified in this high-resolution temperature data with multi-layer structures. As mentioned in Chapter 3, the CMB collects the data every 15 seconds and travels with an average speed of 3.82 m per 15 seconds. For a given depth, the temperature data is a function of the horizontal coordinates, *x*,

$$T_i = T(x_i), \quad x_i = il, \quad i = 0,1,\ldots,\Lambda, \quad \Lambda = L/l, \tag{6}$$

where $l = 3.8$ m, is the horizontal resolution of the data, and L is the total horizontal scale of the data set. The data set has 60,300 temperature profiles (Λ = 60,300) and for each of the four cases (IW-turbulence, IS-turbulence, weak IW-turbulence, and turbulence-dominated), there are 1,200 temperature profiles (Λ = 1,200).

Spectral analyses of the temperature field,

$$E_j = E(k_j), \quad k_j = j/L, \quad j = 1,2,\ldots,\Lambda/2 \tag{7}$$

at all depths for each case were conducted, but for the sake of brevity, and to elucidate the important points, only spectra at six depths (25, 40, 60, 80, 100, and 140 meters) are shown in Figures 22, 23, 24, and 25. A Bartlett window was used to taper the ends of each series before calculating the power spectra to reduce the spectral leakage in the wavenumber domain.

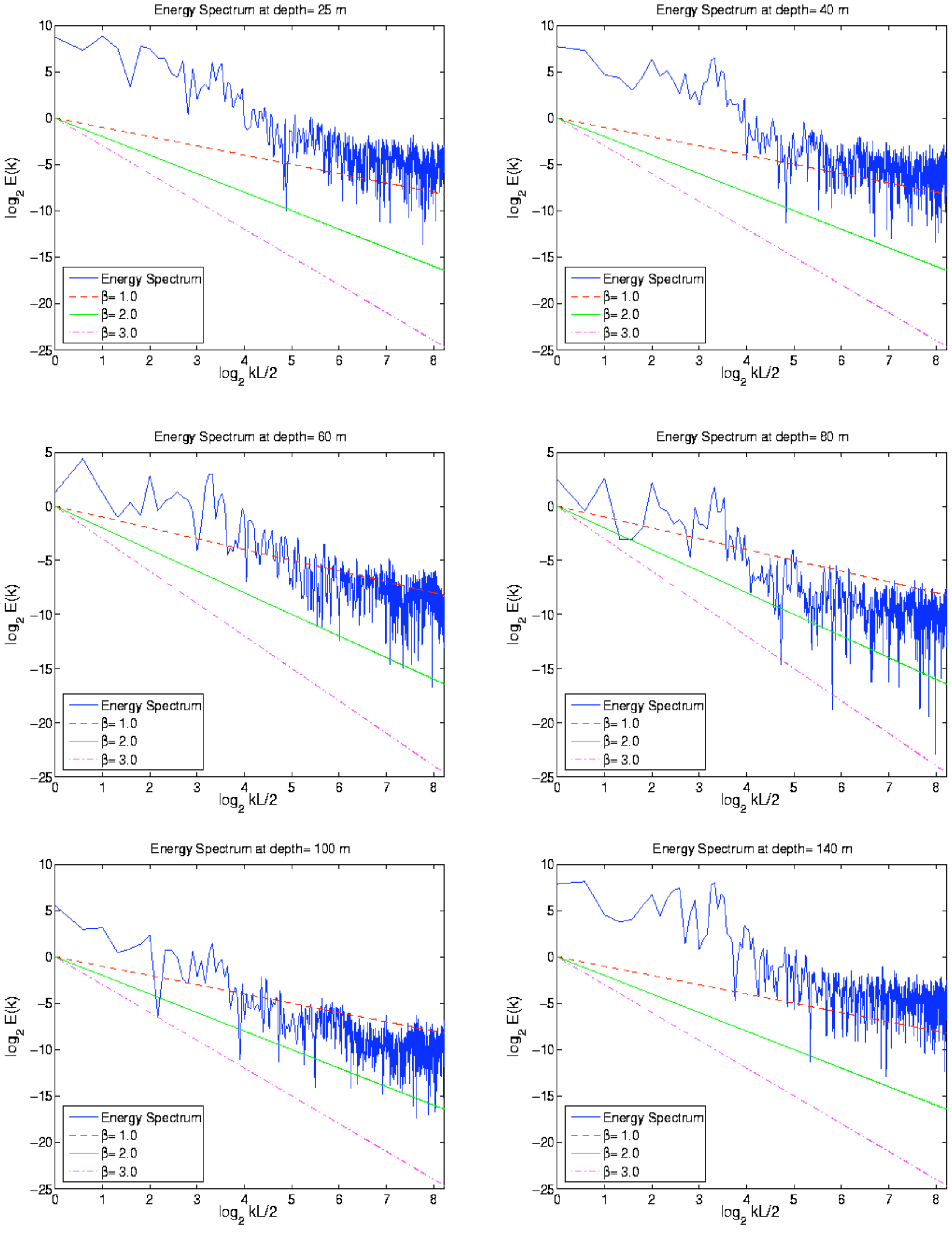

Figure 22. Power spectra of temperature filed at depths of 25, 40, 60, 80, 100, and 140 meters on Wave-A 1000–1500 GMT July 29 (IW-turbulence)

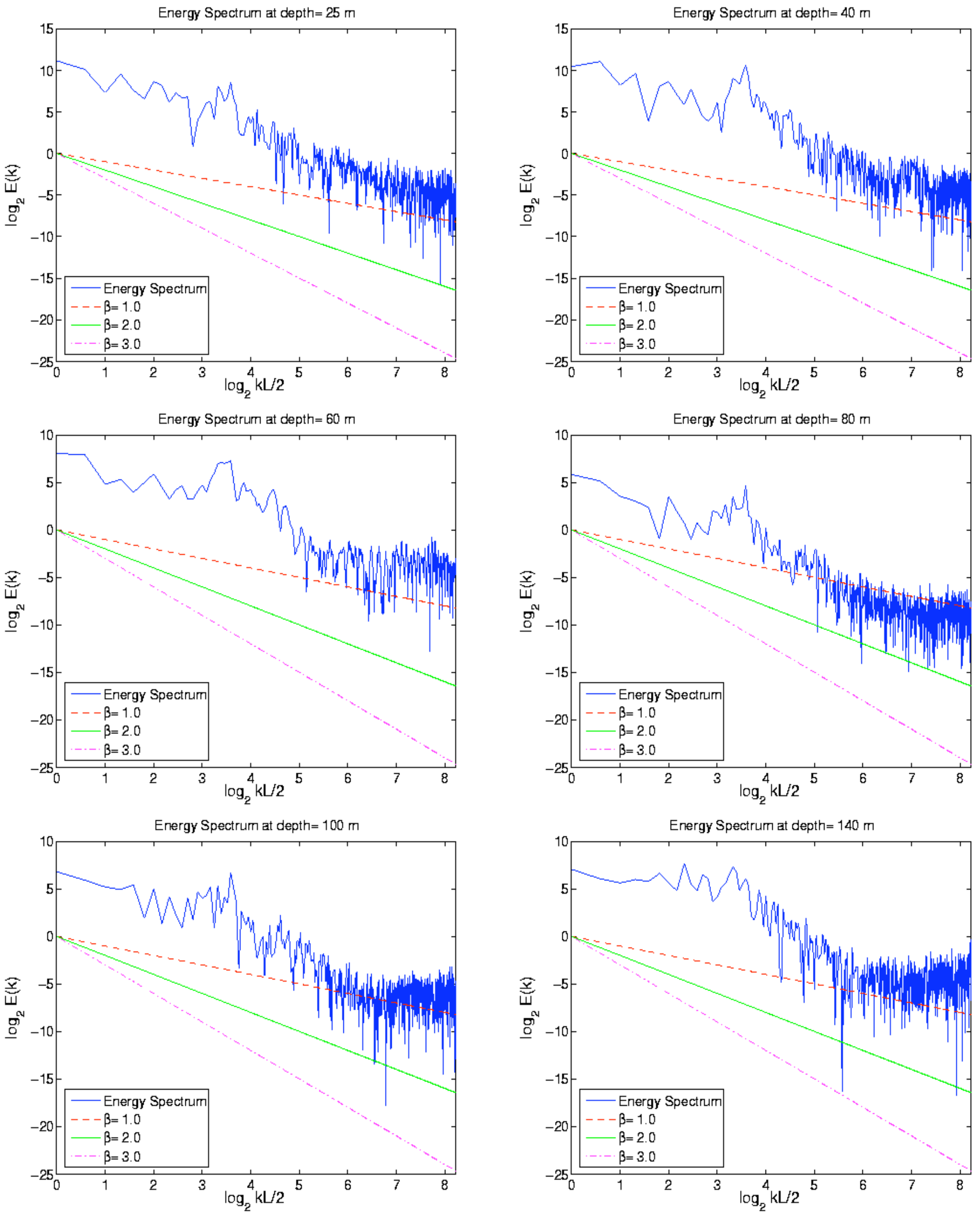

Figure 23. Power spectra of temperature filed at depths of 25, 40, 60, 80, 100, and 140 meters on Wave-B 0700–1200 GMT July 30 (IS-turbulence).

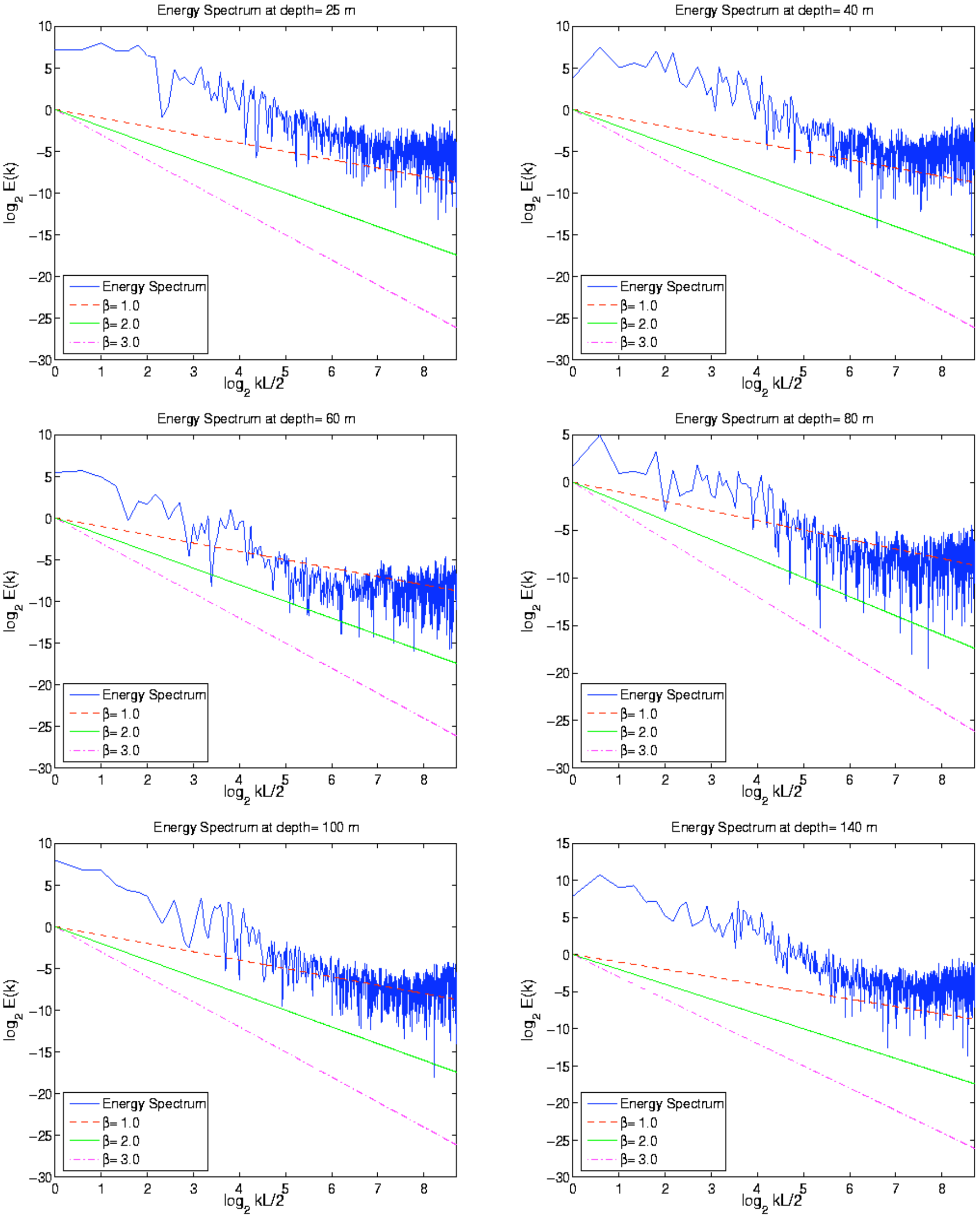

Figure 24. Power spectra of temperature filed at depths of 25, 40, 60, 80, 100, and 140 meters on Wave-C 0200–0700 GMT July 31 (weak IW-turbulence).

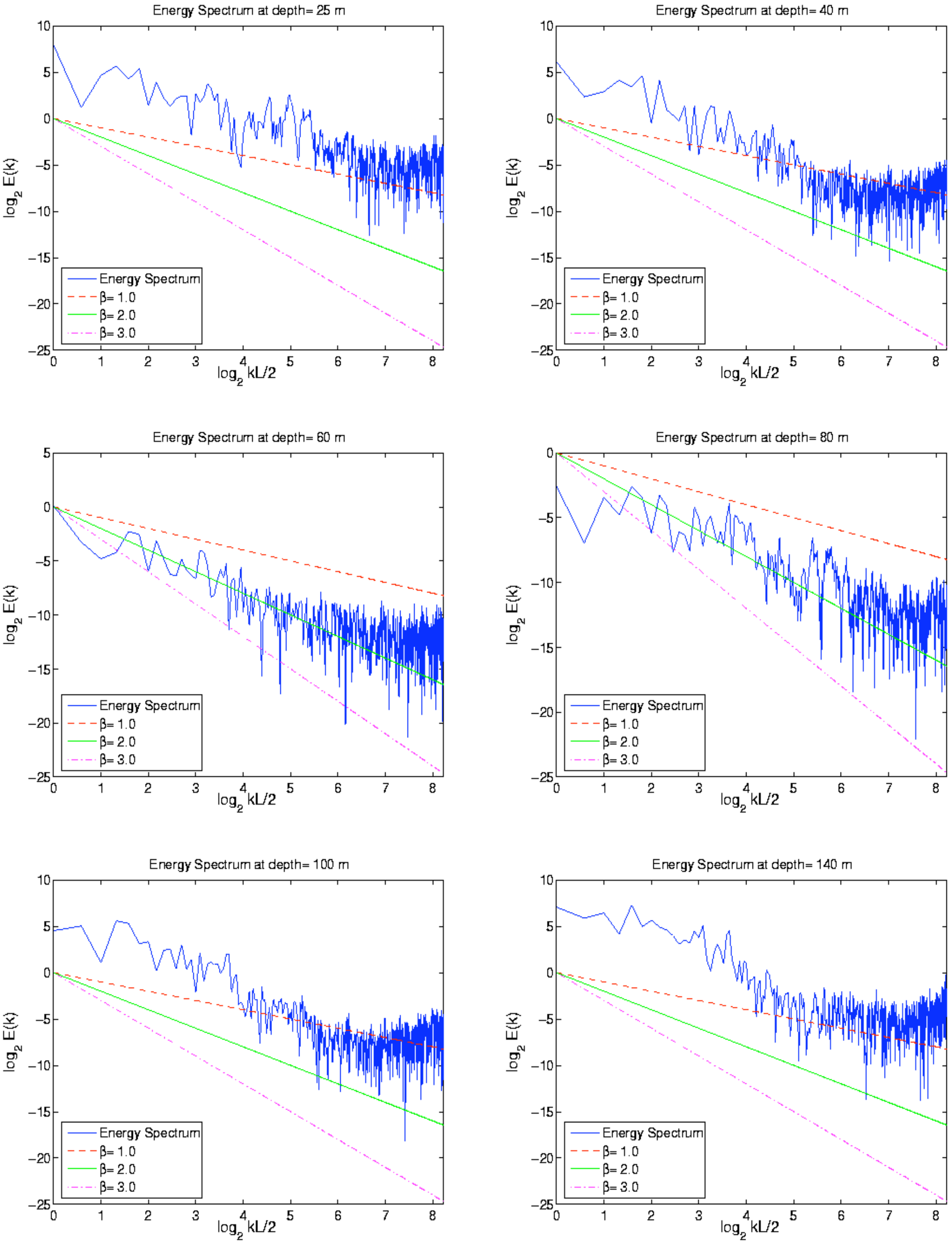

Figure 25. Power spectra of temperature filed at depths of 25, 40, 60, 80, 100, and 140 meters on Wave-D 0000–0500 GMT August 1 (turbulence-dominated).

For a scaling process, one expects power law behavior (Chu, 2004; Chu et al., 2002),

$$E(k) \propto k^{-\beta}, \tag{8}$$

over a large range of wavenumber *k*. The spectral exponent β contains information about the degree of stationarity of the data. If β < 1, the field is stationary; if 1 < β < 3, the field contains a nonstationary signal with stationary increments and in particular, the small-scale gradient field is stationary; if β > 3, the field is nonstationary with nonstationary increments.

The power spectra for the IW-turbulence (Figures 22, and 24) and turbulence-dominated case (Figures 25) have similar scaling characteristics with the spectral exponent β in the range of

$$1 < \beta < 2, \tag{9}$$

which means the temperature field is nonstationary with stationary increments. However, the power *E*(*k*) is much larger for the IW-turbulence case than the turbulence-dominated case. The spectrum for the IS-turbulence case (Figure 24) is quite different from the two other spectra, especially for the low wavenumber ($\log_2 kL/2 < 4$) domain where the spectral exponent β is less than 1.

B. STRUCTURE FUNCTIONS

Since the thermistor chain data set has stationary increments, we should study the statistical characteristics of the gradient field,

$$|\Delta T(r;x)| = |T(x_{i+r}) - T(x_i)|, \quad i = 0,1,\ldots,\Lambda - r, \tag{10}$$

where *r* denotes the lag between two data points. Obviously, *r* is inversely proportional to the wavenumber *k*,

$$r \propto \frac{1}{k}.$$

The structure functions (Eq. 11) are computed for the four cases: (a) IW-turbulence (1000–1500 GMT July 29), (b) IS-turbulence (0700–1200 GMT Jul 30), (c) weak IW-turbulence (0200–0700 GMT July 31), and (d) turbulence-dominated (0000–0500 GMT August 1), and used to depict thermal variability. The *q*th-order structure function is defined by the mean of the *q*-th power of the gradient field $|\Delta T(r;x)|$,

$$S(r,q) \equiv \left\langle \left|\Delta T(r;x)\right|^{q} \right\rangle = \frac{1}{\Lambda - r}\sum_{i=0}^{\Lambda - r}\left|\Delta T(r;x)\right|^{q}. \tag{11}$$

For example, $r = 1$, $q = 1$, the structure function represents the average magnitude of gradient.

$$S(1,1) = \frac{1}{\Lambda - 1}\sum_{i=0}^{\Lambda - 1}\left|T(x_{i+1}) - T(x_{i})\right| \tag{12}$$

Near-linear dependence of $\mathrm{Log}_2\,[S(r,\,q)]$ on $\mathrm{Log}_2(r)$ is found with different *q*-values from 1.0 to 6.0 for the IW-turbulence case (Figure 26), weak IW-turbulence case (Figure 28) and turbulent-dominant case (Figure 29). The straight lines with different slopes show that the structure functions for the upper ocean temperature in the WPS satisfies the power law

$$S(r,q) \propto r^{\zeta(q)}, \tag{13}$$

with the exponent $\zeta(q)$ depending on *q*. Since $S(r, 0) = 1$, the power $\zeta(q)$ should be 0 for $q = 0$. The power of $S(r, q)$ agrees quite well with earlier studies in the southwestern Greenland Sea, Iceland Sea, and Norwegian Sea (Chu, 2004): $\zeta(q)$ is monotonically and near-linearly increasing with *q*. Thus, it may be represented by

$$\zeta(q) = H(q)q, \tag{14}$$

where $H(q)$ is nearly a constant.

However, the structure function $S(r, q)$ for the IS-turbulence case does not satisfy Equation (13) (Figure 27). The power law seems broken at approximately $r = 8$ min, which is nearly the half-period of the IS (with frequency of 4 CPH). This phenomenon occurs at all depths.

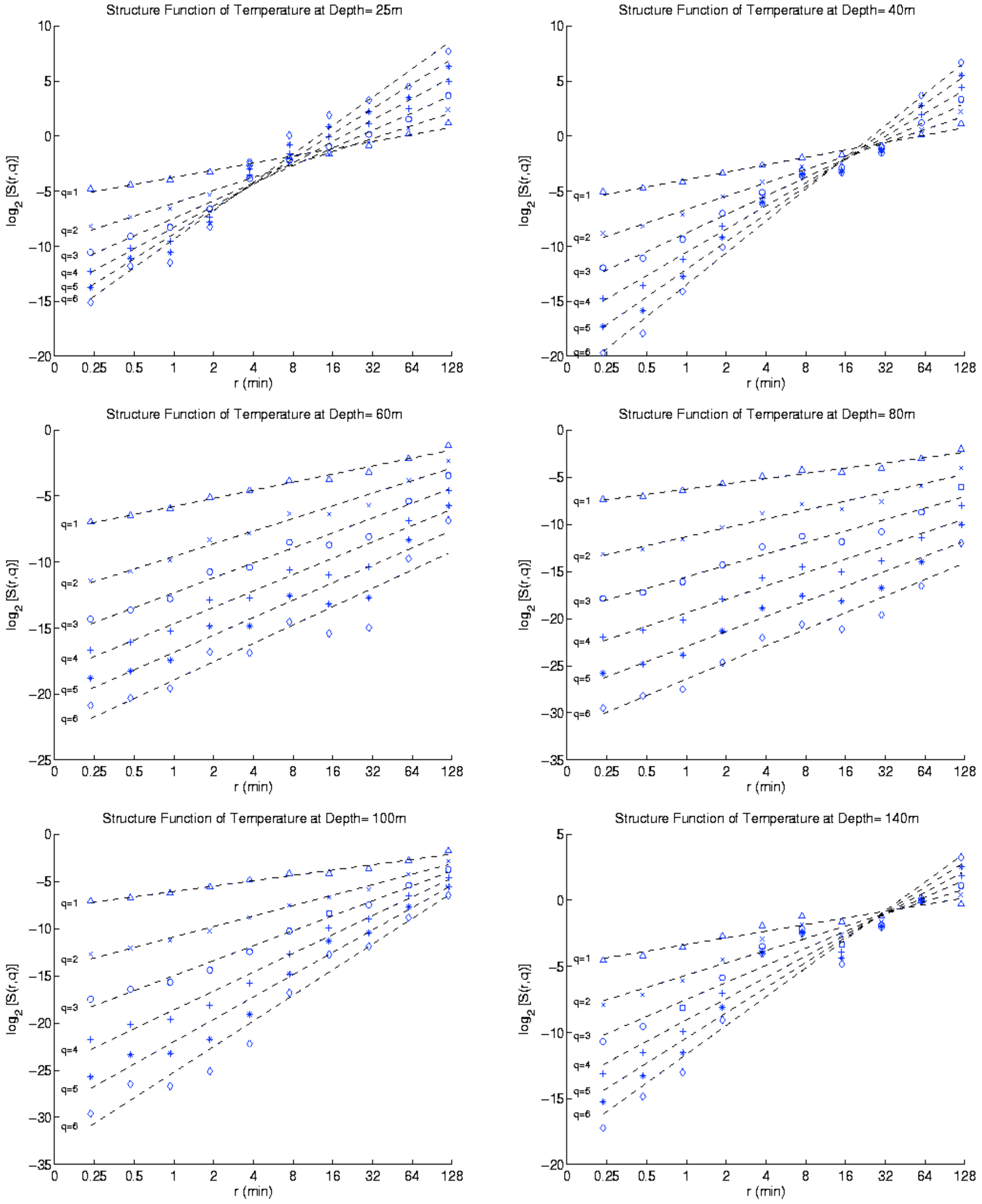

Figure 26. Structure functions for different *q*-values on Wave-A, 0000–0500 GMT July 29, 2005 (IW-turbulence) at depths of 25, 40, 60, 80, 100, and 140 m.

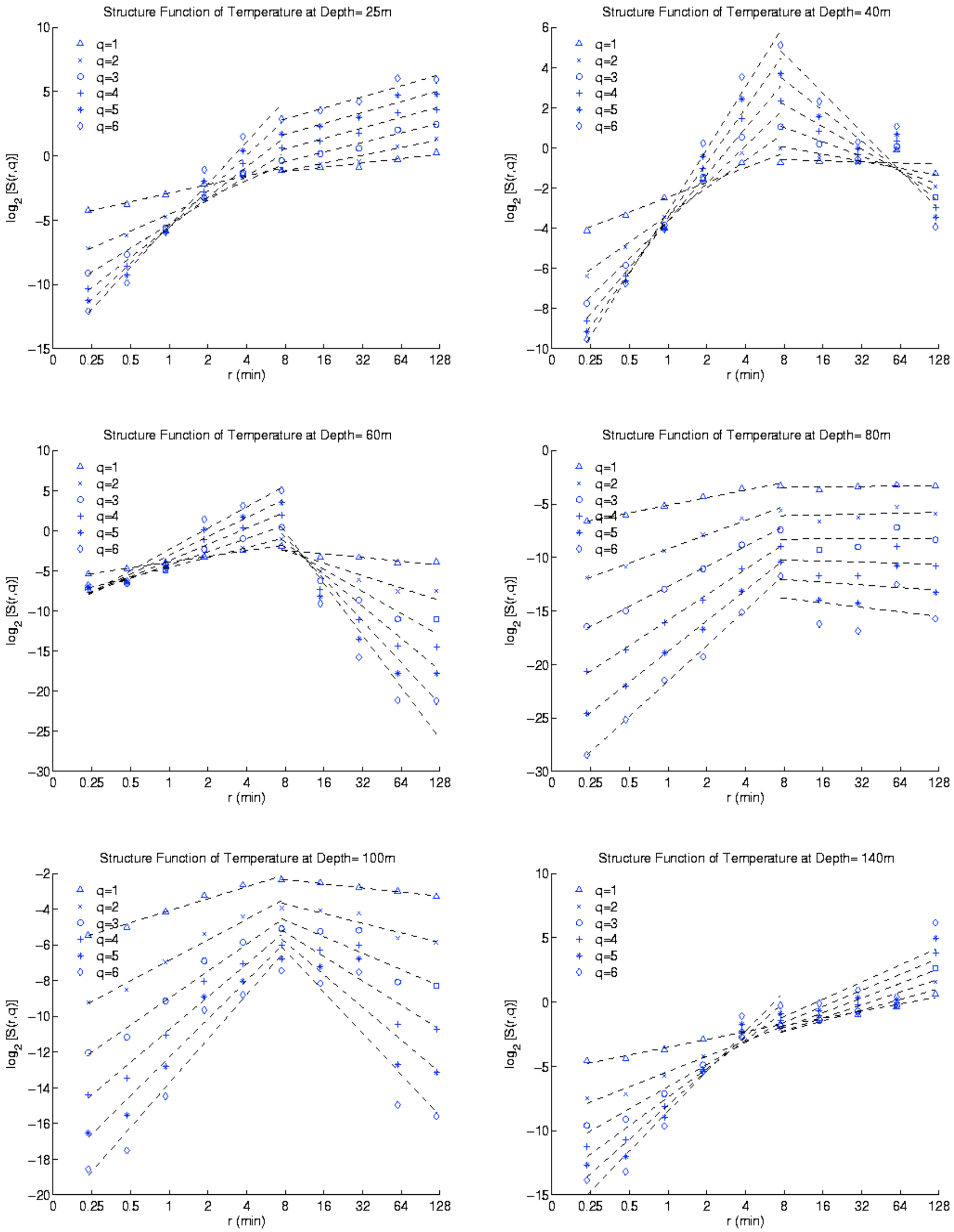

Figure 27. Structure functions for different *q*-values on Wave-B, 0700–1200 GMT July 30, 2005 (IS-turbulence) at depths of 25, 40, 60, 80, 100, and 140m.

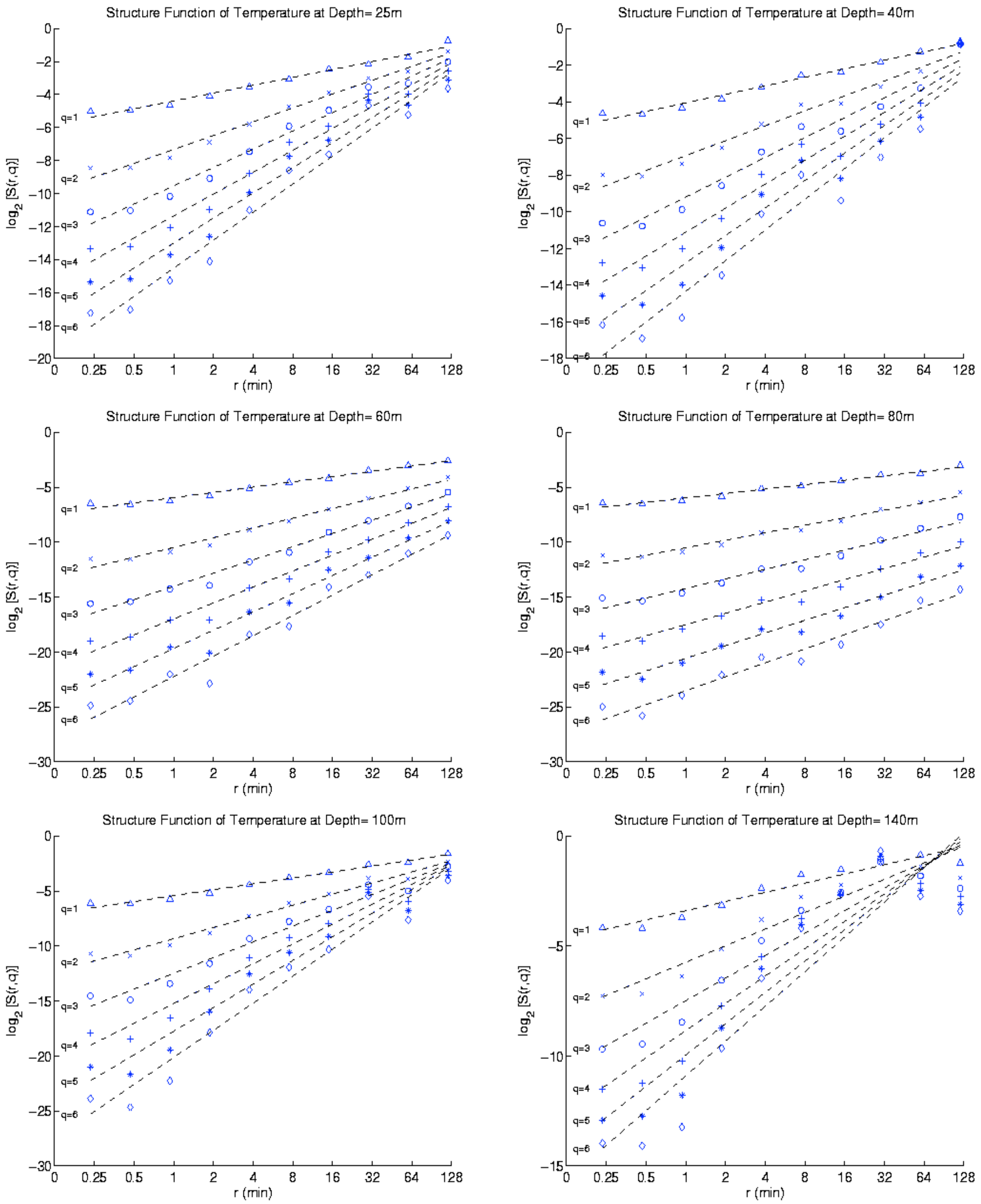

Figure 28. Structure functions for different *q*-values on Wave-C, 0200–0700 GMT July 31, 2005 (weak IW-turbulence) at depths of 25, 40, 60, 80, 100, and 140m.

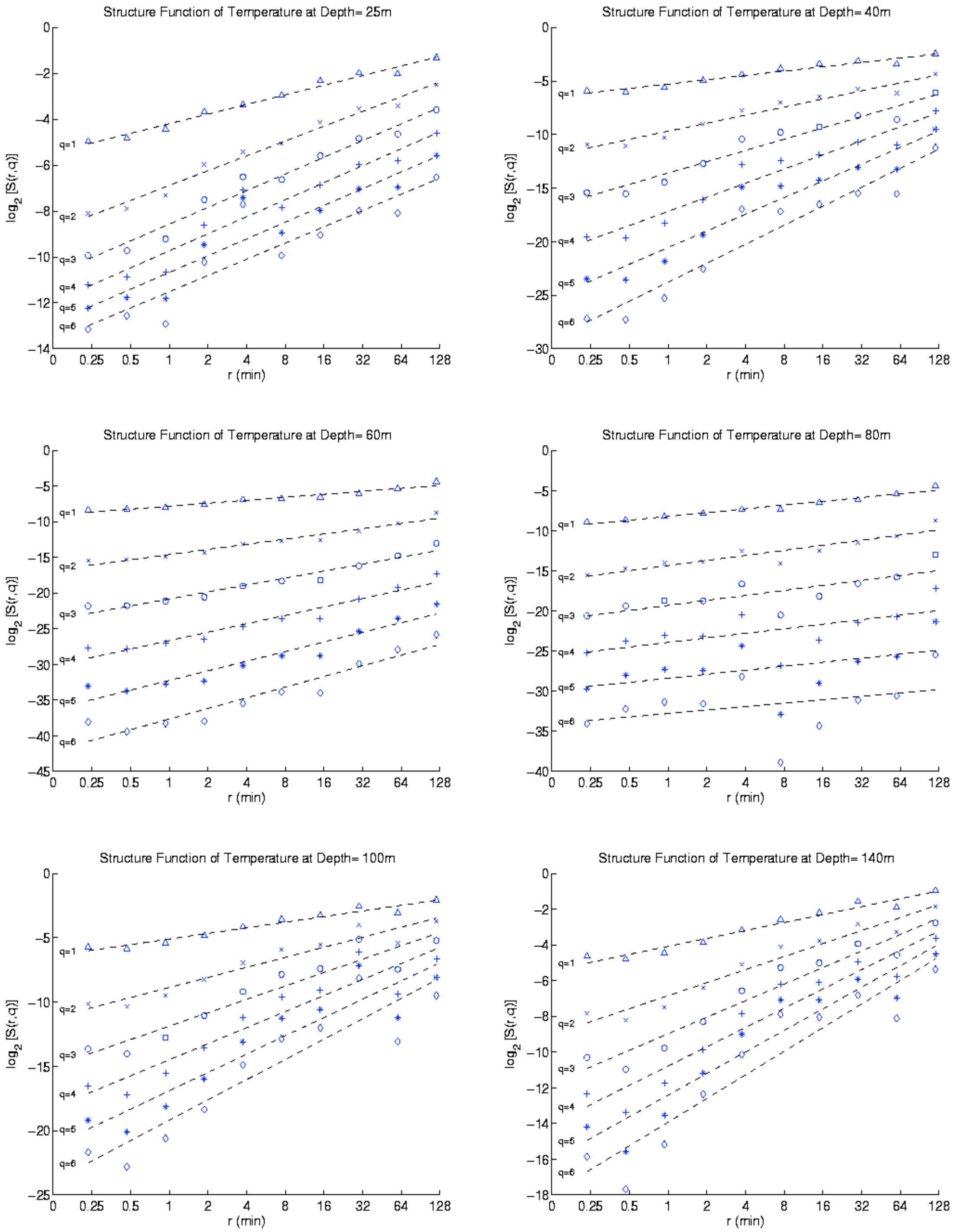

Figure 29. Structure functions for different *q*-values on Wave-D, 0000–0500 GMT August 1, 2005 (turbulence-dominated) at depths of 25, 40, 60, 80, 100, and 140m.

The power of the structure function, $\zeta(q)$, is computed for the whole dataset. Figure 30 shows the dependence of $\zeta(q)$ on q for selected levels. All the curves (near-linear) converge at $q = 0$ [$\zeta(0) = 0$], and show three different patterns: (a) slow increasing with q in the sub-layer (50–80 m), (b) intermediate-rate increasing with q in the upper thermocline (35–45 m) and lower thermocline (100–140 m), (c) fast increasing with q in the mixed layer (25–30 m). For $q \leq 1$, there is not much difference between the cases. The difference becomes evident as q increases. For $q = 6$, the power $\zeta(q)$ varies from 0.5 to 2.1 for the turbulence-dominated case, but from 1.2 to 3.0 for the IW-turbulence case. This indicates that the internal waves increase the power of the structure function especially for high moments.

The structure function for $q = 1$, $S(r, 1)$, is often used to determine the statistical characteristics of the data such as stochastical continuity and stationarity. When the structure function $S(r, 1)$ does not depend on r

$$S(r,1) = \text{const}, \tag{15}$$

which denotes exact stationarity. Eq.(14) is equivalent to

$$\zeta(1) = H(1) = 0 .$$

Thus, $H_1 \equiv H(1)$, represents the statistical characteristics of data. the Since the power $\zeta(1)$ [i.e., $H(1)$] varies with depth between 0.29 at 60 m depth (sub-layer) and 0.41 at 140 m depth (second thermocline), the thermal field in the WPS is nearly stationary.

If $g(T)$ is defined as the graph of $T(x)$, the dimension can be defined by (Mandelbrot, 1982)

$$D_{g(T)} = 2 - H_1 . \tag{16}$$

For a stochastically continuous ($H_1 = 1$) data $T(x)$, the graph is a smooth curve, whose dimension, $D_{g(T)} = 1$. If the graphs $g(T)$ fill the whole space (exactly stationary),

$$D_{g(T)} = 2, \tag{17}$$

which corresponds to $H_1 = 0$. The graph dimension of the WPS upper thermal field varies (multi-dimension structure) from higher values such as 1.71 (sublayer: 60 m), to lower values such as 1.59 (second thermocline: 120 m).

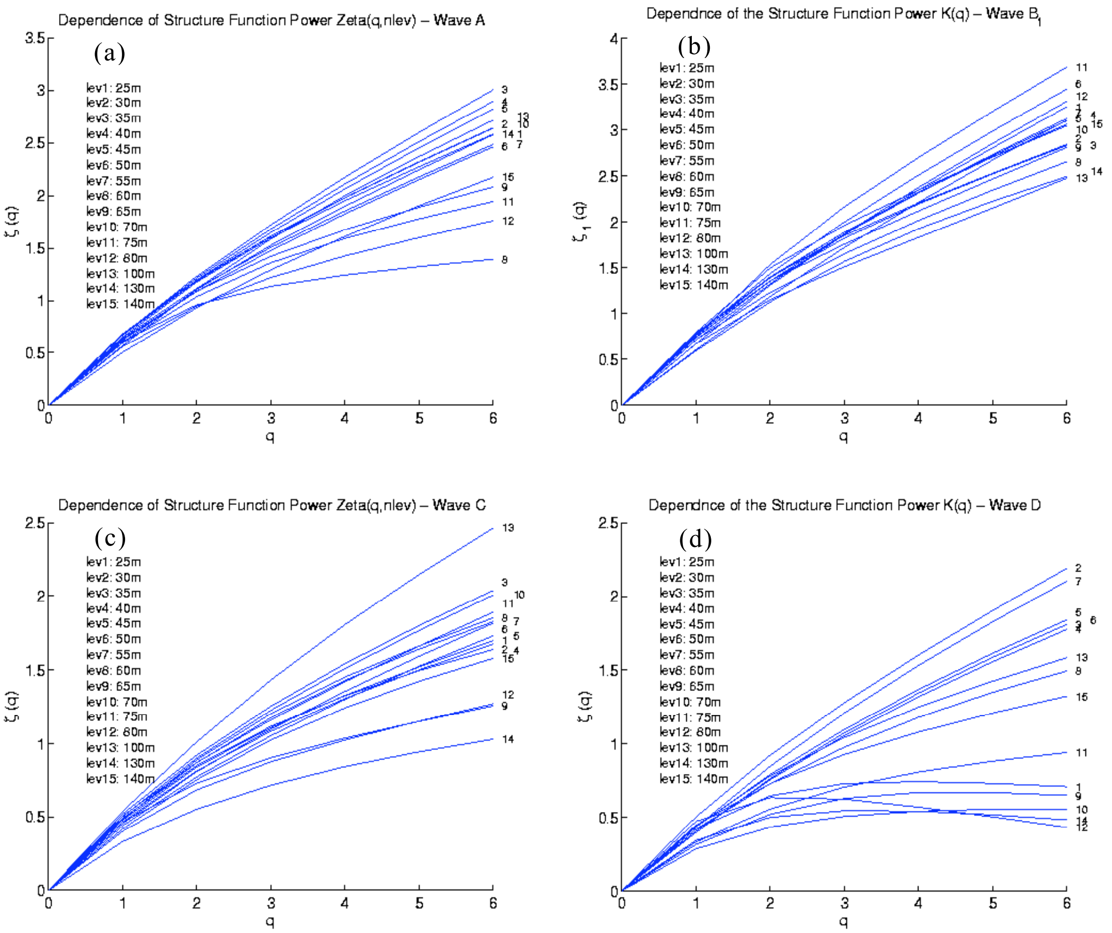

Figure 30. Dependence of $\zeta(q)$ on q=1.0 to 6.0 on the Structure Function of (a) Wave-A (IW-turbulence), (b) Wave-B (IS-turbulence), (c) Wave-C (weak IW-turbulence), and (d) Wave-D (turbulence-dominated).

C. SINGULAR MEASURES

Normalized small scale absolute gradient

$$\varepsilon(1;x_i) = \frac{|\Delta T(1;x_i)|}{\langle|\Delta T(1;x_i)|\rangle}, \qquad \langle|\Delta T(1;x_i)|\rangle = \frac{1}{\Lambda}\sum_{i=0}^{\Lambda-1}|\Delta T(1;x_i)|, \tag{18}$$

is used to identify the intermittency of the thermal field. The running average of r normalized values are computed by

$$\varepsilon(r;x_i) = \frac{1}{r}\sum_{j=i}^{i+r-1}\varepsilon(1;x_j), \qquad i = 0,1,...,\Lambda - r. \tag{19}$$

The mean of the qth power of $\varepsilon(r;x_i)$

$$M(r,q) \equiv \left\langle \varepsilon(r;x_i)^q \right\rangle = \frac{1}{\Lambda - r}\sum_{i=0}^{\Lambda - r}\left[\varepsilon(r;x_i)\right]^q, \tag{20}$$

is defined as the qth-order singular measure. Obviously, for $q = 0$,

$$M(r, 0) = 1. \tag{21}$$

For $q = 1$,

$$M(r,1) \equiv \left\langle \varepsilon(r;x_i) \right\rangle = \frac{1}{\Lambda - r}\sum_{i=0}^{\Lambda - r}\left[\varepsilon(r;x_i)\right]$$

$$= \frac{1}{\Lambda - r}\sum_{i=0}^{\Lambda - r}\left[\frac{1}{r}\sum_{j=i}^{i+r-1}\varepsilon(1;x_j)\right] = 1. \tag{22}$$

Singular measures are computed for all depths. For simplicity, $M(r, q)$ for six depths (25, 40, 50, 75, 100, 140 m) is given here (Figures 31, 32, 33, and 34). Near-linear dependence of $\mathrm{Log}_2\,[M(r, q)]$ on $\mathrm{Log}_2(r)$ is found for all cases with different q-values from 1.0 to 6.0. The straight lines with different slopes show that the singular measures with various q for the upper layer temperature in the WPS satisfies the power law

$$M(r,q) \propto r^{-K(q)}, \qquad q \geq 0, \tag{23}$$

with the power $K(q)$ varying with q. From Eq. (21) and (22), we have

$$K(0) = K(1) = 0. \tag{24}$$

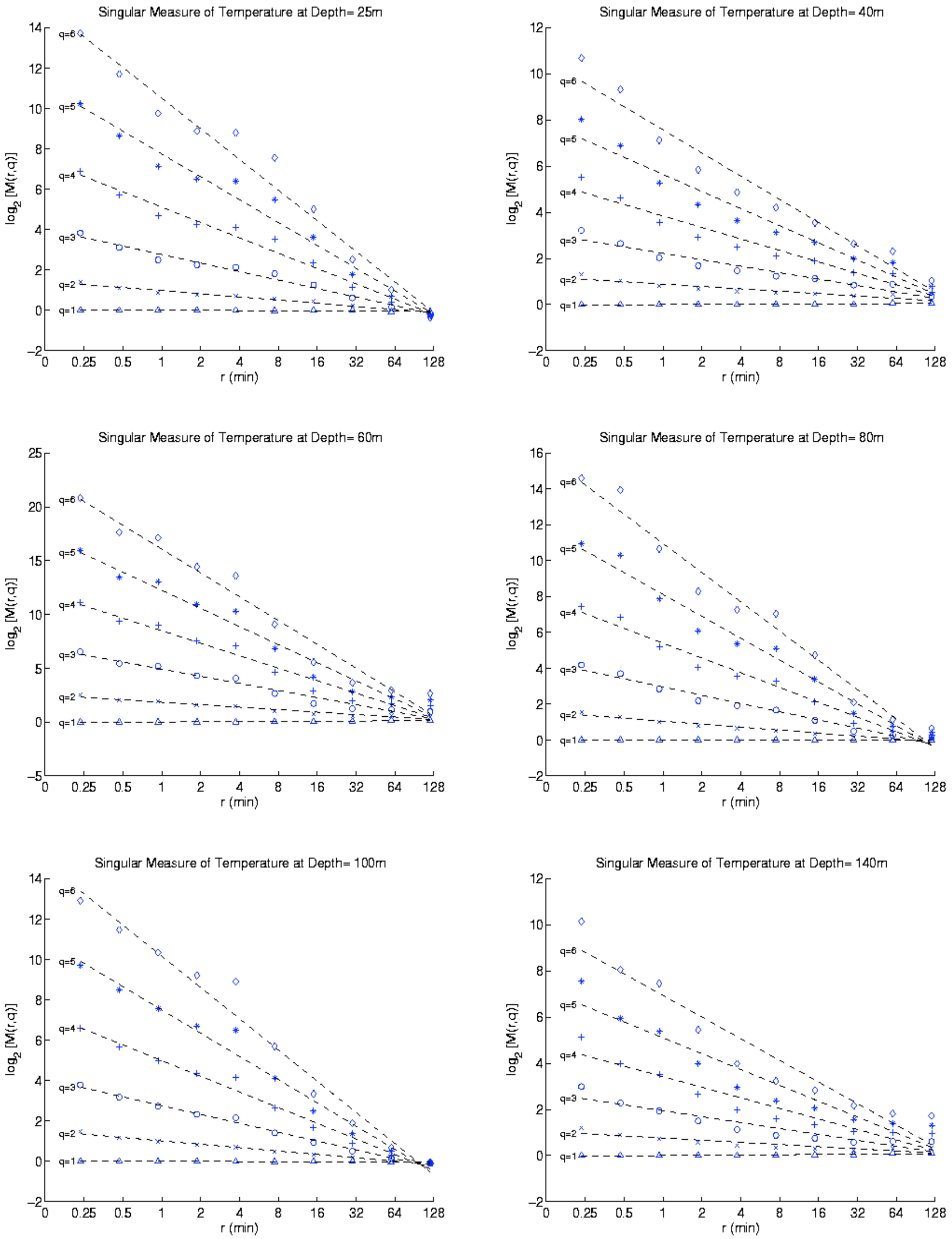

Singular Measure of Temperature at Depth= 25m

Singular Measure of Temperature at Depth= 40m

Singular Measure of Temperature at Depth= 60m

Singular Measure of Temperature at Depth= 80m

Singular Measure of Temperature at Depth= 100m

Singular Measure of Temperature at Depth= 140m

Figure 31. Singular Measures for different *q*-values on Wave-A (IW-turbulence) at depths of 25, 40, 60, 80, 100, and 140m.

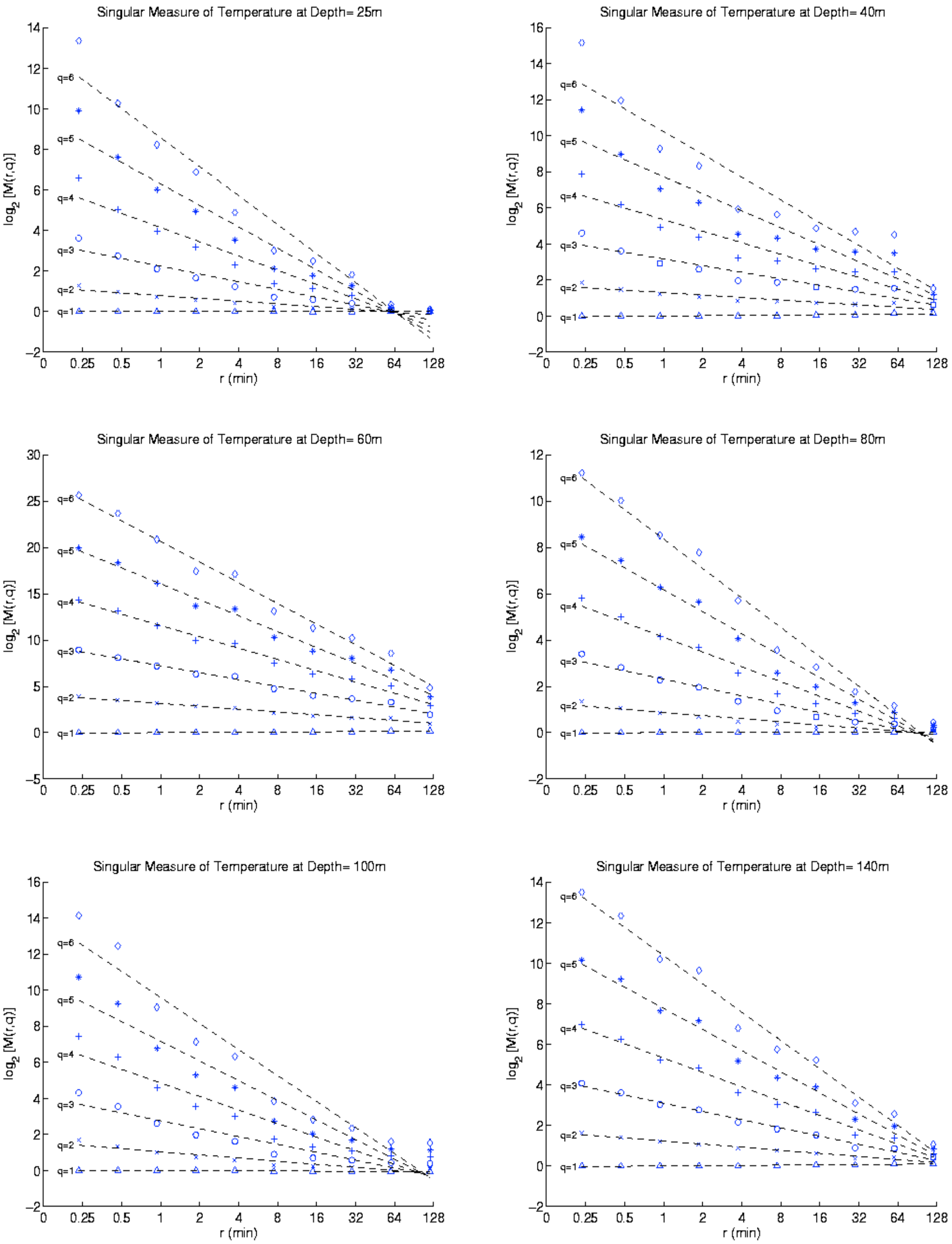

Figure 32. Singular Measures for different *q*-values on Wave-B (IS-turbulence) at depths of 25, 40, 60, 80, 100, and 140m.

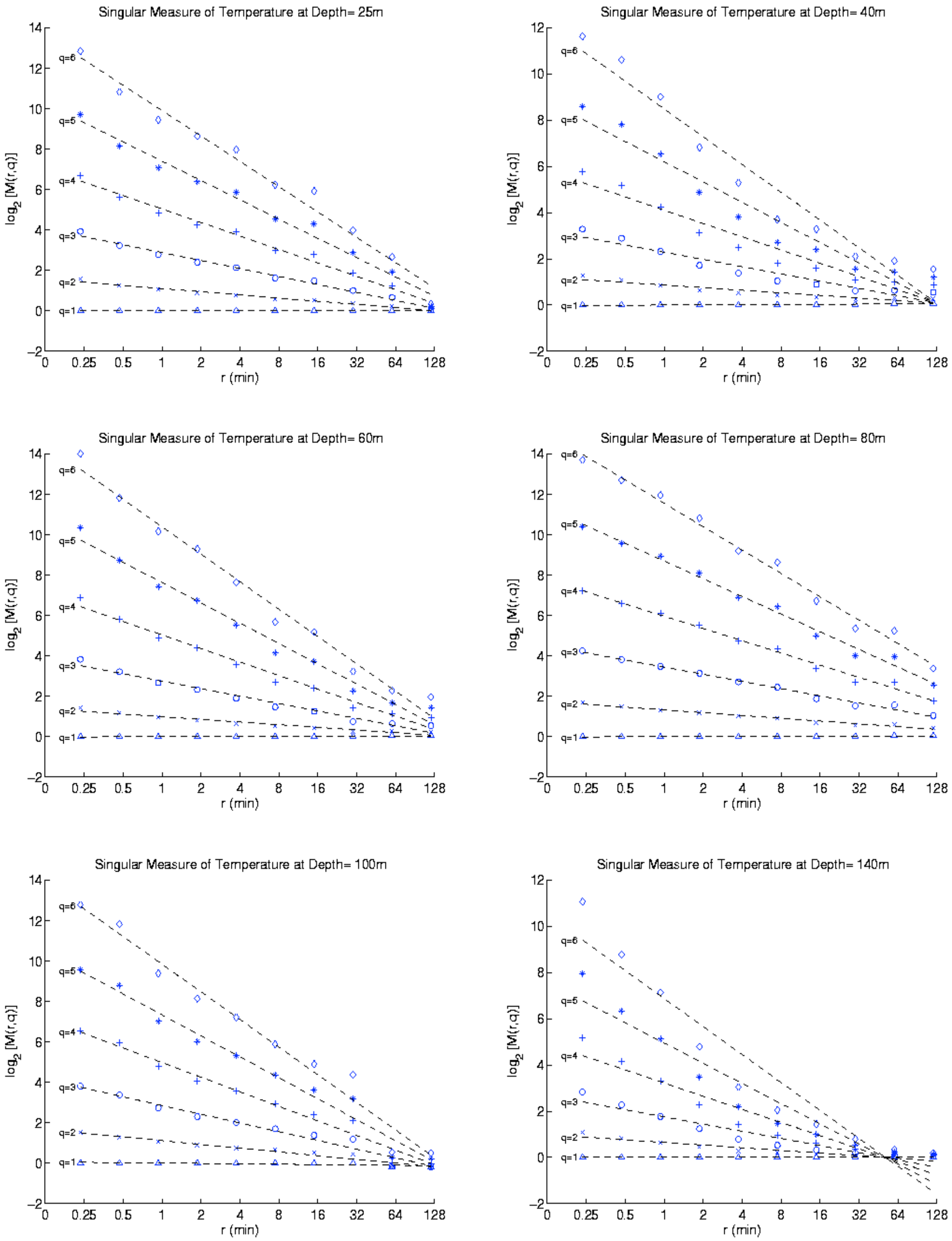

Figure 33. Singular Measures for different *q*-values on Wave-C (weak IW-dominated) at depths of 25, 40, 60, 80, 100, and140m.

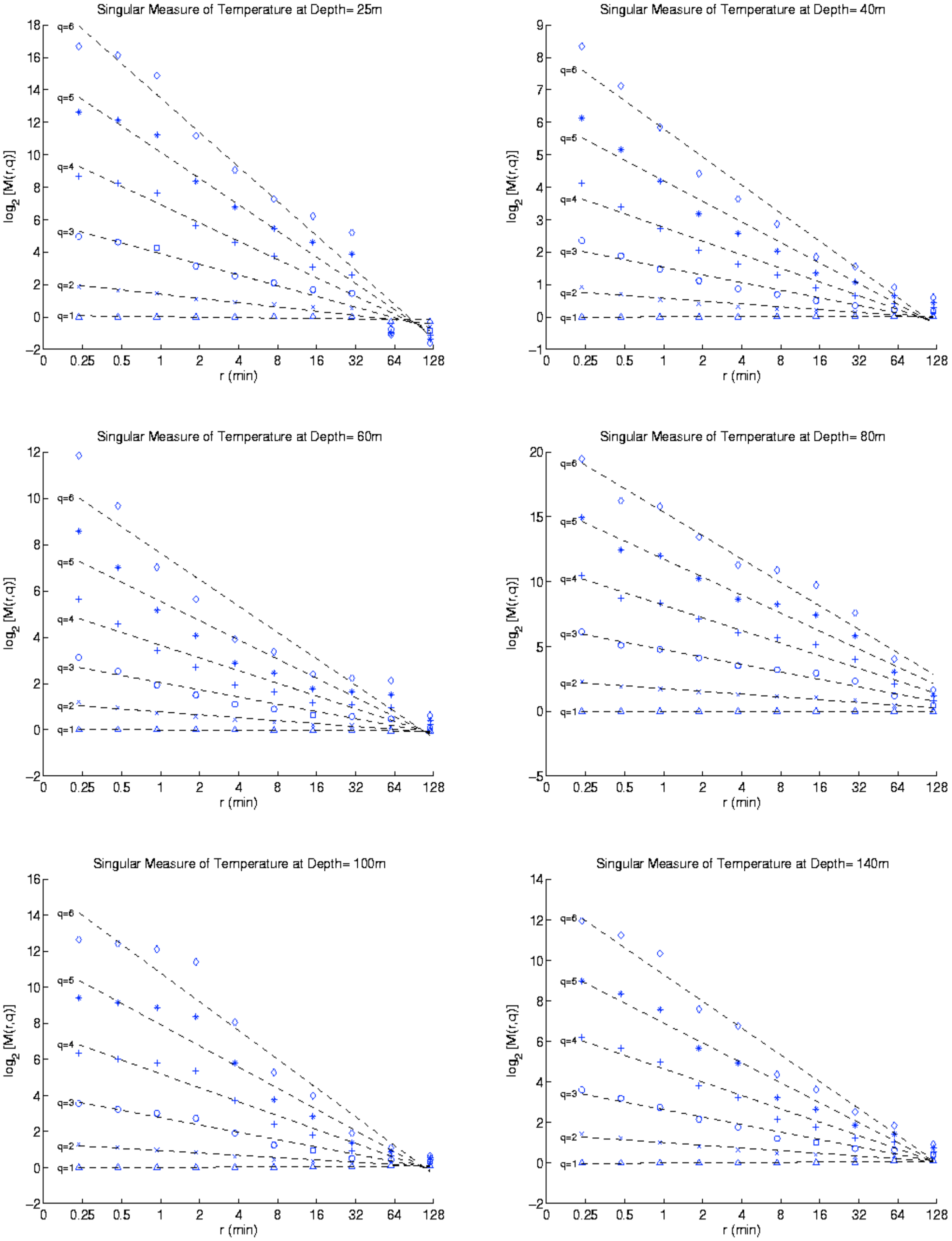

Figure 34. Singular Measures for different *q*-values on Wave-D (turbulence-dominated) at depths of 25, 40, 60, 80, 100, and 140m.

Several characteristics are found in Figures 31 to 34: The power $K(q)$ is a convex function

$$\frac{d^2K(q)}{dq^2} > 0, \tag{25}$$

for all q and

$$K(q) < 0 \qquad \text{only if} \qquad 0 < q < 1 \tag{26}$$

which reflects the fact that, in this range, taking a q^{th} power necessarily reduces the fluctuation of $\varepsilon\,(r;\, x_i)$; and otherwise

$$K(q) \geq 0, \qquad \text{if} \qquad q \geq 0. \tag{27}$$

Following Chu (2004), we may define a function

$$C(q) = \frac{K(q)}{q-1}. \tag{28}$$

For $q \to 1$, we use *l'Hosptal*'s rule to define a straightforward measure of inhomogeneity in the sense of singular measure

$$C_1 \equiv C(1) = K'(1) \geq 0, \tag{29}$$

which is called the intermittency parameter. The larger the value of C_1, the lager the intermittency and singularity the data set has. The C_1-value is computed at all depths for the three cases. The intermittency parameter C_1 varies from 0.25 to 0.6 for the turbulence-dominated case (Figure 35d), from 0.25 to 0.67 for the IW-turbulence case (Figure 35a), from 0.25 to 4.4 for the weak IW-turbulence, and 0.29 to 0.84 for the IS-turbulence case (Figure 35b). The highest intermittency (maximum value of C_1) occurs at the up-most part for the turbulence-dominated case, but at the mid-level for the IW-turbulence (60 m deep) and IS-turbulence (65 m deep) cases. High C_1 values (> 0.7) do not occur for the turbulence-dominated case and IW-turbulence case, but occur in the middle layer (58–73 m, where the thermocline is located, see Figure 15b) for the IS-turbulence case. This indicates that the internal solitons generate high intermittency around the thermocline.

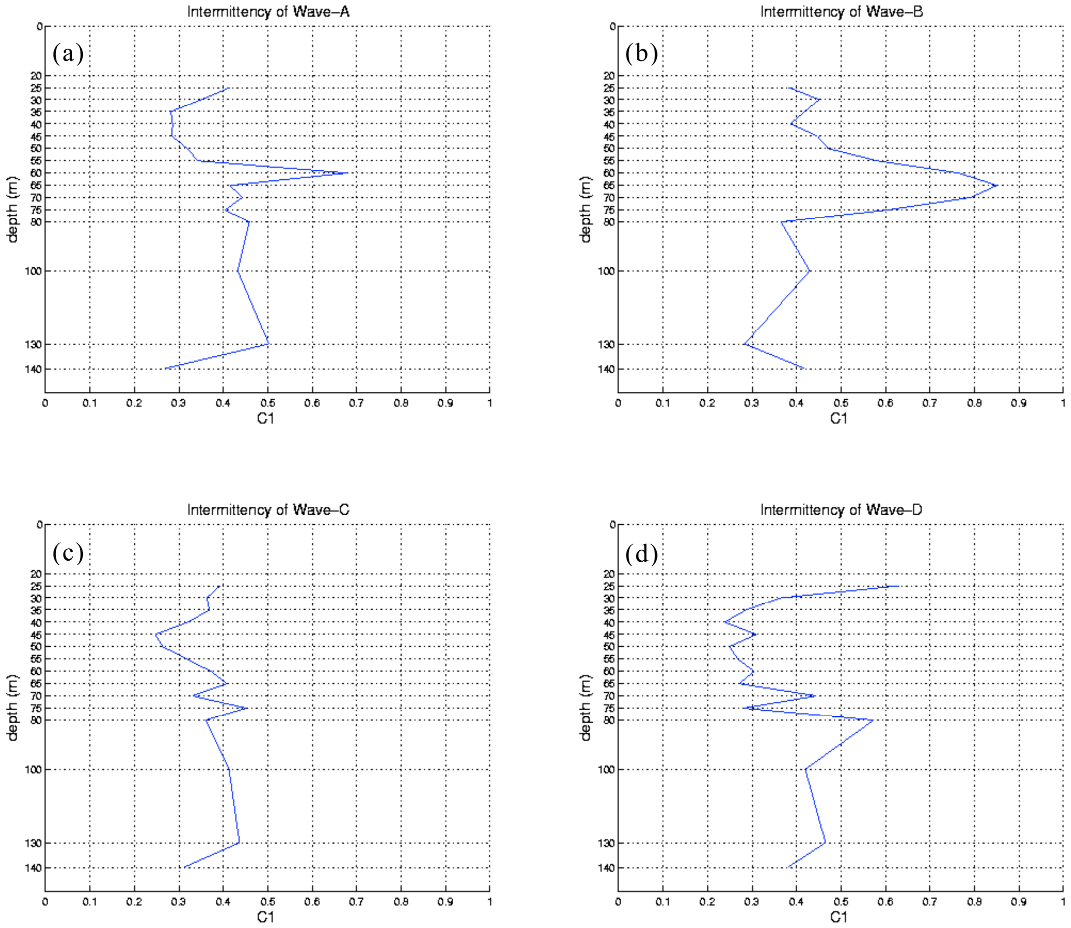

Figure 35. Depth dependent intermittency parameter C_1 on (a) Wave-A (IW-turbulence), (b) Wave-B (IS-turbulence), and (c) Wave-C (weak IW turbulence), and (d) Wave-D (turbulence-dominated).

V. COMPREHENSIVE ACOUSTIC SIMULATION SYSTEM

Mine detection sonar systems are popularly used to generate high-resolution images for acoustic target detection. Sensors, tactics, and platforms optimized to perform in deep oceans acoustically range-independent environments are usually inadequate in shallow, acoustically range-dependent littoral regions. Littoral regions tend to be reverberation-limited and hence are more complicated than the deep ocean.

Recently, the Generic Sonar Model (GSM) evolved into the Navy's Comprehensive Acoustic Simulation System (CASS) for acoustic and sonar analysis. It incorporates the Gaussian Ray Bundle (GRAB) eigenray modes to predict range-dependent acoustic propagation in the 600 Hz to 100 kHz frequency bands. Test rays are sorted into families of comparable numbers of turning points and boundary interactions. Ray properties are then power-averaged for each ray family to produce a representative eigenray for that family. Target echo level and interference levels are typically computed separately and then combined to get a signal-noise. Ambient Noise level is power-summed with the reverberation level to calculate total interference. The peak target echo is used to determine the signal level. A detection threshold is then applied to compute the Signal Excess (SE).

CASS/GRAB is one of the Navy's range-dependent propagation, reverberation, and signal excess acoustic models that can be used in both the active and passive sonar equations. The CASS model acts as the outer shell that computes range-independent monostatic and bistatic active signal–excess calculations and calls on the GRAB subset for the computation of eigenrays and propagation loss. GRAB uses ray bundles vice a ray path. This allows the amplitude of the Gaussian ray bundle to affect all depths to some degree, whereas with classic ray paths, amplitudes are local.

CASS/GRAB simulates the sonar performance reasonably well in the littoral zone, given accurate environmental input data such as bottom type, sound speed profile and wind speed, and accurate tilt angle of the sound source. However, the environmental data often lack the necessary resolution for accurate predictions. The effect of environmental variability on the acoustic propagation inaccuracy should be investigated.

Recently, Chu et al. and Vares (2004) investigated the acoustic uncertainty in the Yellow Sea continental shelf due to sound speed profile uncertainty using CASS/GRAB and found that the level of acoustic uncertainty depends on the location of the sound speed profile errors relative to the sound source location. When Gaussian-type noise is introduced into the sound speed profiles, the detection range anomaly has a non-Gaussian-like distribution in winter and a Gaussian-like distribution in summer, and is much larger in winter than in summer for the same noise intensity.

A. MODEL DESCRIPTION

Let (x, y) and z be the horizontal and vertical coordinates and r be the horizontal range. Let (P, P_0) be the acoustic pressure at (x, y, z) and at a reference distance (r_0) from the source. The horizontal and vertical slowness for the v th ray is represented by

$$p_{r,v} = \frac{\cos\theta_v}{c_v}, \qquad p_{z,v} = \frac{\sin\theta_v}{c_v} \tag{30}$$

where c_v is the sound speed, and θ_v the horizontal inclination angle. The travel time ($T_{z,v}$) at the field-point depth z is computed from the boundary value (T_v) by

$$T_{z,v} = T_v + p_{z,v}(z - z_v). \tag{31}$$

Volume attenuation and boundary reflection losses are represented by the pressure ratio Γ_v and phase shift Φ_v, respectively. Rayleigh bottom "forward" loss is determined from the first three columns of the geo-acoustic table for various bottom types. Duplicate grain size indexes are listed to cover all commonly used geo-acoustic bottom types. Six geo-acoustic parameters are used to calculate.

$$\Gamma_v = \Pi\gamma_{s,v} \times \Pi\gamma_{b,v}, \qquad \Phi_v = \sum\phi_{x,v} + \sum\phi_{b,v} \tag{32}$$

where $\gamma_{s,v}$ is the surface reflection coefficient amplitude; $\gamma_{b,v}$ is the bottom reflection coefficient amplitude; $\phi_{s,v}$ and $\phi_{b,v}$ are the surface and bottom phase shifts.

The energy conservation for simple geometric acoustics states that energy in a ray tube is equivalent to the energy in the ray tube at a reference range. Different from the classical ray theory, the Gaussian ray bundle amplitude of the vth test ray at target depth Z(Ψ_v) is computed by [30]

$$\Psi_v = \frac{\beta_{v,0}\Gamma_v^{\,2}}{\sqrt{2\pi}\sigma_v p_{r,v} r}\exp\left\{-0.5\left[\frac{z-z_v}{\sigma_v}\right]^2\right\},$$

where σ_v is the standard deviation and $\beta_{v,0}$ is the source-dependent conversion term to equate energy within a Gaussian ray bundle with a geometric-acoustic ray tube,

$$\beta_{v,0} = r_0^{\,2} p_{r,v,0}\Delta\theta_{v,0} P_0^{\,2}. \tag{33}$$

Summation of the Gaussian ray bundle amplitudes over all the rays,

$$\Psi_e = \sum_v \Psi_v,$$

is the Gaussian eigenray and its square root, $A_e = \sqrt{\Psi_e}$, and is defined as the Gaussian eigenray amplitude (A_e). The ratio, Ψ_v / Ψ_e, represents the weight of the v th ray. The acoustic characteristics are the weighted averages of the ray bundle properties such as the source angle, horizontal slowness, vertical slowness, boundary phase shift, and travel time,

$$\theta_e = \Psi_e^{-1}\sum_v \Psi_v \theta_{v,0}, \quad p_{r,e} = \Psi_e^{-1}\sum_v \Psi_v p_{r,v}, \qquad p_{z,e} = \Psi_e^{-1}\sum_v \Psi_v p_{z,v}$$

$$\Phi_e = \Psi_e^{-1}\sum_v \Psi_v \Phi_v, \quad T_e = \Psi_e^{-1}\sum_v \Psi_v T_{z,v}. \tag{34}$$

From these representative eigenrays, coherent or random propagation loss is calculated.

GRAB contains sound speed conversion models such as Leroy's equation and Millero-Li's equation, which suggest adjustments to the original Chen-Millero equation. The Wilson's equation for temperature-salinity-sound speed conversion is used. GRAB defaults to Leroy's equation for sound speed conversions, whereas numerically stable polynomials are fit to Wilson's data.

B. MODEL SIMULATION

Use of CASS/GRAB needs environmental input: surface, volume, and bottom. The surface wind data over the ocean are highly uncertain, as is the bottom type data. Many parts of the world have inadequate bottom type mapping in littoral regions and covert reconnaissance may be the only source of even approximate bottom information. Bottom types can vary greatly in a small area and affect actual acoustic performance as the bottom interaction changes.

The sound speed profile is calculated using the Wilson equation. With this sound speed profile, the CASS/GRAB is integrated with different wind speeds, bottom types, and tilt angles. Differences in acoustic transmission are analyzed to determine the effects of uncertain wind and bottom type.

C. MODEL INPUTS

The frequencies of 3.75 kHz and 7.5 kHz with a bandwidth of 500 Hz and four different source/transmitter depths of 5, 15, 100, and 200 m in different combinations are applied to run the model. Besides the frequencies and source depth input, the GRAB eigenray model uses the monostatic active mode with parameters of the maximum surface/bottom reflections < 30, modeling ranges from 0 to 10 km with 0.5 km increments, and a vertical angle from -89° to 89° with 0.1° increments. The surface wind collected by the CMB during the internal solitary wave event has a maximum wind speed of 4.2 m/s and a minimum of 3.3 m/s (Figure 36). The mean wind speed of 3.76 m/s is then applied to the inputs. The West Philippine Sea is relatively deep water with a bottom depth of around 5,000 to 6,000 m. The common bottom sediment types of this deep ocean are mud and clay.

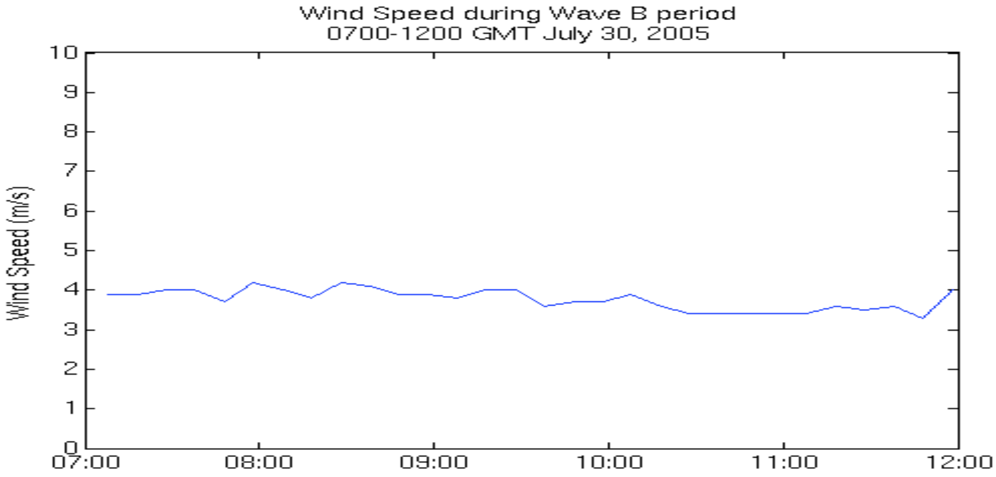

Figure 36. Wind Speed during the Wave Period (0700–1200 GMT July 30, 2005)

The water temperatures above 20 meters were collected by the CMB at five different depths (0, 3, 5, 18, and 20 meters) with 10-minute record intervals. Between 20 meters and 140 meters they were recorded by the thermistor chain at fourteen different depths (25, 30, 35, 40, 45, 50, 55, 60, 65, 70, 75, 80, 100, 130, and 140 meters) with fifteen seconds record intervals, and from 140 meters to 760 meters, the XBT data (Figure 37) at the same time period were used.

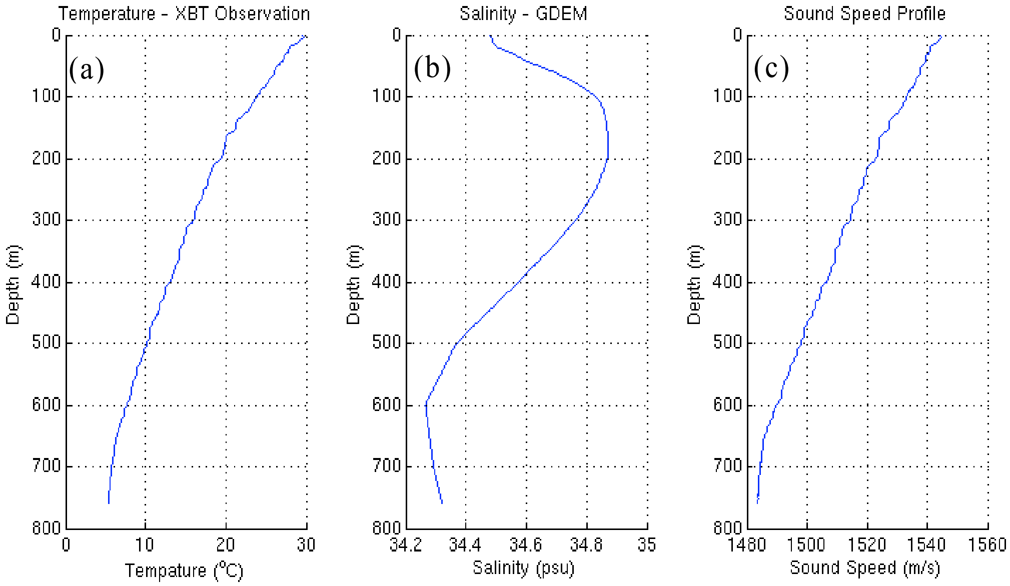

Figure 37. XBT (a) Temperature (°C) (b) Salinity (psu) – GDEM (c) Sound Speed (m/s)

In order to get the total sound speed profiles (SSP) from the surface to the sea bottom, the Generalized Digital Environment Model (GDEM) (Figure 38), water temperatures below 760 meters and the salinity data from surface to bottom was interpolated to the true measurement data. The CSIRO Matlab Seawater code was used to produce 105 SSP inputs to the CASS model with sixteen-meter range intervals (the floating speed of the CMB is 0.267 m/s). A highly regarded range-dependent transmission loss model, the PE model, is not often used when the frequency is over 1kHz, as in this case, because of excessive model run time. CASS/GRAB is sufficiently accurate and executes more quickly. However, the output depth scales of the Transmission Loss (TL) in the PE model are a reference to apply to the CASS model to set the inputs of the target depths in order to generate the clear figure of TL in different ranges and depths.

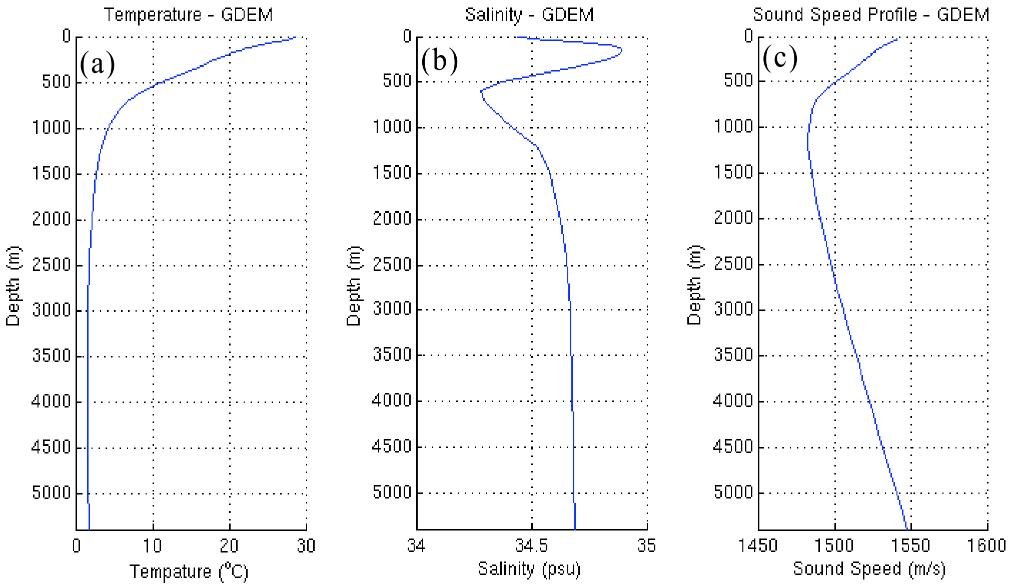

Figure 38. GDEM data (a) Temperature (°C) (b) Salinity (psu) (c) Sound Speed (m/s).

VI. TRANSMISSION LOSS DUE TO INTERNAL SOLITONS

A. RANGE-DEPENDENT

The IS-turbulence Wave-B during 0700–1200 GMT July 30, 2005 has 1201 temperature records from the thermistor chain. For high efficiency and the best resolution requirement, the one-minute time intervals with sixteen-meter range intervals are used in the CASS/GRAB model. A total of 105 sound speed profiles (Figure 39) obtained during 0752–0936 GMT July 30 are used in this study. It is assumed that these profiles represent the instantaneous sound speed structure across a distance of 1.664 kilometers.

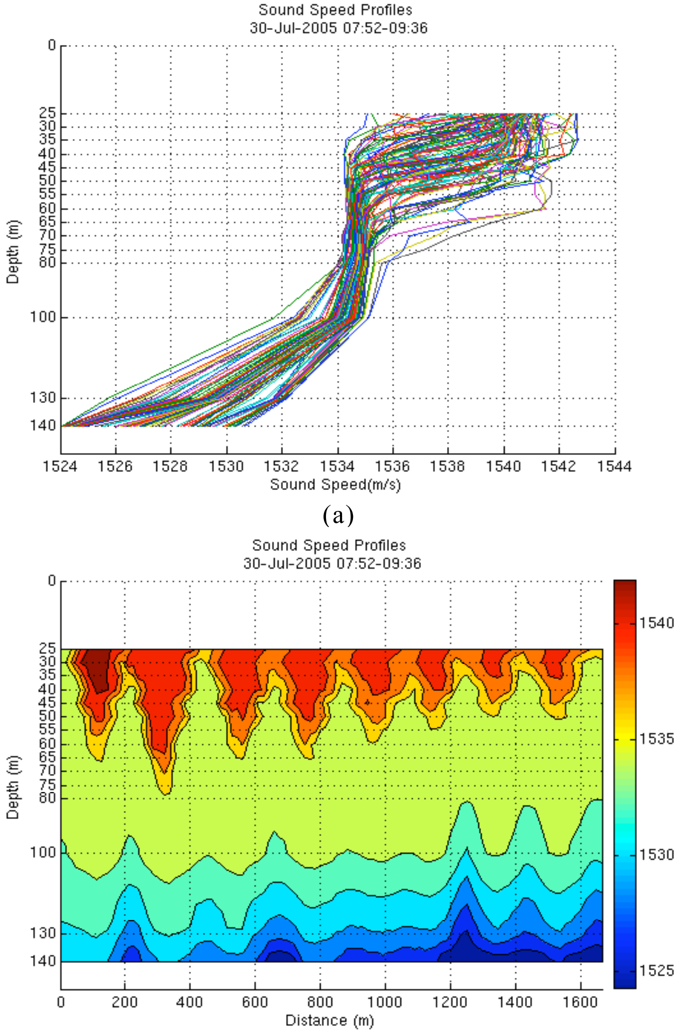

(a)

(b)

Figure 39. (a) Range-dependent 105 Sound Speed Profiles, and (b) SSP contour of the upper layer range from 07:52 to 09:36 July 30.

Figures 40 and 41 show the Transmission Loss (left) and the ray-trace (right) of two frequencies of 3.75kHz and 7.5kHz at the source depth of 5, 100, and 200 meters. Due mostly to volume attenuation, the higher frequency (7.5kHz) cases have larger Transmission Loss (TL) than the lower frequency (3.75kHz) cases. As source depth increases, the strength of the shadow zone caused by acoustic energy reflected by the ocean surface is greatly reduced. From the TL figures, we can see that caustics appear 1 to 2 kilometers down range, near the ocean surface, and in both frequencies can be noticed for a source depth of 100 meters. When the source depth is at 200 meters, we can see that caustics again appear 1 to 2 kilometers down range, but at depths deeper than for the 100 meter source. From the ray trace figures, it can be seen the above events are caused by the surface reflection. In shallow source depths of 5 meters, the rays are all downward propagation, and until the vertical angle is greater than 46°, bottom reflection occurs which extends the propagation. We can conclude that the deeper the source, the more acoustic wave propagation reaches the shadow zone and the less transmission loss there is in this area.

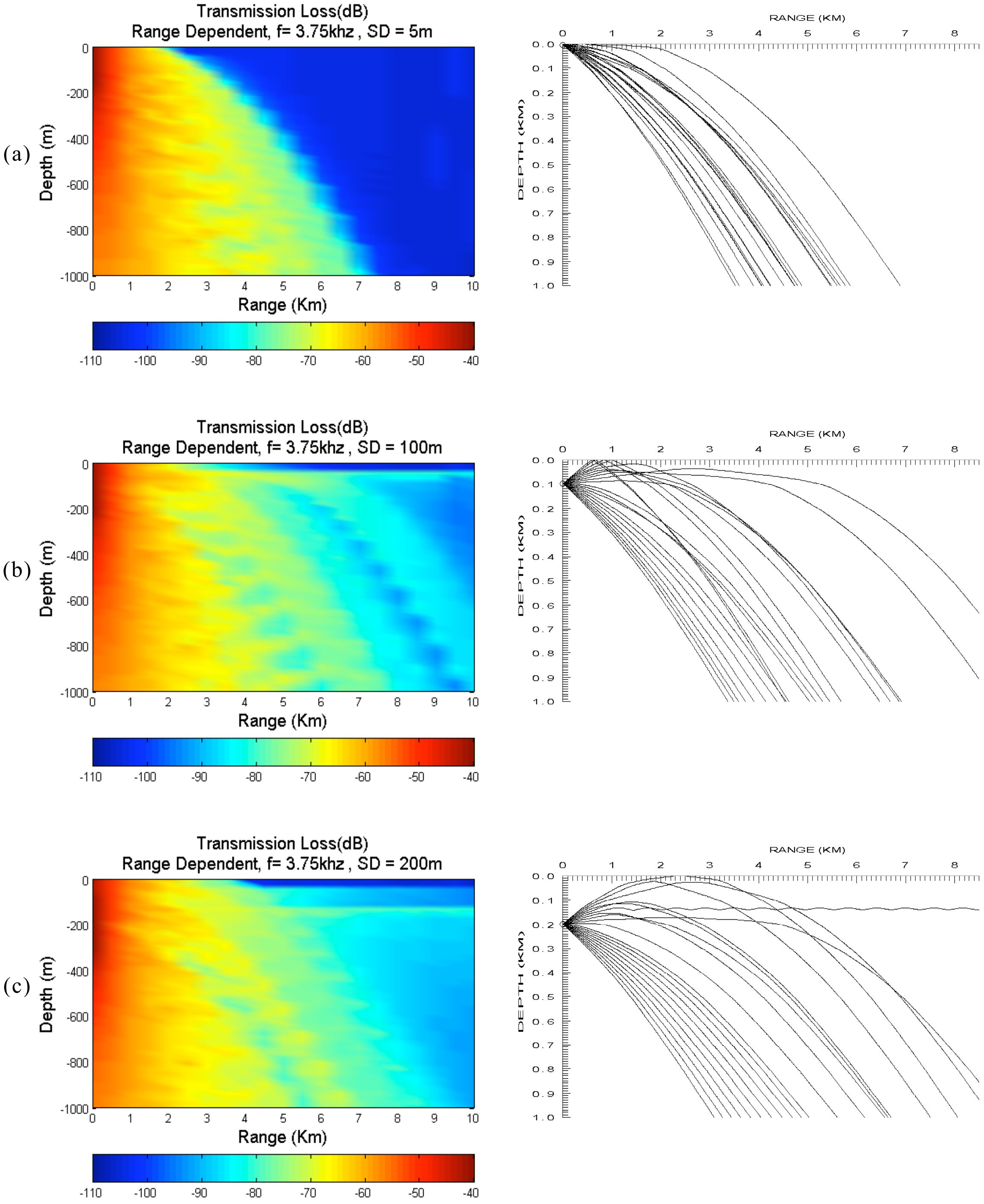

Figure 40. Transmission Loss (left) and Ray trace (right) of Range-Dependent cases of f = 3.75 kHz at different source depths of (a) 5, (b) 100, and (c) 200 meters.

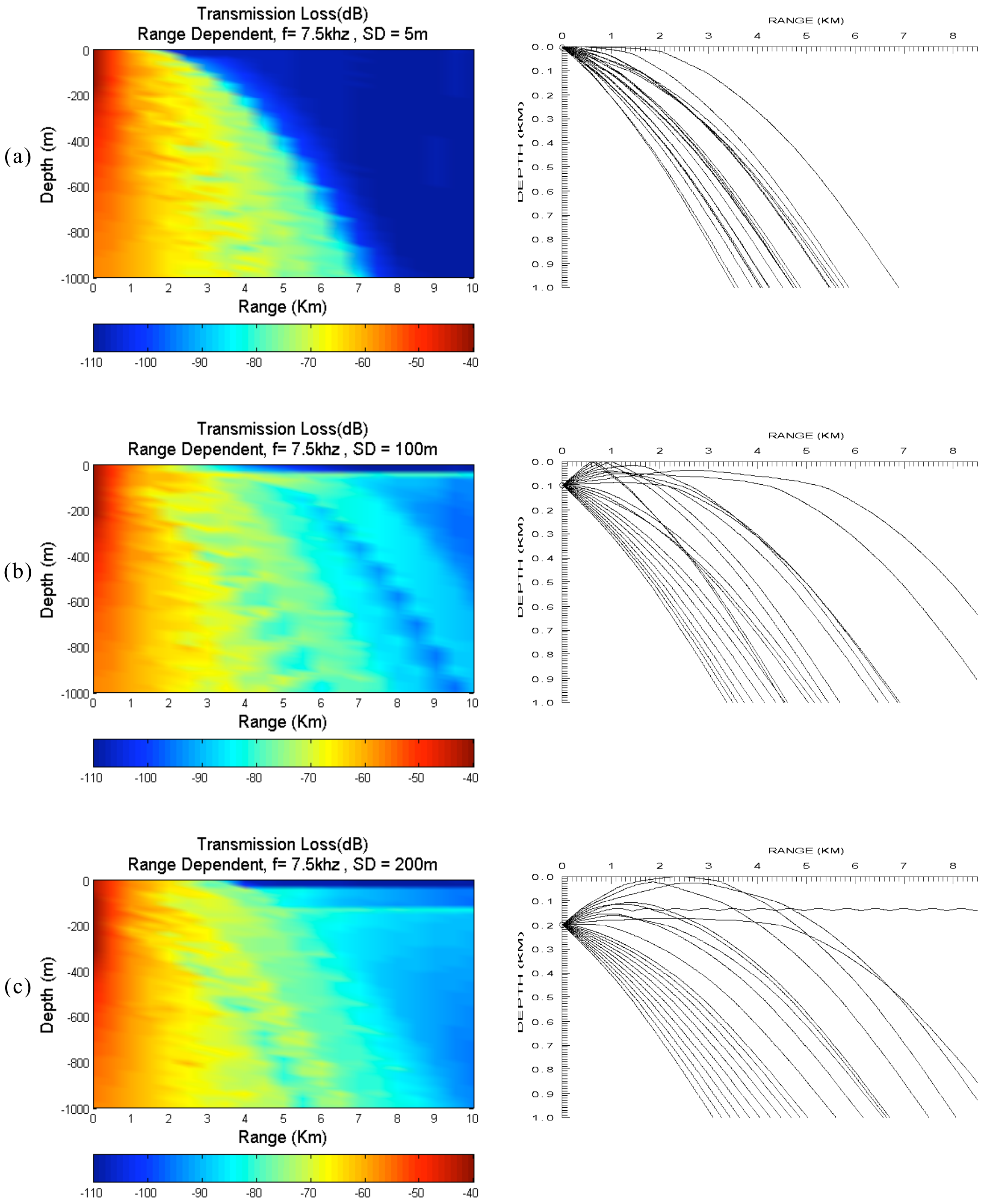

Figure 41. Transmission Loss (left) and Ray trace (right) of Range-Dependent cases of f = 7.5 kHz at different source depths of (a) 5, (b) 100, and (c) 200 meters.

Despite the soliton, a shadow zone is clearly seen at a range of about 3 kilometers at depth about 50 meters. Transmission loss is at least 100 to -110 decibel (dB) in this shadow zone. This is due to the downward reflection and refraction of rays. For the source depth of 100 m, the surface reflection at a range of around 0.6 to 1 kilometers causes caustics at a depth of about 45 m (Figure 42). When the source depth is at 200 m, a sound channel can be noticed at a depth of 140 meters (Figure 43).Again surface reflection and downward refraction causes caustics.

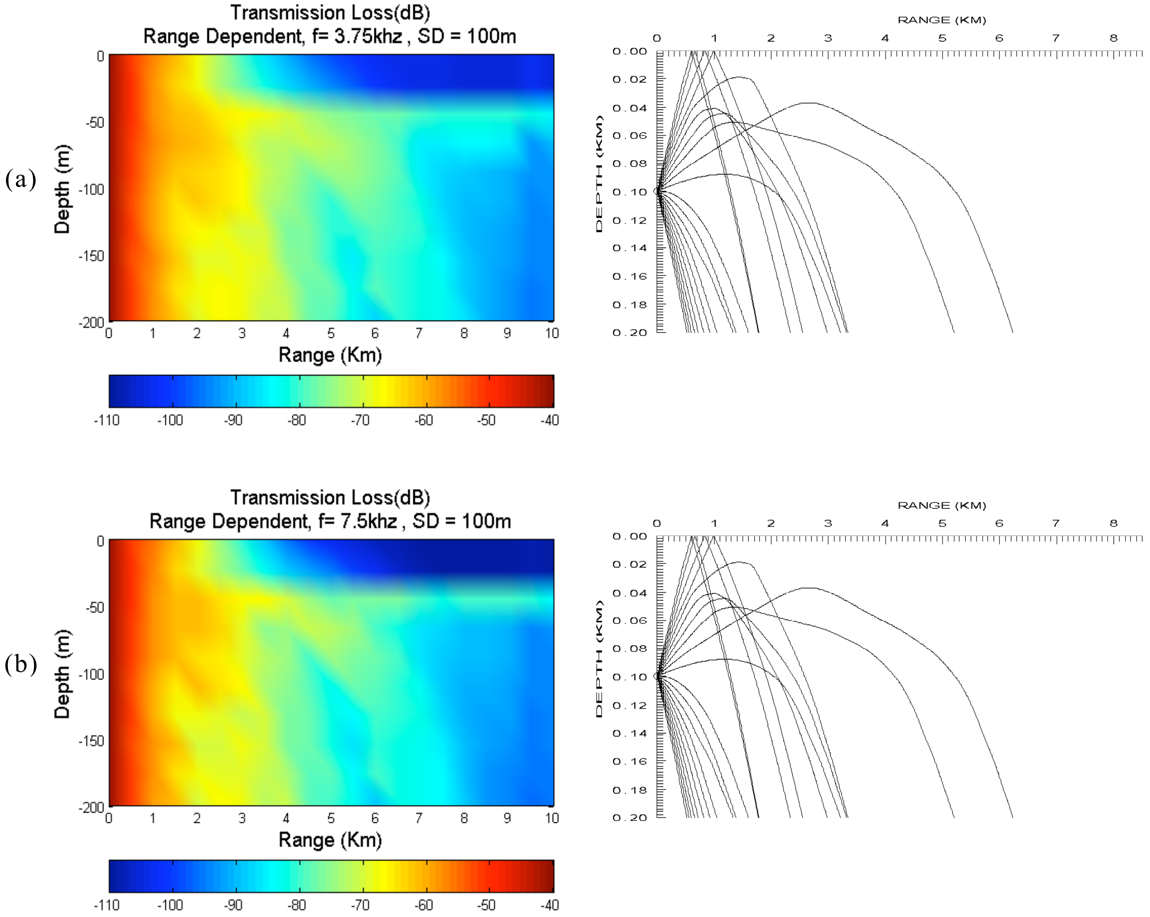

Figure 42. Surface Reflection and Caustic at a depth of about 45 meters at source depth of 100 m of (a) f = 3.75kHz, (b) f = 7.5kHz.

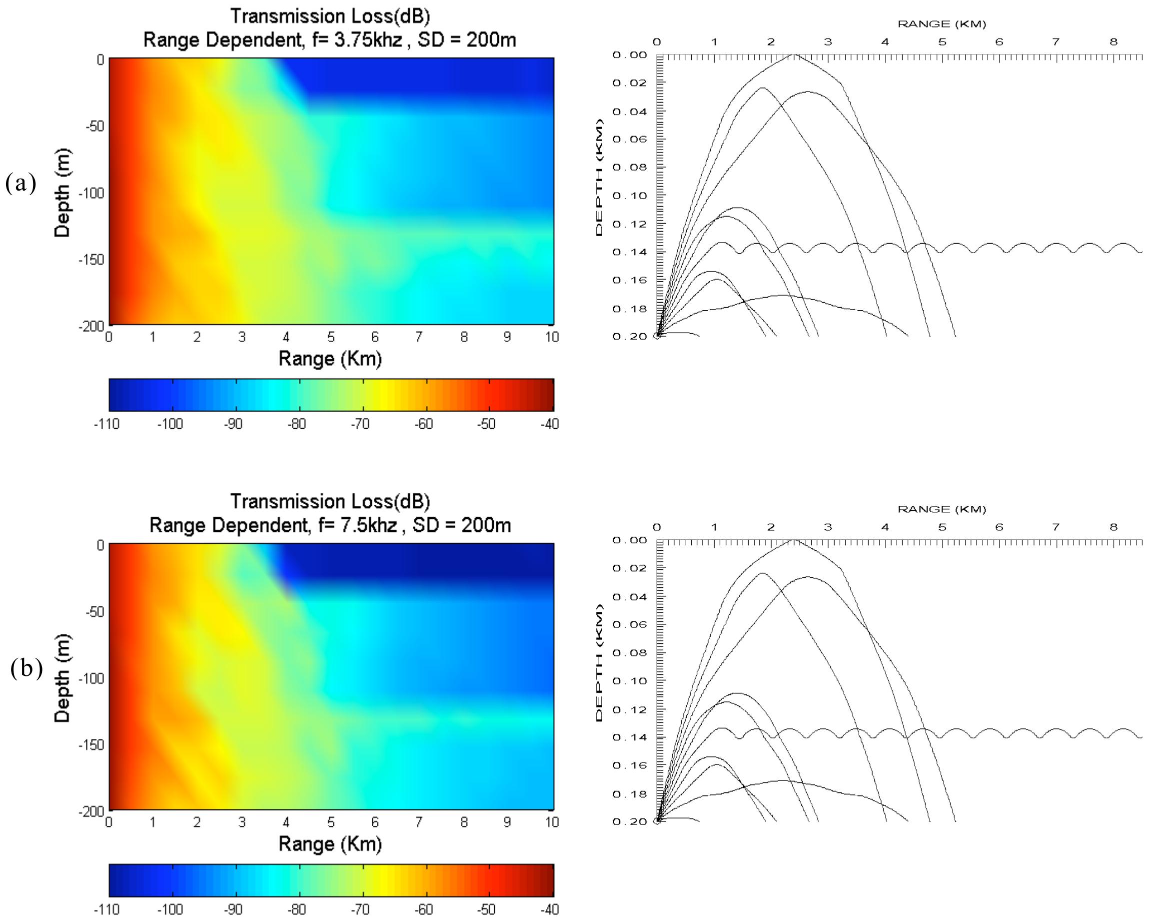

Figure 43. Surface Reflection and Sound Channel at depth of about 140 meters at source depth of 200 m of (a) f = 3.75kHz, (b) f = 7.5kHz.

B. RANGE-INDEPENDENT

The mean temperature (Figure 44) of the 105 sound speed profiles is used to represent the range-independent without IS-turbulence event. After averaging all of the sound speed profiles, the IW-turbulence and IS-turbulence characteristics, as well as the turbulence from surface wind effect are diminished, and there are no bottom sediment effects at the shorter ranges here — the interesting acoustic events occur before the energy can bounce off the bottom and back up to the surface. This condition can be assumed as an ideal case of a fair weather with a mild wind. The shadow zone at the surface occurred in range-dependent deeper source depth cases (100 and 200 meters) but do not occur in any of the range-independent cases. The caustics near the surface are different in nature and the sound channel cannot be seen.

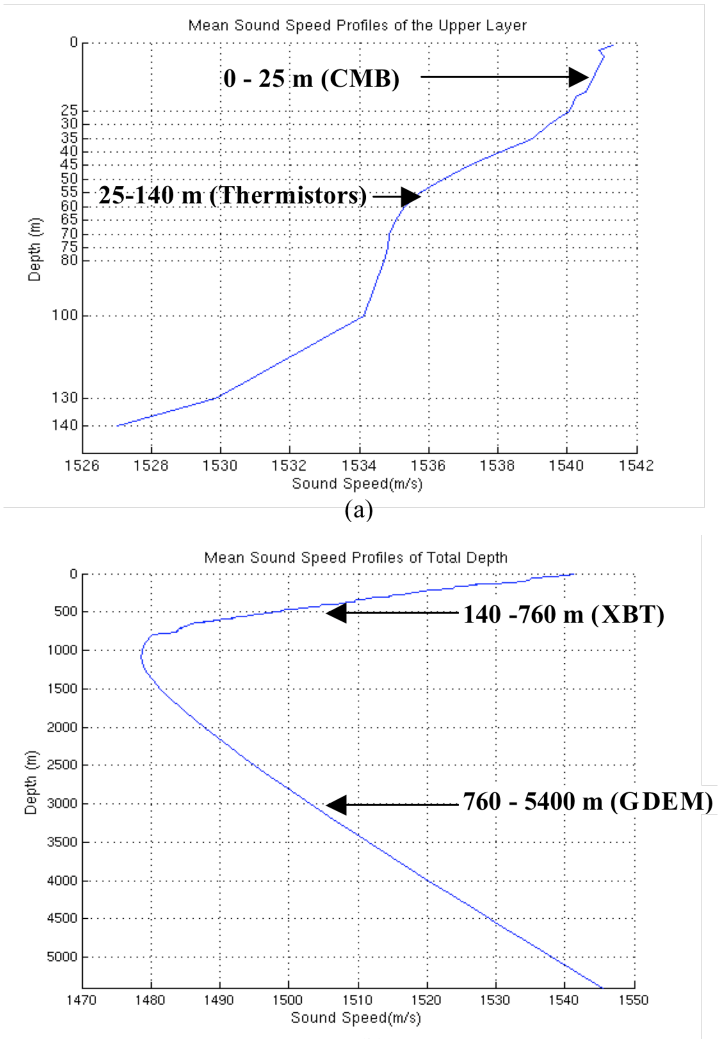

(a)

(b)

Figure 44. Mean sound speed profiles of the (a) upper layer, (b) total depth.

The maximum transmission loss at the higher frequency of 7.5 kHz (Figure 46) has a larger value of about -95 dB than the lower frequency of 3.75 kHz (Figure 45) of about -85 dB. This shows the same effect that the high frequency acoustic wave energy will have larger attenuation, and absorption, and large transmission loss.

From the ray trace, the surface reflection and the downward refraction still exist at the deeper source depth cases, but the sound channels at deep source depth do not occur in range–independent cases (Figure 47).

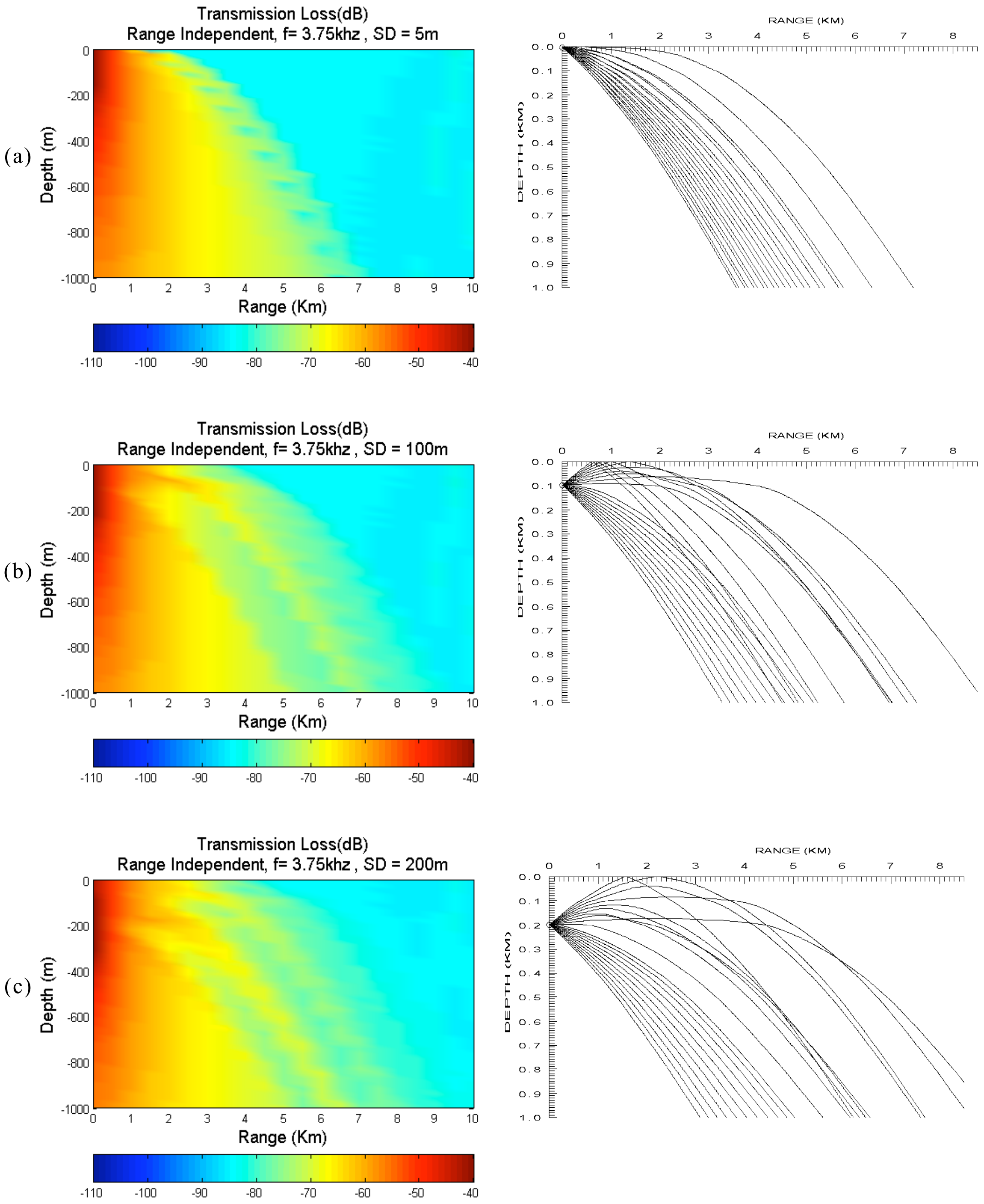

Figure 45. Transmission Loss (left) and Ray trace (right) of Range-Independent cases of f = 3.75 kHz at different source depths of (a) 5, (b) 100, and (c) 200 meters.

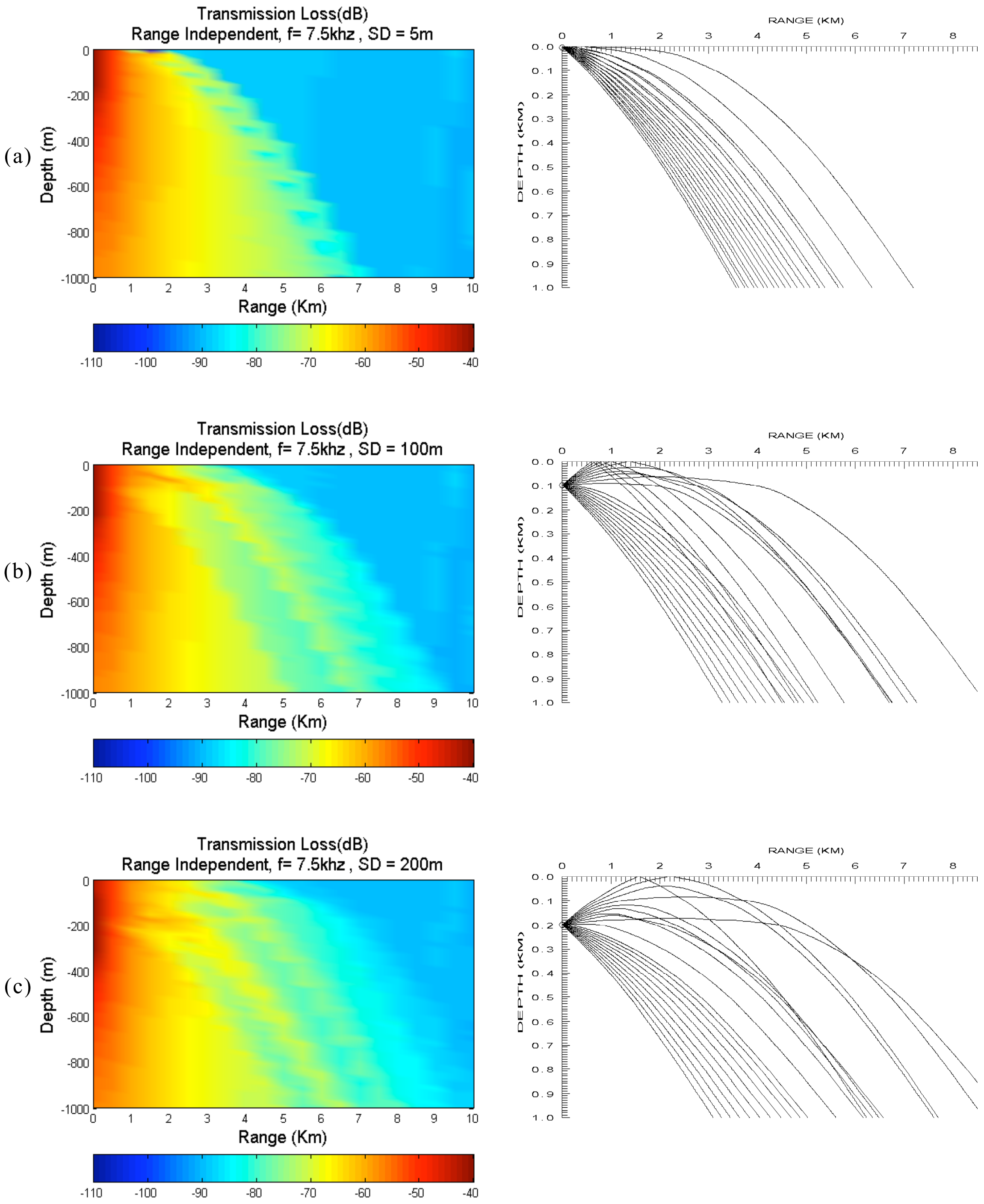

Figure 46. Transmission Loss (left) and Ray trace (right) of Range-Independent cases of f = 7.5 kHz at different source depths of (a) 5, (b) 100, and (c) 200 meters.

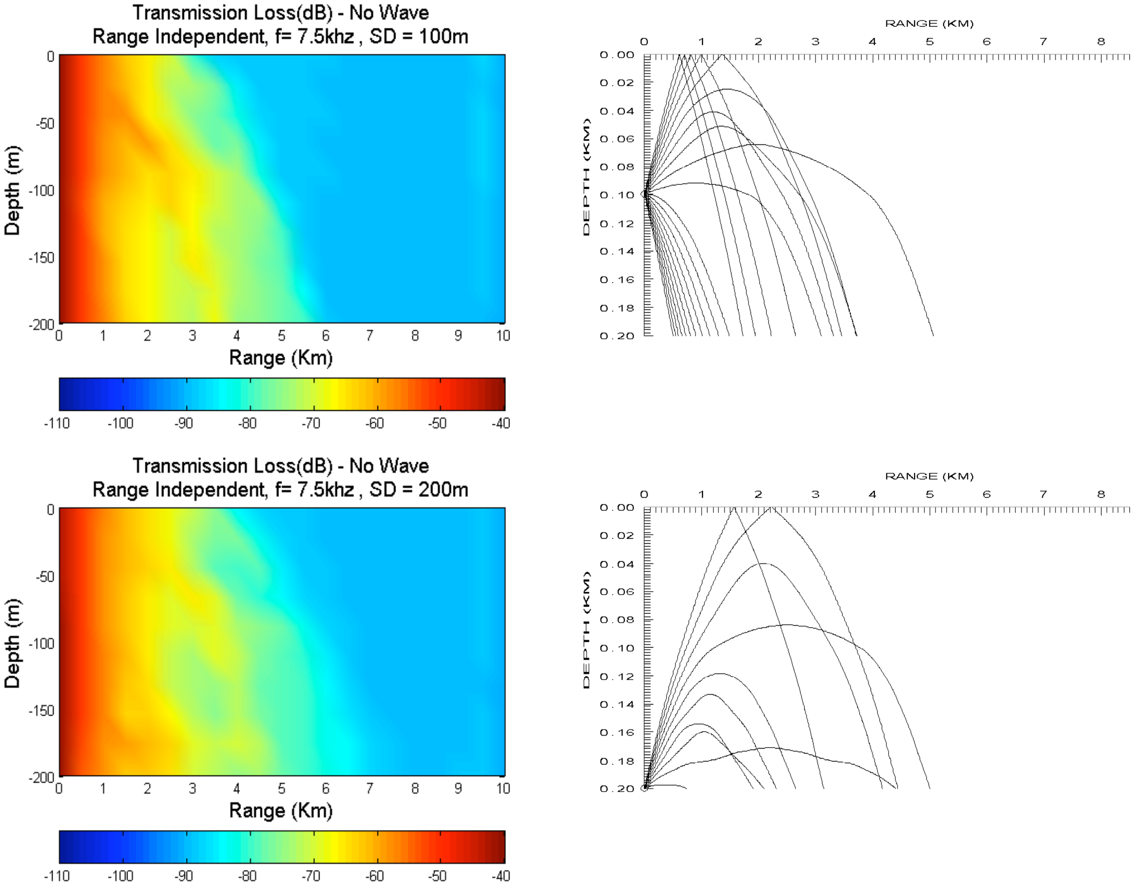

Figure 47. No sound channels or caustics occur on deeper source depths of Range-Independent cases.

C. DIFFERENCE BETWEEN THE RANGE-DEPENDENT AND RANGE-INDEPENDENT CASES

Figure 48 shows the transmission loss difference ($TL_{diff} = TL_{rd.} - TL_{ri}$) between the range-dependent IS-turbulence cases (Figures 40 and 41) and the range-independent cases with IW, IS and turbulence (Figures 45 and 46).

The TL difference on the left side of the interface is near zero value and indicates that the TL in either the range-dependent or the range-independent cases has the same magnitude of the TL near the source. The TL difference on the right side of the interface has values of -20 dB in shallow source depths of 5 m (Figure 48a) cases and it indicates clearly that the TL in the range-dependent case is larger. The TL difference at the source depth of 100 meters (Figure 48b and 49) has a focusing of a value from +5 dB to +20 dB at the convergence zone. At source depths of 100 and 200 meters, the TL difference also has a value of from +5 dB to +20 dB. The shadow zones at the surface (Figure 48b, and c) can be seen as proof that the internal solitons and wind conditions affect acoustic wave propagation dramatically near the surface.

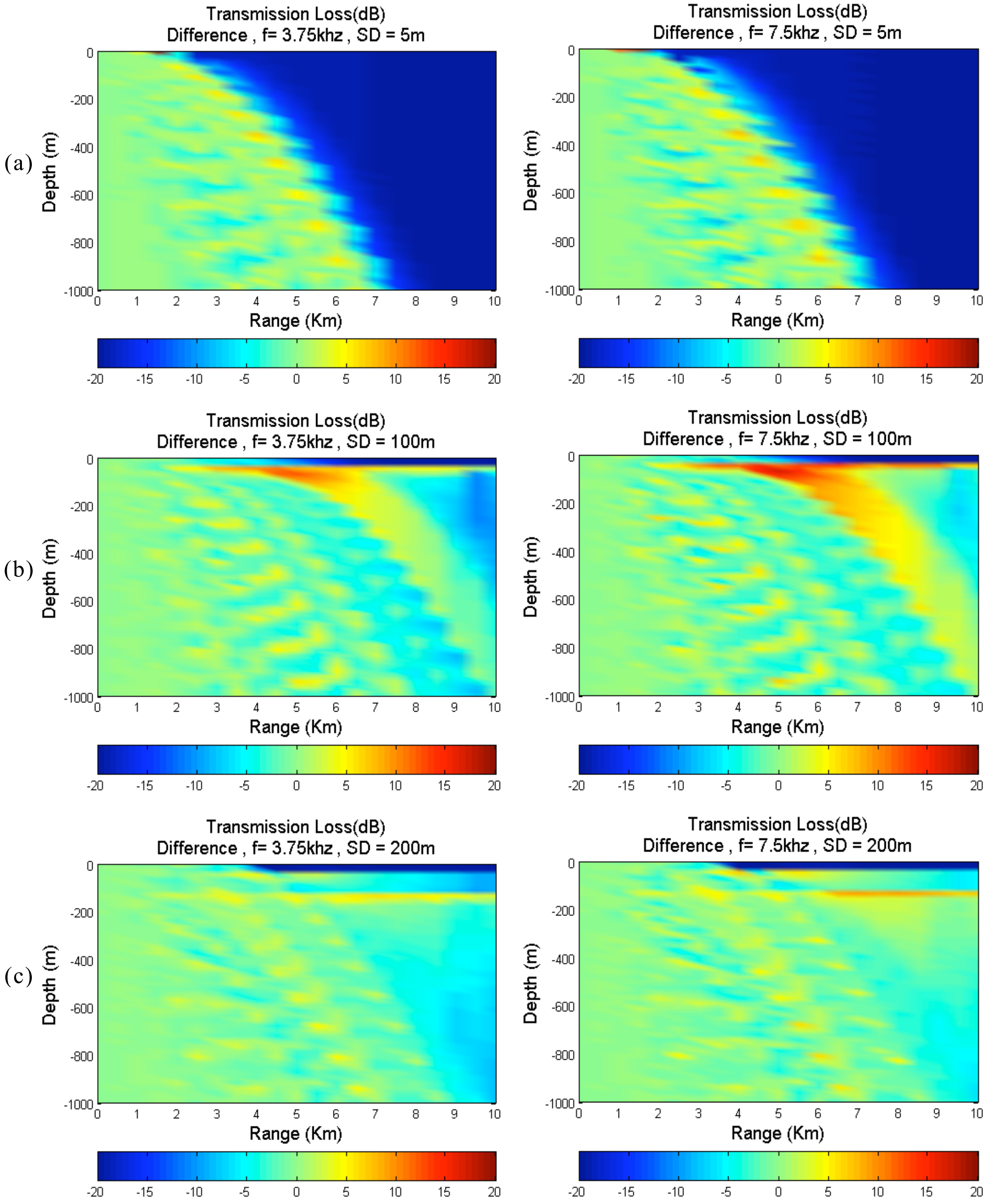

Figure 48. Transmission Loss difference of f = 3.75 kHz (left) and f = 7.5 kHz (right) at different source depths of (a) 5, (b) 100, and (c) 200 meters.

All the results show that acoustic waves propagating through internal solitary waves will cause larger transmission losses than in stable ocean conditions. For mine detection, very high frequency sonar is usually used to get clear video images in the water. But the higher frequency means a larger transmission loss increasing with the range. Another way to deal with this problem is to make the source depth deeper. The acoustic energy will penetrate into the shadow zones, through the shadow zone caused by this internal solitary wave and wind effects still exists to a depth of 45 meters. The possible methods to compensate the large TL at the surface, away from the source, are the towed array active/passive sonar and the Unmanned Undersea Vehicles (UUV) that can be deployed away from the platform and positioned to a designated depth to pass through the shadow zone, extend the detection range, and avoid direct damage to the platform.

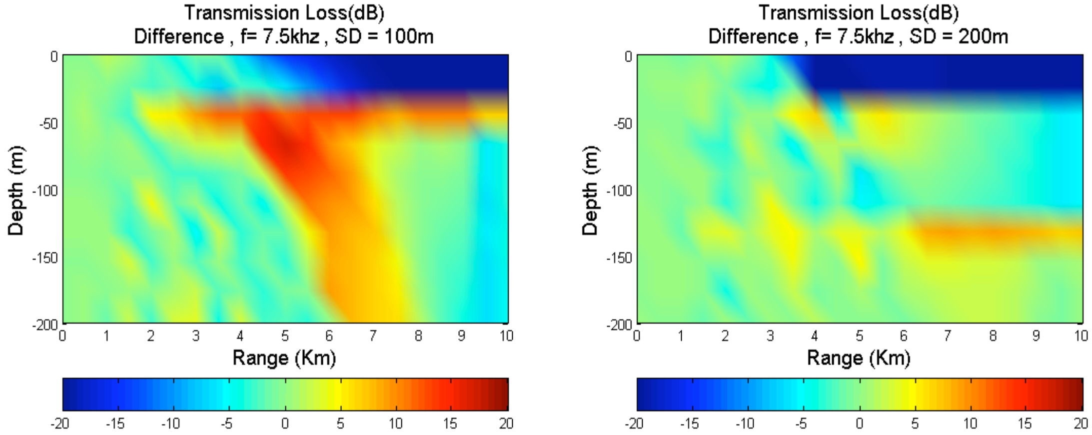

Figure 49. The positive values of TL difference in (a) caustics in SD = 100 m and (b) sound channels in SD =200m.

VII. APPLICATION TO MINE DETECTION

A. MINE DETECTION AND IDENTIFICATION

The naval mines laid in the deep ocean usually are the floating mines. Once an area is determined to be a mined area, the problem becomes one of deterrence or blockade, and must consider the threat of damage to the naval platform and personnel. The mine countermeasures include several methods to prevent damage from mines in dangerous waters. The active technique is to clear via removal or destruction of the mines by minehunting and minesweeping. The most important step in minehunting and minesweeping is to detect and localize the mines.

Acoustics waves can propagate over hundreds, even thousands of miles in the ocean. As a result, sonar plays a major role in the underwater detection. The sonar with the higher frequency is usually used to obtain higher resolution for imaging the target. The second step in minehunting is to then identify whether the target is a mine or a non-mine objects, based on the acoustic features of the target. The acoustic features are the target's strength (TS), signal-to-noise ratio (SNR), target size and shape, target motion, target echo structure and target resonance. The TS and SNR are the important acoustic features of mine detection and identification when using high frequency sonar.

B. TARGET STRENGTH OF MINES

The performance of mine detection can be quantified in terms of the SNR in the active sonar equation (Nicholas P. C, et al.).

$$SNR = S - N$$

where S and N are the signal and the noise levels in decibels (dB). The signal level is the strength of the target echo, including the source level (SL) relative to $1\mu Pa$ at 1yd, the reflection or scattering by the target of target strength (TS), and the two-way transmission loss (TL) from the sonar traveling to the target and back toward the sonar. The signal level can be expressed as,

$$S = SL + TS - 2TL\,. \tag{35}$$

The noise level includes all kinds of interference, including the parameters determined by the sonar, the self-noise level (SN), and parameters determined by the medium, the ambient noise (AN) and the reverberation level (RL). The ambient noise and reverberation are modified by the receiver Directivity Index (DI). The flow noise component (noise generated by the flow of water around the sonar) of the self-noise may also be diminished by the DI. The noise level can be expressed as,

$$N = (NL - DI) = RL \tag{36}$$

The signal excess (SE) can then be combined as,

$$SE = SL + TS - 2TL - N - DT \tag{37}$$

The parameter TS in active sonar refers to the echo reflected by the target. The target strength of the submarines and mines are of high interest to the military. The TS is defined as 10 times the logarithm to the base of the ratio of the intensity of the sound returned by the target; TS can be expressed as,

$$TS \equiv 10 \log \frac{I_r}{I_i} \tag{38}$$

where I_r = intensity of return at 1yd ;

I_i = incident intensity

The naval mines are usually quasi-cylindrical objects a few feet long to 1–2 feet in diameter, flat or round on one end, and containing protuberances, depressions, and fins superposed on the cylindrical shape. The beam aspects on the larger flat portion of the shape and normal to the incident direction have relatively larger TS than other aspects. Measured TS of about +10 dB (Table 1) within a few degrees of the beam aspect, become much smaller at the intermediate aspect. The TS of a cylinder of length L, radius a, at wavelength λ is expressed as (Urick, 1967)

$$TS \equiv 10 \log \frac{aL^2}{2\lambda} \tag{39}$$

TS of different geometric shapes and forms have been found theoretically. Table 2 lists the common shape of a mine's target strength that has been previously determined.

Table 1. Nominal Values of Target Strength (From Urick, 3rd edition)

Target	Aspect	TS, dB
Submarines	Beam	+25
	Bow-stern	+10
	Intermediate	+15
Surface ships	Beam	+25 (highly uncertain)
	Off-beam	+15 (highly uncertain)
Mines	Beam	+10
	Off-beam	+10 to -25
Torpedoes	Bow	-20
Fish of Length L, in.	Dorsal view	-19 log L -54 (approx.)
Unsuited swimmers	Any	-15
Seamounts	Any	+30 to +60

Table 2. Target strength of Simple Form (From Urick, 3rd edition)

Form	Target Strength	Direction of Incidence	Conditions
Sphere	$10\log\frac{a^2}{4}$	Any	$ka >> 1$ $r > a$
Cylinder	$10\log\frac{aL^2}{2\lambda}$	Normal to axis of cylinder	$ka >> 1$ $r > L^2/\lambda$
Plate (Finite) Any shape	$\left(\frac{A}{\lambda}\right)^2$	Normal to plate	$kl >> 1$ $r > L^2/\lambda$

* a = Radius, L = Length, λ=wavelength, $k = 2\pi / \lambda$

The CASS/GRAB model results show that the Transmission Loss difference between the range-dependent and range-independent cases in shallow depths reaches to 20 dB and is much larger then the TS of mines of +10 dB and of submarines of +15 dB. In undersea warfare, the internal solitary waves will be an important factor for mine and submarine detection.

C. APPLICATION IN MINE DETECTION

1. Mine Hunting Sonar

The mine-hunting sonars can be categorized into (C. M. Mckinney)

a. Ahead Looking Sonar – Horizontal Scan.

b. Side Scan Sonar – Mapping.

c. Vertical Scan Sonar.

d. Downward Looking Sonar.

f. Acoustics Camera Sonar – Azimuth and Elevation Scan

Most of the surface ships equipped with the Ahead Looking Sonar, and the Side Scan Sonars are used as mine-hunters or mine-sweepers. The major applications for mine-hunting sonars are listed as:

a. Conventional Surface Ship Mine-hunting.

b. Mapping – Reconnaissance – Surveillance

c. Handheld Sonar.

d. Unmanned Submersibles: UUV

e. Swimmer Delivery Vehicle-Obstacle Avoidance

f. Obstacle Avoidance for submarines.

g. Obstacle and Mine Avoidance for Surface Fleet.

The development of mine-hunting sonar includes the capability of deeper VDS to counter the threat of mines in the deep ocean and still retains the capability for shallow water. The second development is the side scan sonars. They are usually operated on a high frequency with a fine resolution. Detection and identification can essentially be combined into a single operation. Another development of the continuous transmission or CTFM handheld sonar is a small widget that is easily provided to swimmers and has an aural display and earphones to operate mine warfare in the water. The AN/PQS-2 is an example that is still used by U.S SEALs and EOD divers and swimmers.

2. Marine Mammal Application–Dolphin

The U.S. Navy has found that the biological sonar of dolphins, called echolocation, makes them uniquely effective at locating sea mines. Other marine mammals, such as California sea lions, also have the ability to mark and retrieve objects in the ocean.

The U.S Navy Marine Mammal Program has trained dolphins to detect and locate tethered deep water mines off the ocean bottom (MK-4) as well as buried or bottom mines (Mk-7), and built a human/dolphin team to identify safe corridors in shallow water for the initial landing of troops ashore (MK-8). Real operation experience proves that marine mammals become more and more important in mine detection and identification tasks than a human sonar operator in Naval mine operations.

D. APPLICATION IN ANTISUBMARINE WARFARE

On October 26, 2006, the PLA-Navy Song-class diesel-powered attack submarine armed with wake-homing torpedoes and anti-ship cruise missile surfaced within the missile range near the U.S. Navy carrier battle group in deep waters off Okinawa without any detection. The increasing numbers of new technology submarines of the PLA-Navy gives the threat not only to the nearby countries but also to the U.S.

The submarine, a strategic weapon platform, is a menace anywhere and at any time. It has a ability to carry various types of weapons, such as torpedoes to attack surface ships and other submarines, anti-surface and anti-air missile (ASM/AAM), and mines. It is the maritime weapon posing the greatest threat to an aircraft carrier formation. In a complicated ocean environment, the quiet and stealthy characteristics make the anti-submarine warfare even more difficult.

1. Target Strength of Submarines

The target strengths of submarines are a significant factor in ASW. Not like sea mines which can only stay in the same location, submarines can change the position, depth, aspect, and even keep still in the water column or sit in the bottom. Thus, the target strength of submarines vary greatly from echo to echo on a single submarine, and from submarine to submarine, as measured by different operators at different.

The target strengths of submarines vary with different factors of different aspects, frequencies, depths, ranges, and pulse lengths. The TS of submarine showed in table 1 ranges from +10 dB to +25 dB. Comparing to the maximum TL_{diff} to -20dB in CASS/GRAB model result, the -15dB to +5 dB difference due to the Internal Solitary wave will make anti-submarine warfare more difficult.

2. Target Strength of Torpedoes

A torpedo is basically cylindrical with a flat round nose. An approaching torpedo with a hemispherical nose facing would have a target strength equal to $10\log(r^2/4)$ and the target strength in beam aspect could be approximated by the cylindrical formula as mine. Torpedoes of the PLA-Navy are mainly imported from Russia. The Shkval (Squall) rocket torpedo reportedly travels at a speed of 200 knots, five to six times faster than any current torpedoes and no U.S. defense can stop it.

The target strengths of submarines and torpedoes are important but not the only factor in ASW. The ocean environment, bathymetry and sonar's and the operator's ability are also very important. The acoustic model inputs with in situ data will give more information about wave propagation and will increase the detection probability in ASW.

VIII. CONCLUSION

Temperatures of the WPS upper layer (to 140 m deep) was sampled with high frequency from July 28 to August 7, 2005 from the coastal monitoring buoy with 15 thermistors attached. The isopycnal displacement is calculated from the temperature field, and the internal waves and solitons were observed.

A. PHYSICAL OCEANOGRAPHY

(1) Without internal waves and solitons (turbulence-dominated case), the temperature fluctuation has maximum values at the surface, decreases with depth to mid-depths (60-65 m deep), and then increases with depth to 140 m deep. Such depth-dependent (decreasing then increasing) pattern preserves during the internal wave propagation during 1000–1500 GMT July 29, 2005. However, this was altered during the internal soliton propagation to a pattern that increases with depth from the surface to 60 m deep, decreases with depth from 60 m deep to 100 m deep, and increases again with depth from 100 m to 140 m deep. Temperature fluctuation is enhanced with the internal wave and soliton propagation. Between the two, the internal solitons bring larger fluctuations.

(2) The observed temperature profile does not oscillate if there is no internal wave or soliton propagation. It oscillates in the upper layer above 50 m with internal wave propagation, and above 80 m with internal soliton propagation. The amplitude of the oscillation is much larger during internal soliton propagation (maximum amplitude around 4^{o}C) than internal wave propagation (maximum amplitude around 2^{o}C).

(3) The EOF analysis on the ispopycnal displacement shows that the first baroclinic mode dominates the variability for internal waves (86.0% of variance) and internal solitons (74.4% of variance). Maximum variability is located at different depths with 30 m for the internal waves and 60 m for the internal solitons. The amplitude of this mode fluctuates on two time scales with 4 CPH as a high frequency and around 5 cycles per hour as a low frequency for the internal waves, and on one time scale with a frequency of around 4 CPH for the internal solitons. The maximum amplitude is more than three times larger in the internal solitons than in the internal waves.

(4) Three types of thermal variability are identified: IW-turbulence, IS-turbulence, and turbulence-dominated. The power spectra of temperature at all the depths have multi-scale characteristics. For the IW-turbulence case and turbulence-dominated case, the spectral exponent β is in the range of (1, 2) and thus the temperature field is nonstationary with stationary increments. For the IS-turbulence case, the spectrum is quite different and the spectral exponent β is less than 1 for the low wavenumber domain.

(5) The structure function satisfies the power law with multifractal characteristics for the IW-turbulence case and turbulence-dominated case, but not for the IS-turbulence case. The internal waves increase the power of the structure function especially for high moments. The internal solitons destroy the multifractal characteristics of the structure function. The power law is broken approximately at the lag of 8 minutes, which is nearly half the period of the IS (with frequency of 4 CPH).

(6) The singular measure (representing the intermittency) satisfies the power law with multifractal characteristics for all three cases (IW-turbulence, IS-turbulence, and turbulence-dominated). The intermittency parameter C_1 does not change too much during the internal wave propagation, but increases drastically during the internal soliton propagation. This implies that the internal waves do not generate extra intermittency, but the internal solitons generate high intermittency.

(7) Multifractal analysis provides a useful framework to analyze ocean data when complex nonlinear processes exist. For the data collected from the CMB with attached thermistors, it clearly shows evident differences between internal wave and internal soliton propagation. The physical mechanisms causing these different effects need to be further explored.

B. ACOUSTIC DETECTION

The ray theory based CASS/GRAB model generates transmission loss and ray traces of both the range-dependent environment and range-independent environment. The transmission loss between these two cases proves that:

(1) The effects of the internal wave may create a significant shadow zone at relatively short ranges for a shallow sonar. As expected, as sonar depth increases, acoustic energy propagates through the internal wave more successfully.

(2) The detection range is significantly reduced by limiting reflection from the surface and the downward refraction of acoustic energy, even for deeper source depth cases. This causes a shadow zone near the surface. A variable depth sonar, can deal with the problem by moving the VDS to depths below sharp thermoclines. VDS is also applied to remove the source/sonar from the turbulent surface water and by using a low grazing angle, which in turn reduces the bottom reverberation and surface reverberation in shallow water.

(3) The range-dependent cases of internal solitary waves have larger transmission loss than the range-independent cases. The -3 dB differences in intensity scale have a factor of 0.5 (50%) off the original detection rate, and -10 dB will have a factor of 0.1 (10%) to the original detection probability. The sea mines' target strength is about +10 dB, varying with size and shape. A transmission loss difference of -20 dB will cause the mine detection under the internal solitary events to be 100 times more difficult.

Suggested future work in studying internal solitary wave effects on mine hunting in the western Philippine Sea using the CASS/GRAB would be as follows: 1) comparing the CTD and XTBs observed data with the thermistor observed data, 2) using deeper observed data from the thermistor, and 3) performing various input configurations in the CASS/GRAB model.

THIS PAGE INTENTIONALLY LEFT BLANK

APPENDIX A. ISOPYCNAL DISPLACEMENT

1. WAVE A

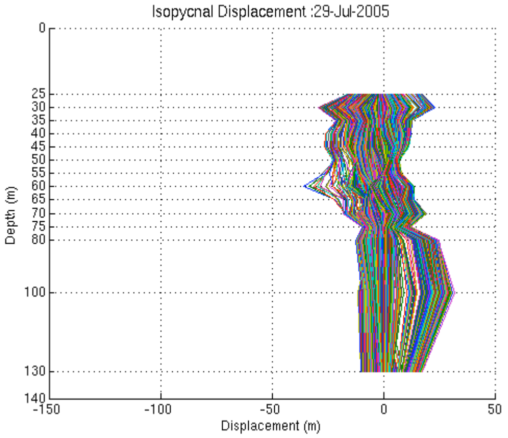

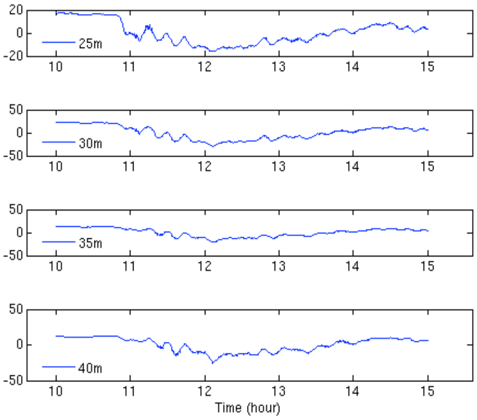

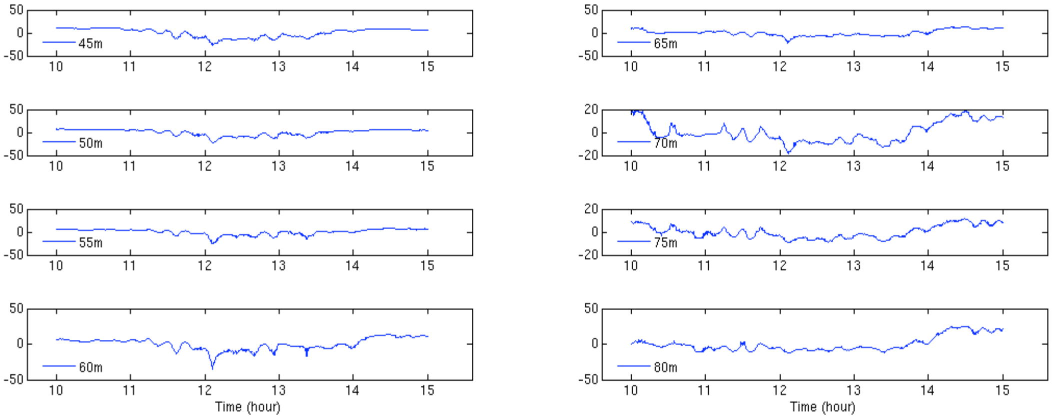

2. WAVE B

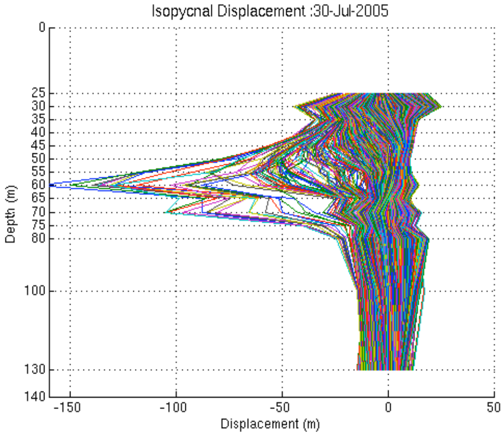
Isopycnal Displacement :30-Jul-2005
Depth (m)
0
25
30
35
40
45
50
55
60
65
70
75
80
100
130
140
-150
-100
-50
0
50
Displacement (m)

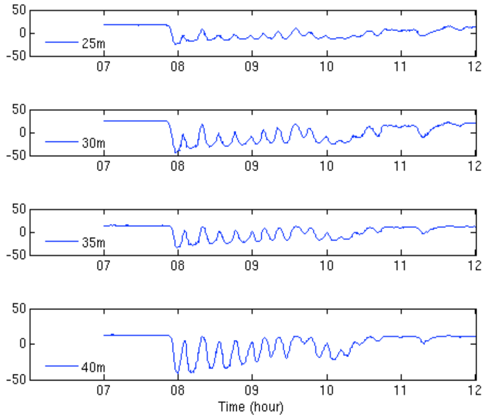
50
0
-50
25m
30m
35m
40m
07
08
09
10
11
12
Time (hour)

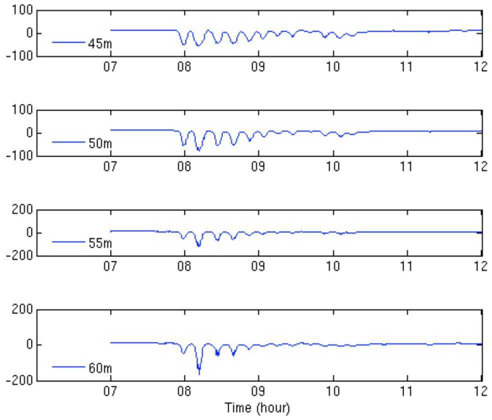
100
0
-100
200
-200
45m
50m
55m
60m
07
08
09
10
11
12
Time (hour)

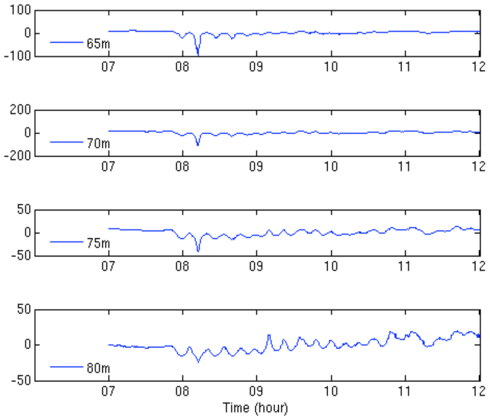
100
0
-100
200
-200
50
-50
65m
70m
75m
80m
07
08
09
10
11
12
Time (hour)

3. WAVE C

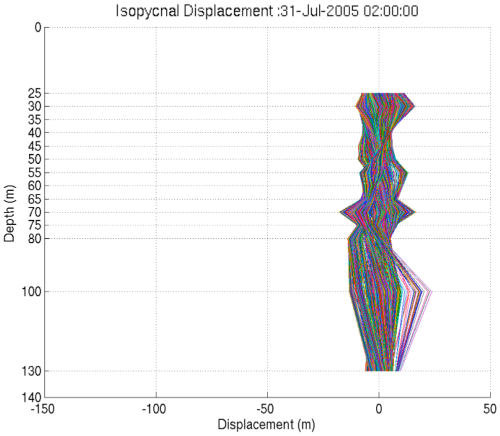
Isopycnal Displacement :31-Jul-2005 02:00:00
Depth (m)
0
25
30
35
40
45
50
55
60
65
70
75
80
100
130
140
-150
-100
-50
0
50
Displacement (m)

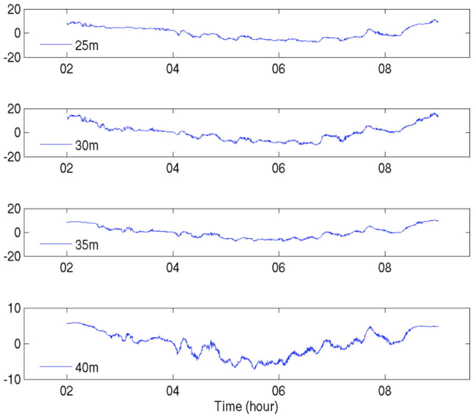
20
0
-20
25m
30m
35m
10
-10
40m
02
04
06
08
Time (hour)

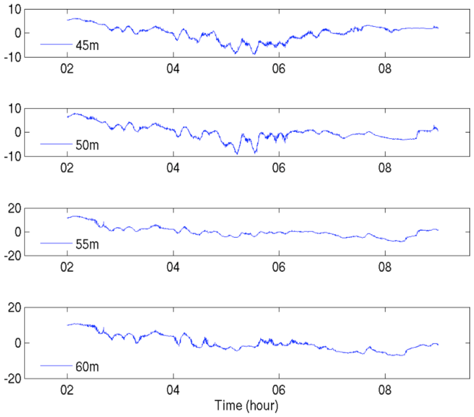
10
0
-10
45m
50m
20
-20
55m
60m
02
04
06
08
Time (hour)

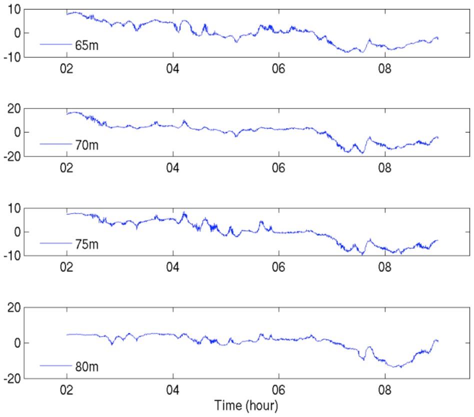
10
0
-10
65m
20
-20
70m
75m
80m
02
04
06
08
Time (hour)

4. WAVE D

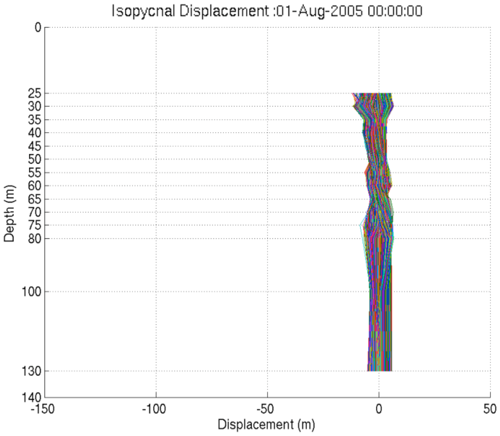
Isopycnal Displacement :01-Aug-2005 00:00:00
Depth (m)
0
25
30
35
40
45
50
55
60
65
70
75
80
100
130
140
-150
-100
-50
0
50
Displacement (m)

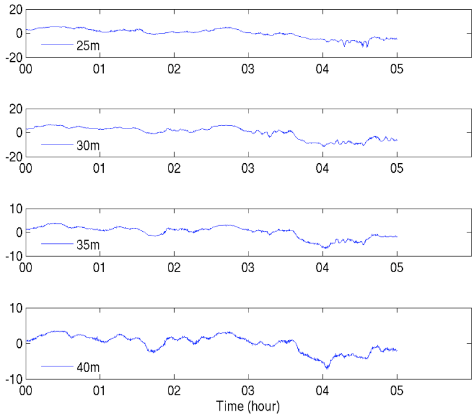
20
0
-20
25m
20
0
-20
30m
10
0
-10
35m
10
0
-10
40m
00
01
02
03
04
05
Time (hour)

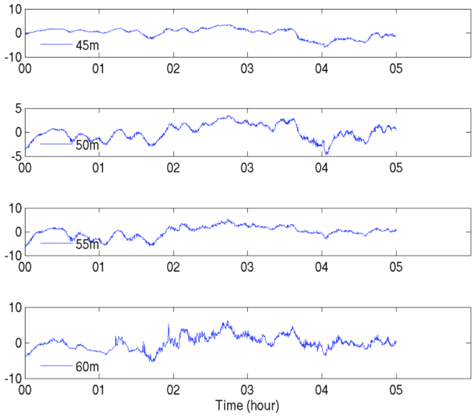
10
0
-10
45m
5
0
-5
50m
10
0
-10
55m
10
0
-10
60m
00
01
02
03
04
05
Time (hour)

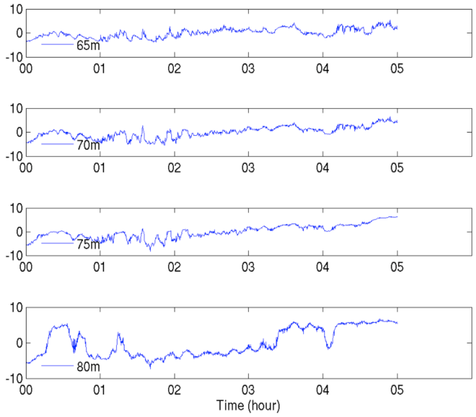
10
0
-10
65m
10
0
-10
70m
10
0
-10
75m
10
0
-10
80m
00
01
02
03
04
05
Time (hour)

APPENDIX B. ENERGY SPECTRUM – TEMPERATURE

1. WAVE A

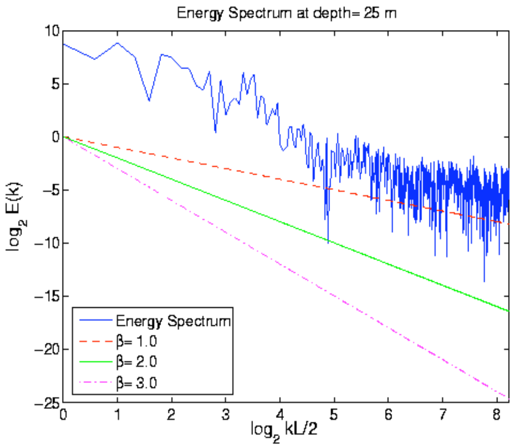

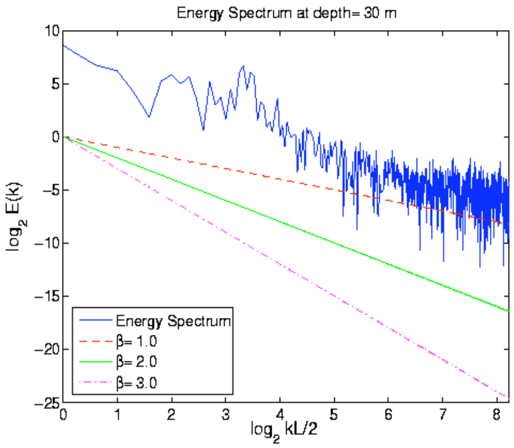

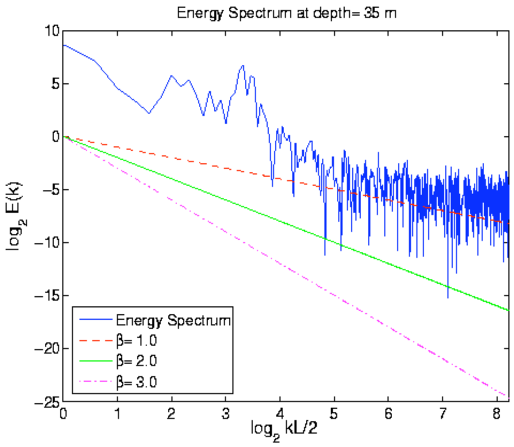

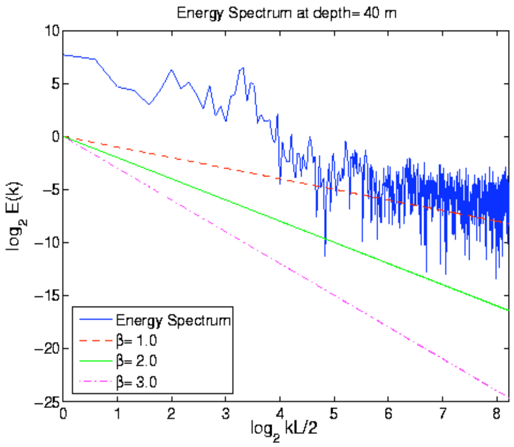

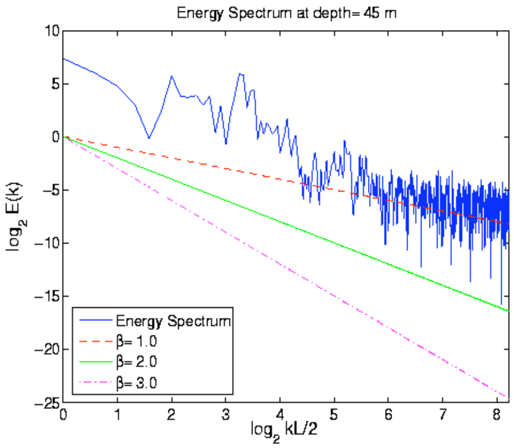

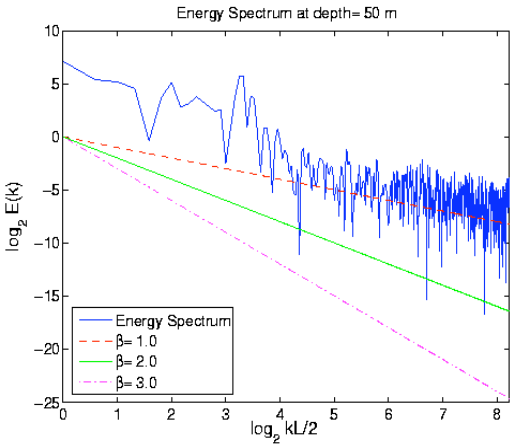

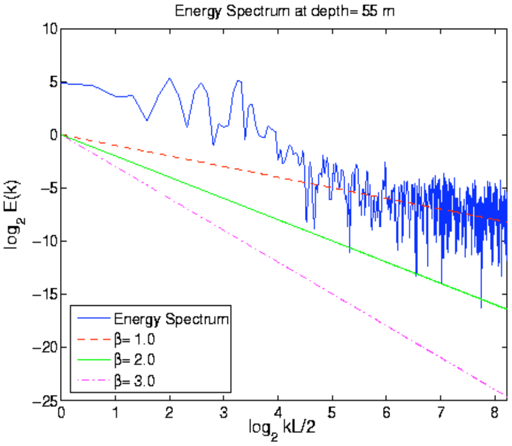
Energy Spectrum at depth= 55 m
log$_2$ E(k)
log$_2$ kL/2
10
5
0
−5
−10
−15
−20
−25
0 1 2 3 4 5 6 7 8
Energy Spectrum
β= 1.0
β= 2.0
β= 3.0

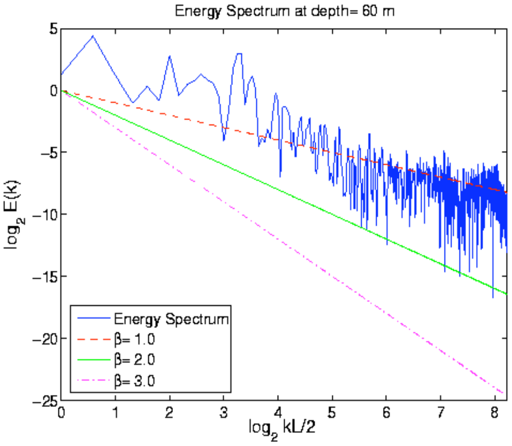
Energy Spectrum at depth= 60 m
log$_2$ E(k)
log$_2$ kL/2
5
0
−5
−10
−15
−20
−25
0 1 2 3 4 5 6 7 8
Energy Spectrum
β= 1.0
β= 2.0
β= 3.0

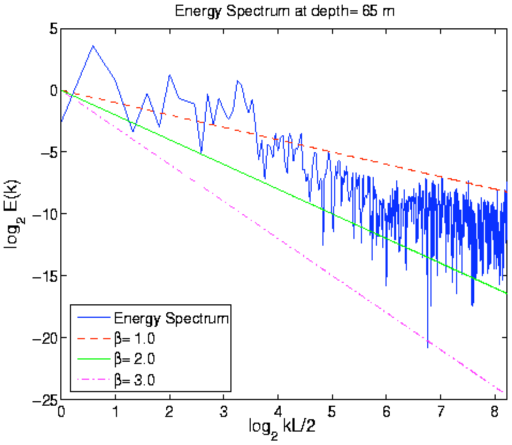
Energy Spectrum at depth= 65 m
log$_2$ E(k)
log$_2$ kL/2
5
0
−5
−10
−15
−20
−25
0 1 2 3 4 5 6 7 8
Energy Spectrum
β= 1.0
β= 2.0
β= 3.0

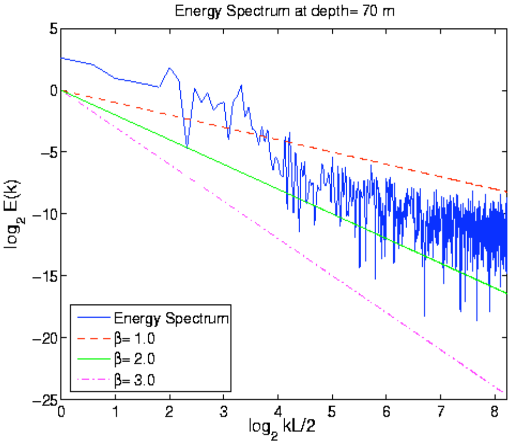
Energy Spectrum at depth= 70 m
log$_2$ E(k)
log$_2$ kL/2
5
0
−5
−10
−15
−20
−25
0 1 2 3 4 5 6 7 8
Energy Spectrum
β= 1.0
β= 2.0
β= 3.0

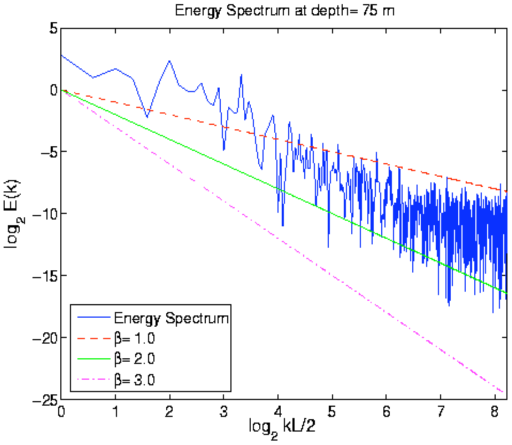
Energy Spectrum at depth= 75 m
log$_2$ E(k)
log$_2$ kL/2
5
0
−5
−10
−15
−20
−25
0 1 2 3 4 5 6 7 8
Energy Spectrum
β= 1.0
β= 2.0
β= 3.0

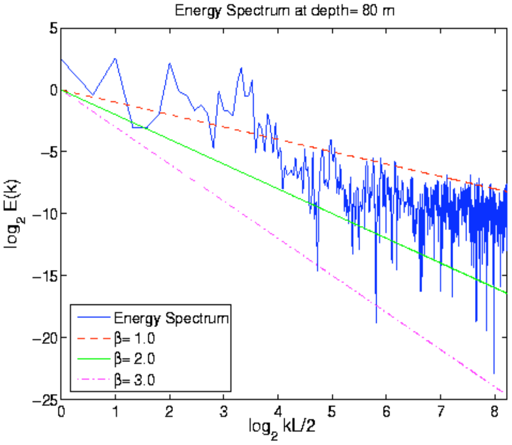
Energy Spectrum at depth= 80 m
log$_2$ E(k)
log$_2$ kL/2
5
0
−5
−10
−15
−20
−25
0 1 2 3 4 5 6 7 8
Energy Spectrum
β= 1.0
β= 2.0
β= 3.0

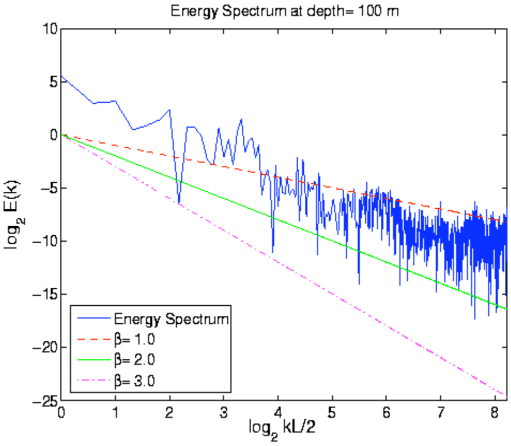
Energy Spectrum at depth= 100 m
log$_2$ E(k)
log$_2$ kL/2
10
5
0
−5
−10
−15
−20
−25
0
1
2
3
4
5
6
7
8
Energy Spectrum
β= 1.0
β= 2.0
β= 3.0

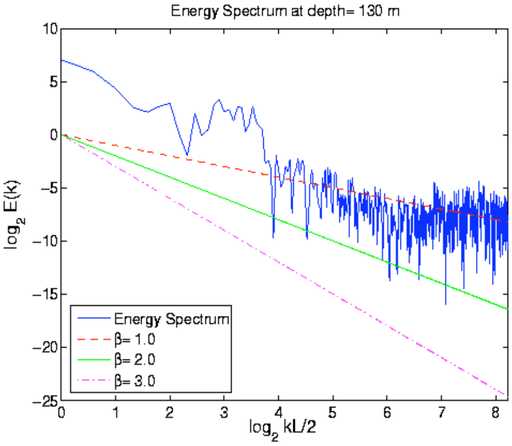
Energy Spectrum at depth= 130 m
log$_2$ E(k)
log$_2$ kL/2
10
5
0
−5
−10
−15
−20
−25
0
1
2
3
4
5
6
7
8
Energy Spectrum
β= 1.0
β= 2.0
β= 3.0

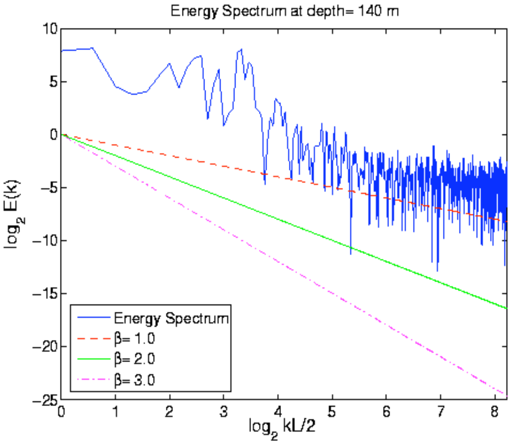
Energy Spectrum at depth= 140 m
log$_2$ E(k)
log$_2$ kL/2
10
5
0
−5
−10
−15
−20
−25
0
1
2
3
4
5
6
7
8
Energy Spectrum
β= 1.0
β= 2.0
β= 3.0

2. WAVE B

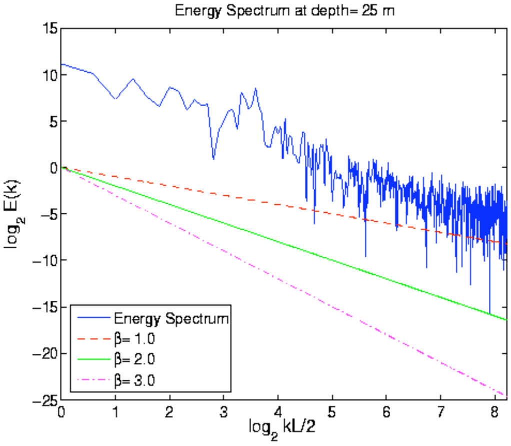
Energy Spectrum at depth= 25 m
15
10
5
0
−5
−10
−15
−20
−25
0
1
2
3
4
5
6
7
8
$\log_2 E(k)$
$\log_2 kL/2$
Energy Spectrum
β= 1.0
β= 2.0
β= 3.0

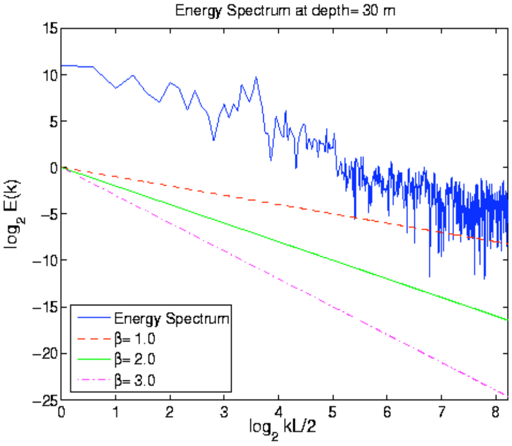
Energy Spectrum at depth= 30 m
15
10
5
0
−5
−10
−15
−20
−25
0
1
2
3
4
5
6
7
8
$\log_2 E(k)$
$\log_2 kL/2$
Energy Spectrum
β= 1.0
β= 2.0
β= 3.0

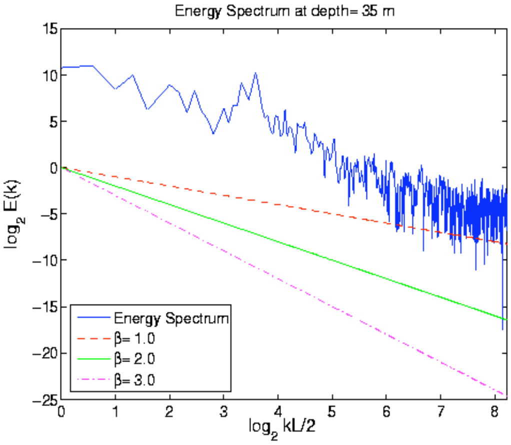
Energy Spectrum at depth= 35 m
15
10
5
0
−5
−10
−15
−20
−25
0
1
2
3
4
5
6
7
8
$\log_2 E(k)$
$\log_2 kL/2$
Energy Spectrum
β= 1.0
β= 2.0
β= 3.0

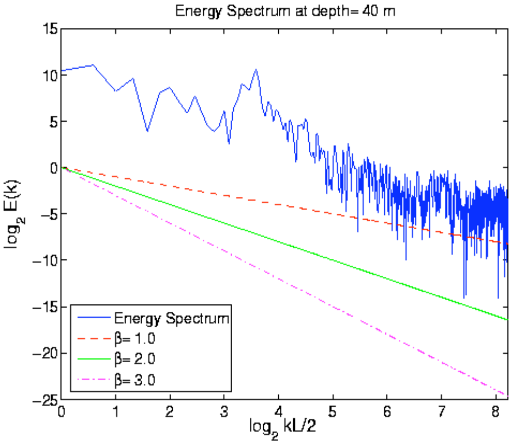
Energy Spectrum at depth= 40 m
15
10
5
0
−5
−10
−15
−20
−25
0
1
2
3
4
5
6
7
8
$\log_2 E(k)$
$\log_2 kL/2$
Energy Spectrum
β= 1.0
β= 2.0
β= 3.0

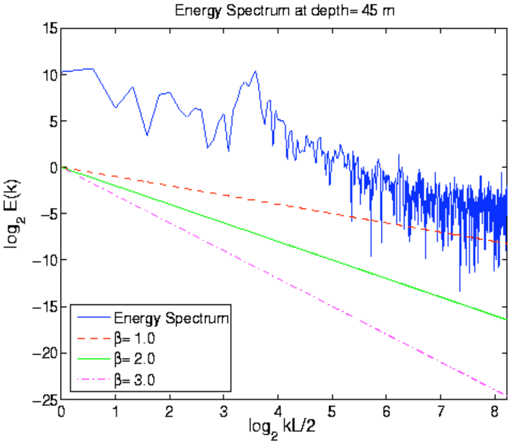
Energy Spectrum at depth= 45 m
15
10
5
0
−5
−10
−15
−20
−25
0
1
2
3
4
5
6
7
8
$\log_2 E(k)$
$\log_2 kL/2$
Energy Spectrum
β= 1.0
β= 2.0
β= 3.0

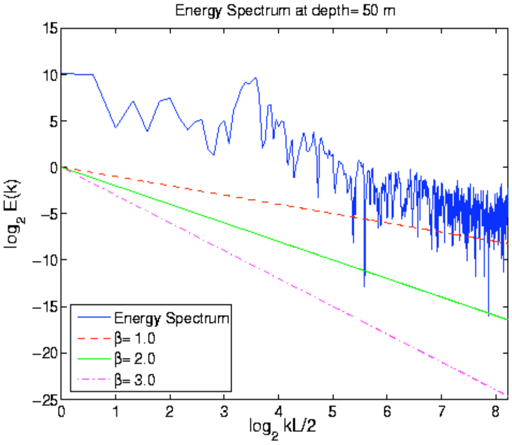
Energy Spectrum at depth= 50 m
15
10
5
0
−5
−10
−15
−20
−25
0
1
2
3
4
5
6
7
8
$\log_2 E(k)$
$\log_2 kL/2$
Energy Spectrum
β= 1.0
β= 2.0
β= 3.0

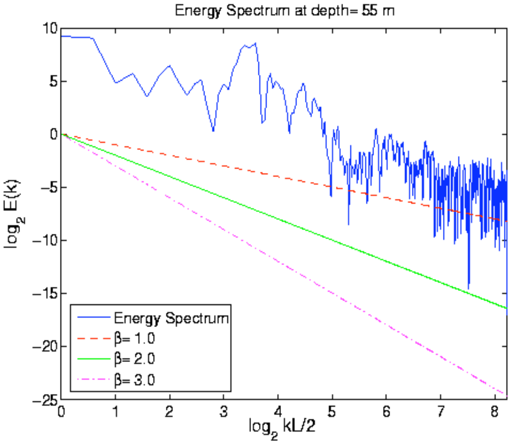
Energy Spectrum at depth= 55 m

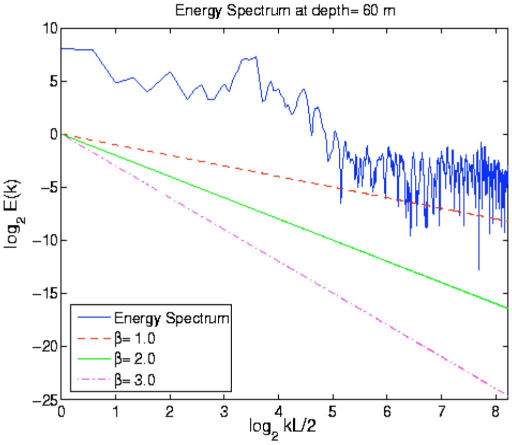
Energy Spectrum at depth= 60 m

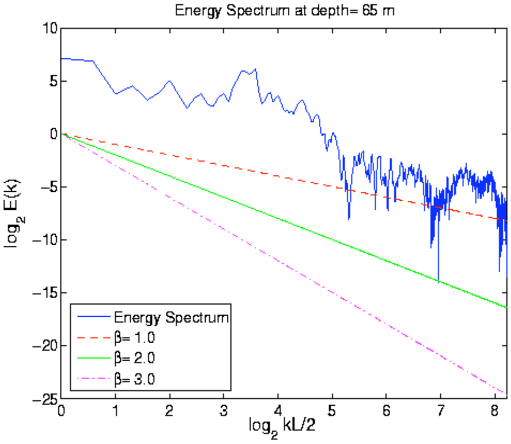
Energy Spectrum at depth= 65 m

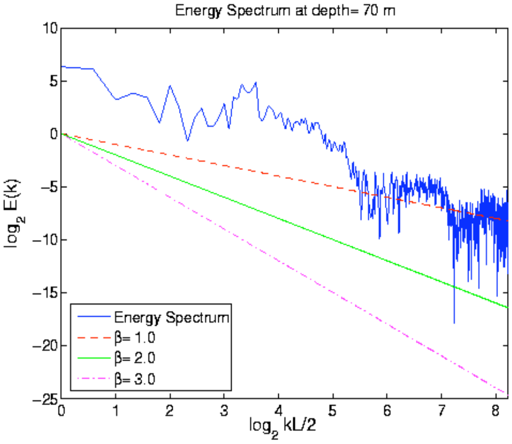
Energy Spectrum at depth= 70 m

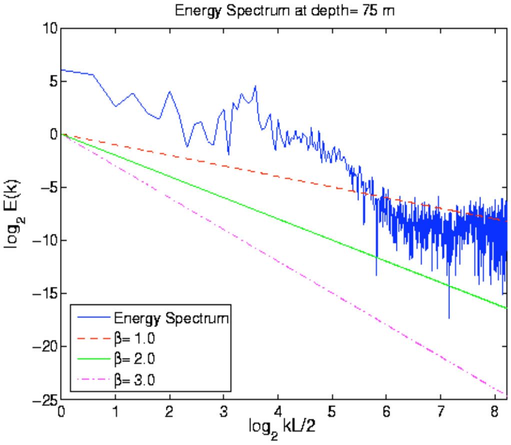
Energy Spectrum at depth= 75 m

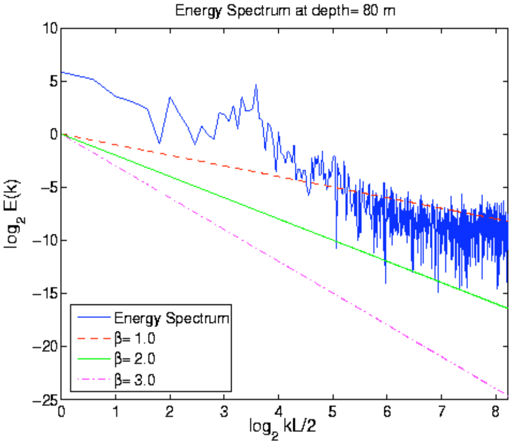
Energy Spectrum at depth= 80 m

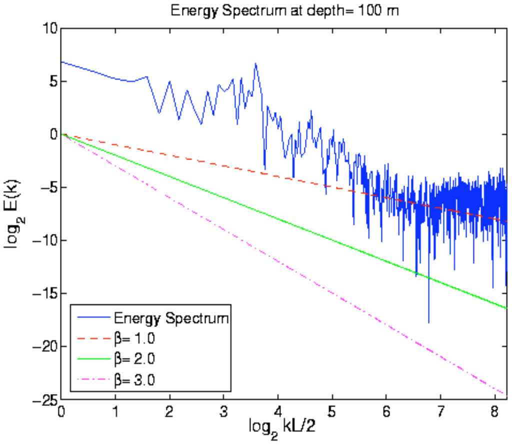
Energy Spectrum at depth= 100 m
log$_2$ E(k)
log$_2$ kL/2
10
5
0
−5
−10
−15
−20
−25
0
1
2
3
4
5
6
7
8
Energy Spectrum
β= 1.0
β= 2.0
β= 3.0

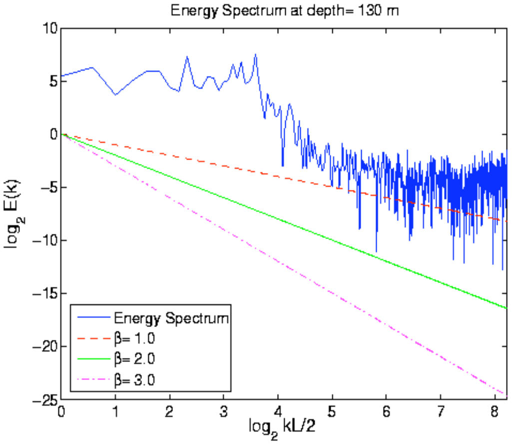
Energy Spectrum at depth= 130 m
log$_2$ E(k)
log$_2$ kL/2
10
5
0
−5
−10
−15
−20
−25
0
1
2
3
4
5
6
7
8
Energy Spectrum
β= 1.0
β= 2.0
β= 3.0

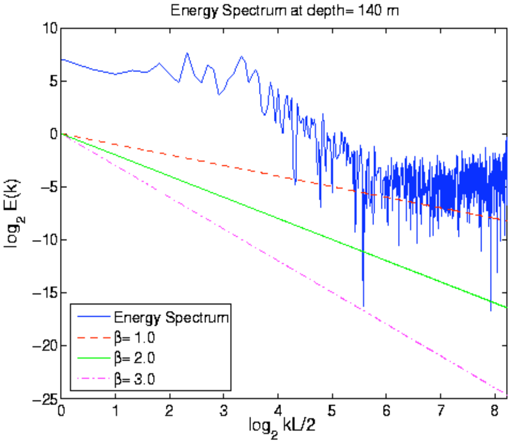
Energy Spectrum at depth= 140 m
log$_2$ E(k)
log$_2$ kL/2
10
5
0
−5
−10
−15
−20
−25
0
1
2
3
4
5
6
7
8
Energy Spectrum
β= 1.0
β= 2.0
β= 3.0

3. WAVE C

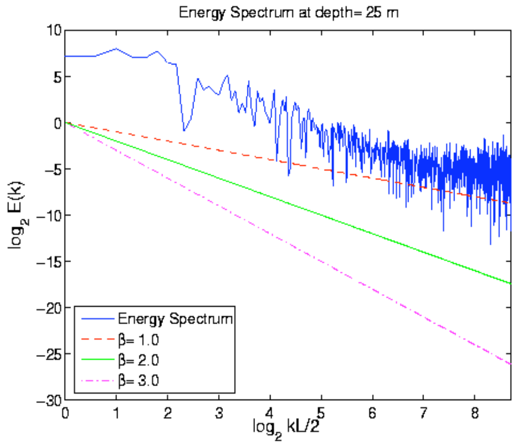
Energy Spectrum at depth= 25 m

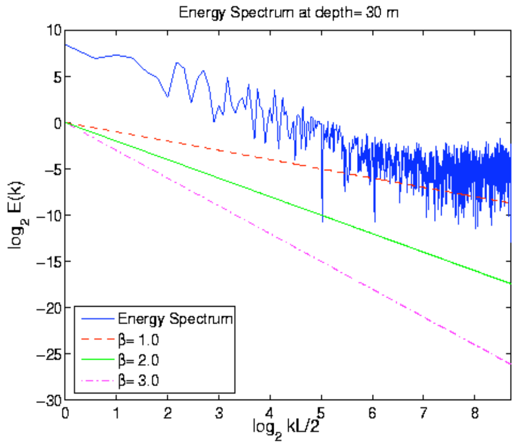
Energy Spectrum at depth= 30 m

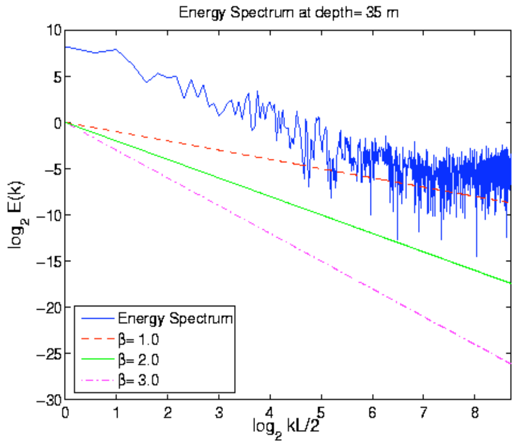
Energy Spectrum at depth= 35 m

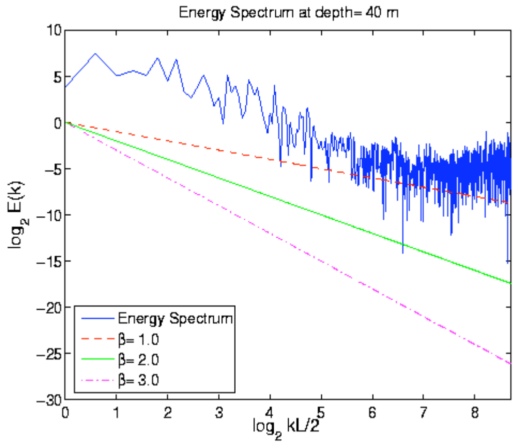
Energy Spectrum at depth= 40 m

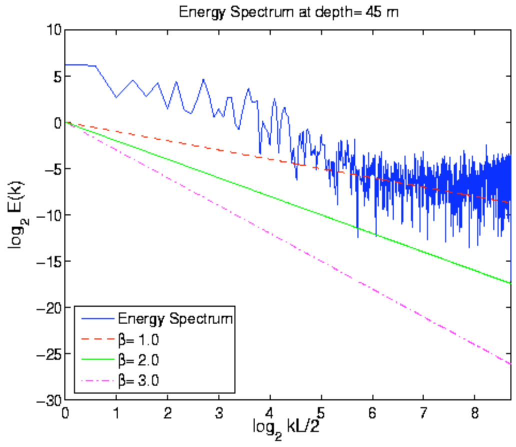
Energy Spectrum at depth= 45 m

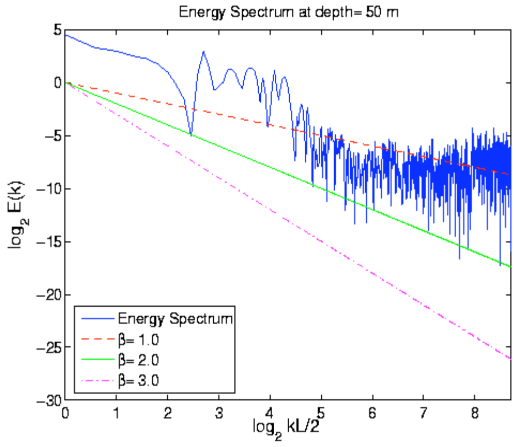
Energy Spectrum at depth= 50 m

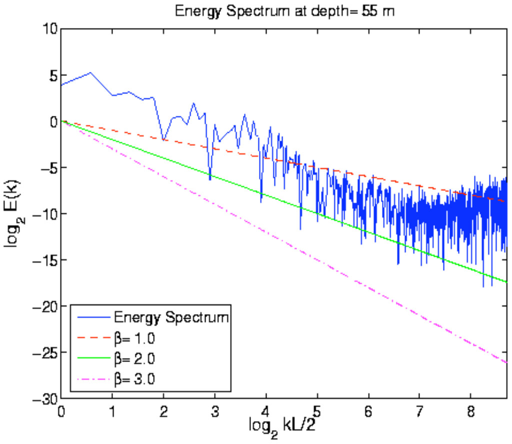
Energy Spectrum at depth= 55 m
log2 E(k)
log2 kL/2
10
5
0
−5
−10
−15
−20
−25
−30
0
1
2
3
4
5
6
7
8
Energy Spectrum
β= 1.0
β= 2.0
β= 3.0

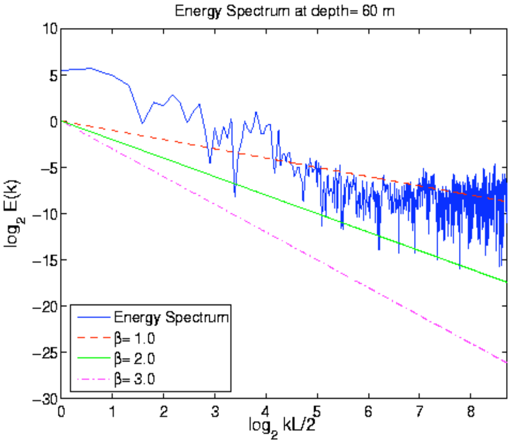
Energy Spectrum at depth= 60 m
log2 E(k)
log2 kL/2
10
5
0
−5
−10
−15
−20
−25
−30
0
1
2
3
4
5
6
7
8
Energy Spectrum
β= 1.0
β= 2.0
β= 3.0

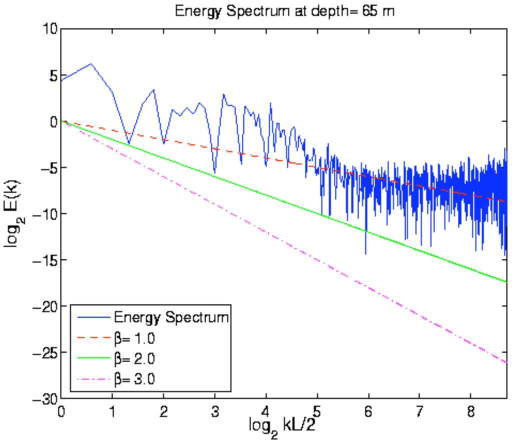
Energy Spectrum at depth= 65 m
log2 E(k)
log2 kL/2
10
5
0
−5
−10
−15
−20
−25
−30
0
1
2
3
4
5
6
7
8
Energy Spectrum
β= 1.0
β= 2.0
β= 3.0

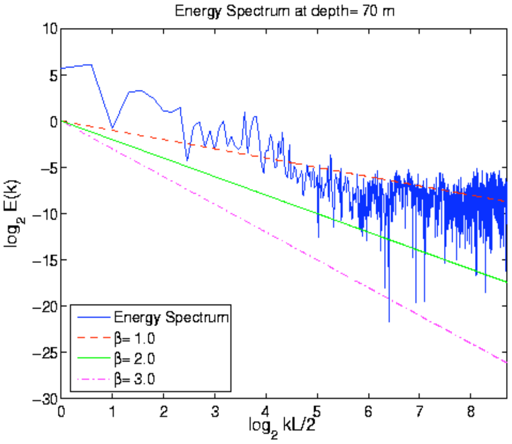
Energy Spectrum at depth= 70 m
log2 E(k)
log2 kL/2
10
5
0
−5
−10
−15
−20
−25
−30
0
1
2
3
4
5
6
7
8
Energy Spectrum
β= 1.0
β= 2.0
β= 3.0

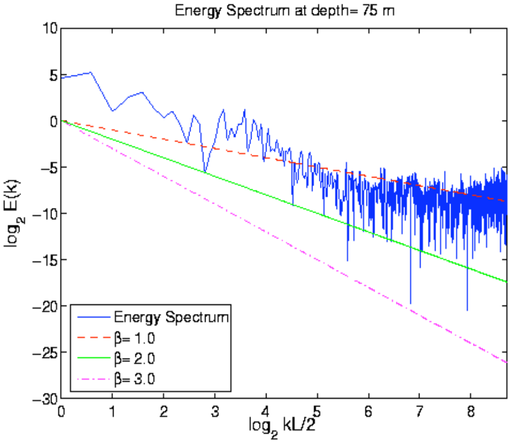
Energy Spectrum at depth= 75 m
log2 E(k)
log2 kL/2
10
5
0
−5
−10
−15
−20
−25
−30
0
1
2
3
4
5
6
7
8
Energy Spectrum
β= 1.0
β= 2.0
β= 3.0

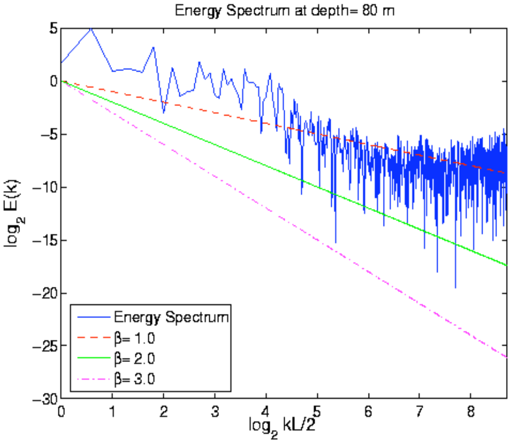
Energy Spectrum at depth= 80 m
log2 E(k)
log2 kL/2
5
0
−5
−10
−15
−20
−25
−30
0
1
2
3
4
5
6
7
8
Energy Spectrum
β= 1.0
β= 2.0
β= 3.0

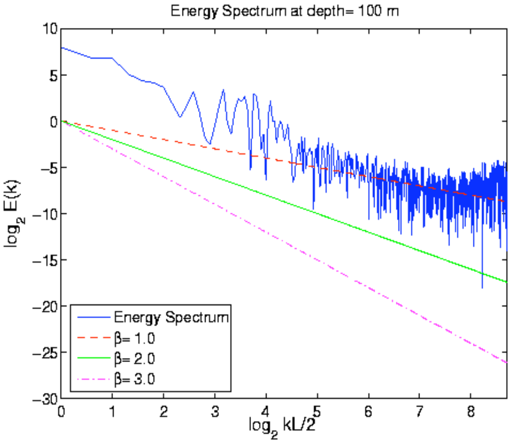
Energy Spectrum at depth= 100 m

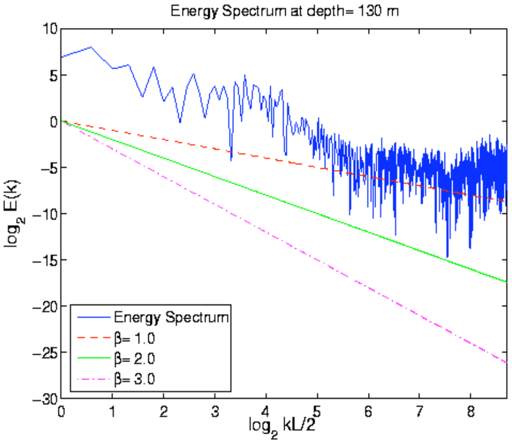
Energy Spectrum at depth= 130 m

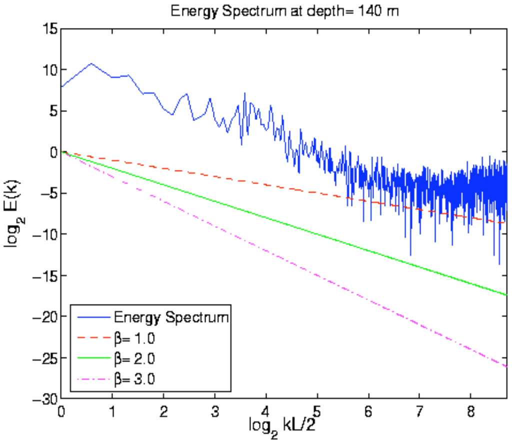
Energy Spectrum at depth= 140 m

4. WAVE D

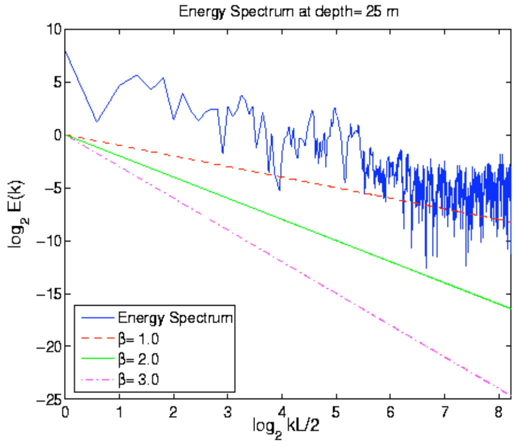
Energy Spectrum at depth= 25 m

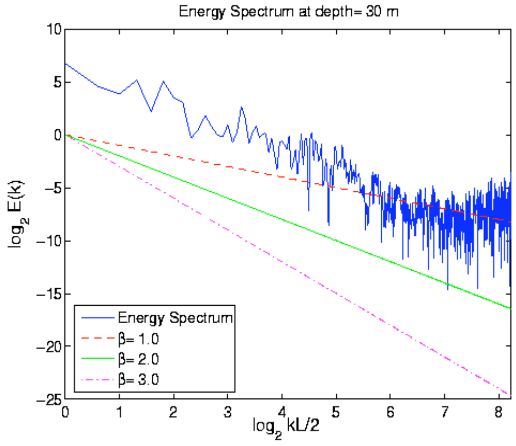
Energy Spectrum at depth= 30 m

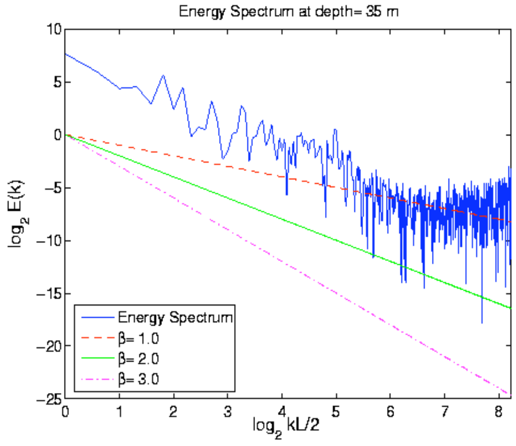
Energy Spectrum at depth= 35 m

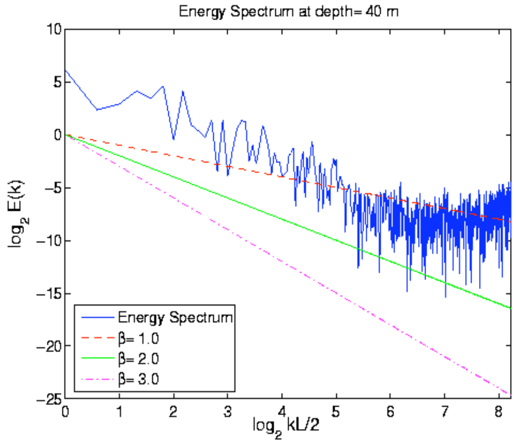
Energy Spectrum at depth= 40 m

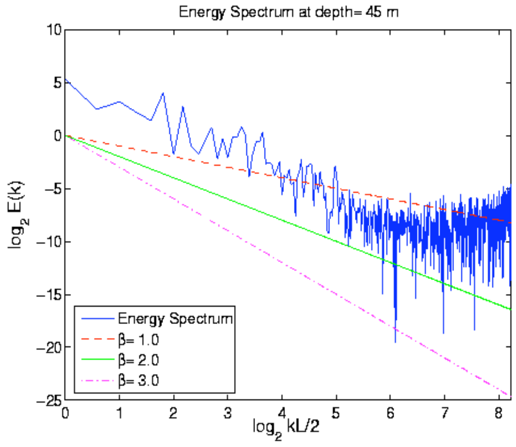
Energy Spectrum at depth= 45 m

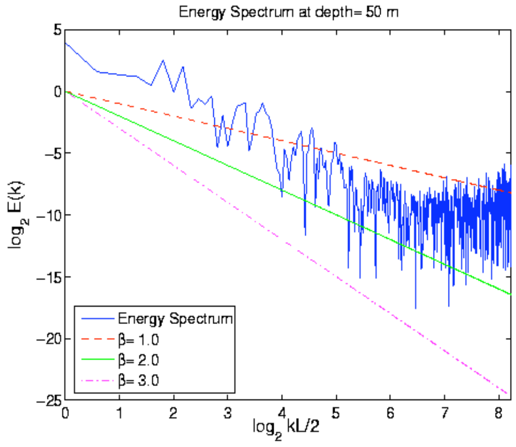
Energy Spectrum at depth= 50 m

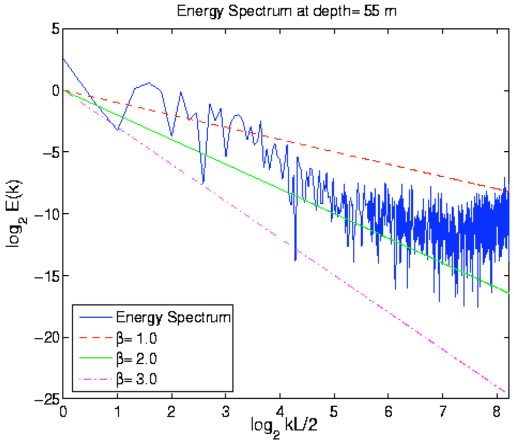
Energy Spectrum at depth= 55 m
log$_2$ E(k)
log$_2$ kL/2
5
0
−5
−10
−15
−20
−25
0
1
2
3
4
5
6
7
8
Energy Spectrum
β= 1.0
β= 2.0
β= 3.0

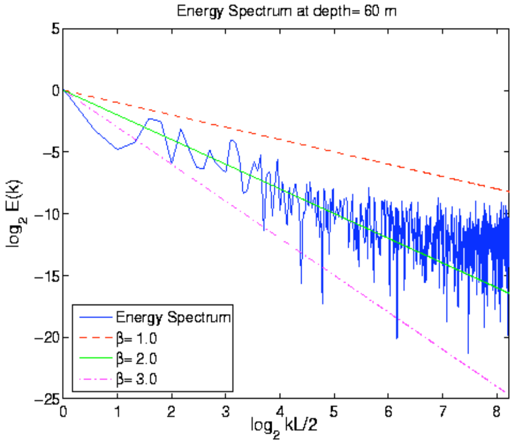
Energy Spectrum at depth= 60 m
log$_2$ E(k)
log$_2$ kL/2
5
0
−5
−10
−15
−20
−25
0
1
2
3
4
5
6
7
8
Energy Spectrum
β= 1.0
β= 2.0
β= 3.0

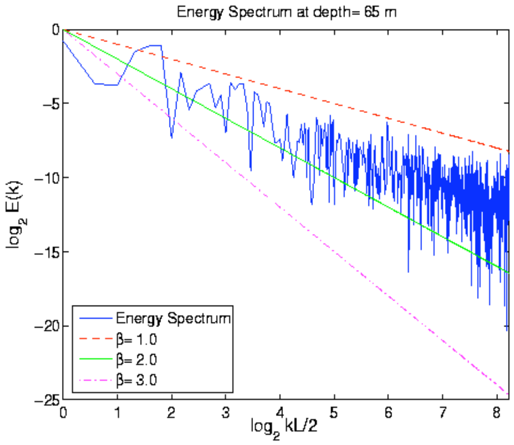
Energy Spectrum at depth= 65 m
log$_2$ E(k)
log$_2$ kL/2
0
−5
−10
−15
−20
−25
0
1
2
3
4
5
6
7
8
Energy Spectrum
β= 1.0
β= 2.0
β= 3.0

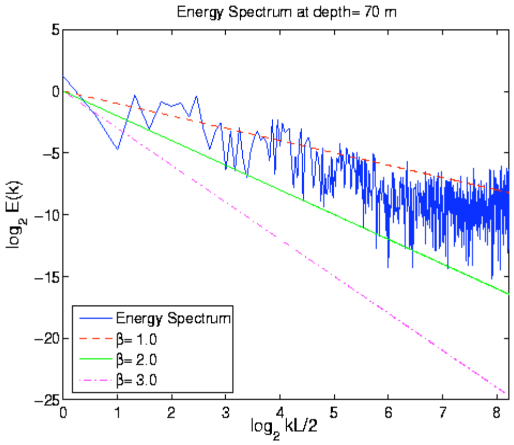
Energy Spectrum at depth= 70 m
log$_2$ E(k)
log$_2$ kL/2
5
0
−5
−10
−15
−20
−25
0
1
2
3
4
5
6
7
8
Energy Spectrum
β= 1.0
β= 2.0
β= 3.0

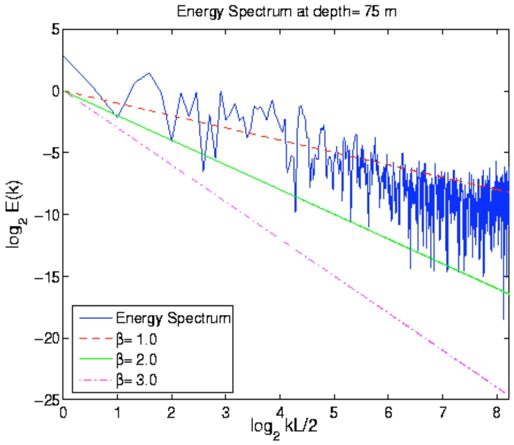
Energy Spectrum at depth= 75 m
log$_2$ E(k)
log$_2$ kL/2
5
0
−5
−10
−15
−20
−25
0
1
2
3
4
5
6
7
8
Energy Spectrum
β= 1.0
β= 2.0
β= 3.0

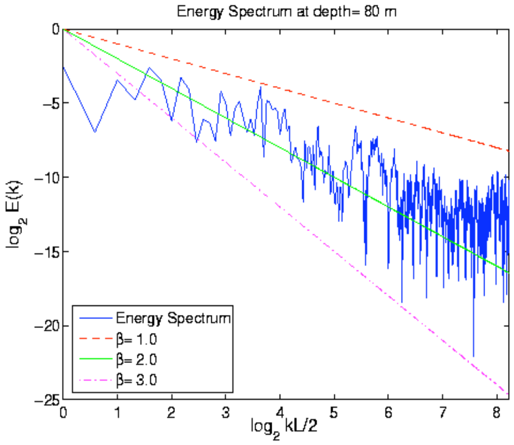
Energy Spectrum at depth= 80 m
log$_2$ E(k)
log$_2$ kL/2
0
−5
−10
−15
−20
−25
0
1
2
3
4
5
6
7
8
Energy Spectrum
β= 1.0
β= 2.0
β= 3.0

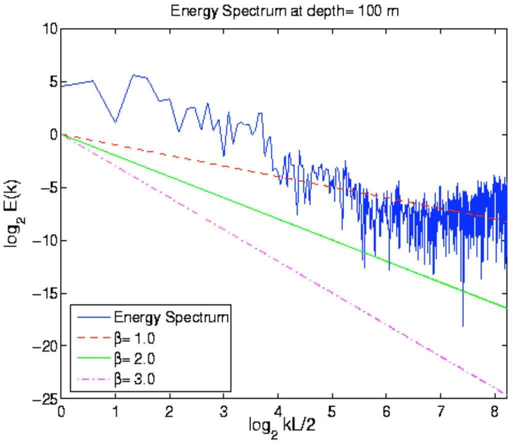
Energy Spectrum at depth= 100 m
10
5
0
−5
−10
−15
−20
−25
$\log_2$ E(k)
0
1
2
3
4
5
6
7
8
$\log_2$ kL/2
Energy Spectrum
β= 1.0
β= 2.0
β= 3.0

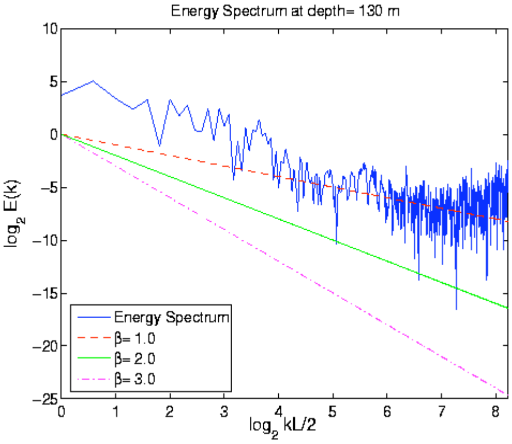
Energy Spectrum at depth= 130 m
10
5
0
−5
−10
−15
−20
−25
$\log_2$ E(k)
0
1
2
3
4
5
6
7
8
$\log_2$ kL/2
Energy Spectrum
β= 1.0
β= 2.0
β= 3.0

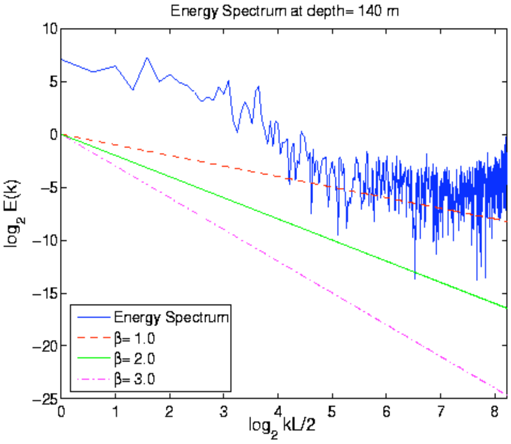
Energy Spectrum at depth= 140 m
10
5
0
−5
−10
−15
−20
−25
$\log_2$ E(k)
0
1
2
3
4
5
6
7
8
$\log_2$ kL/2
Energy Spectrum
β= 1.0
β= 2.0
β= 3.0

APPENDIX C. STRUCTURE FUNCTION –TEMPERATURE

1. WAVE A

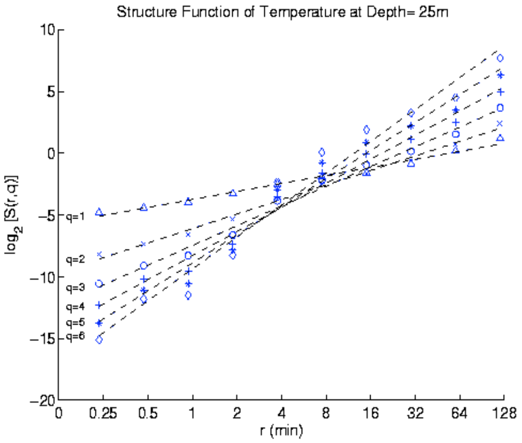

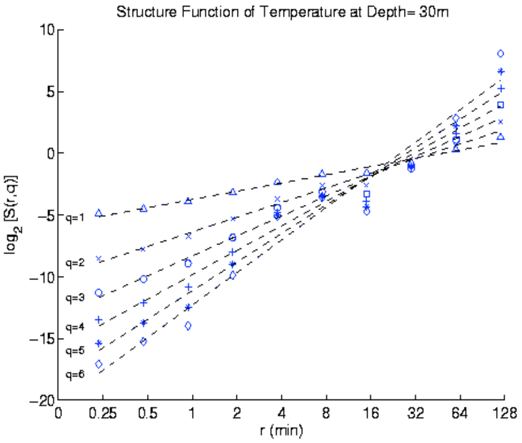

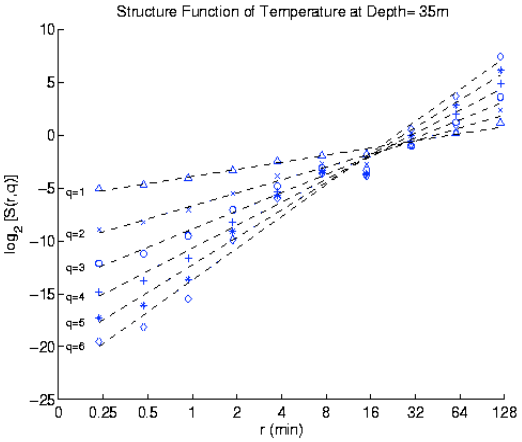

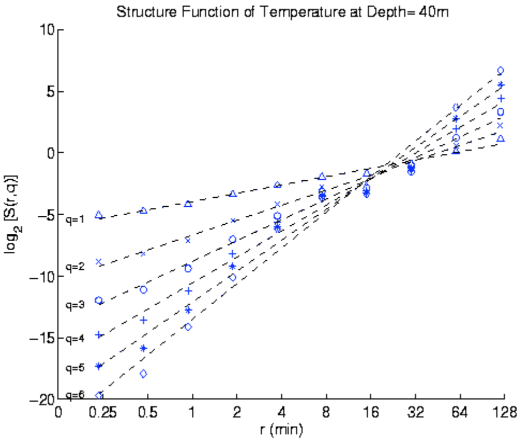

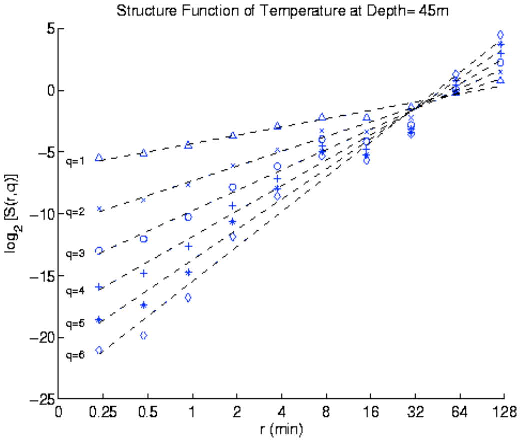

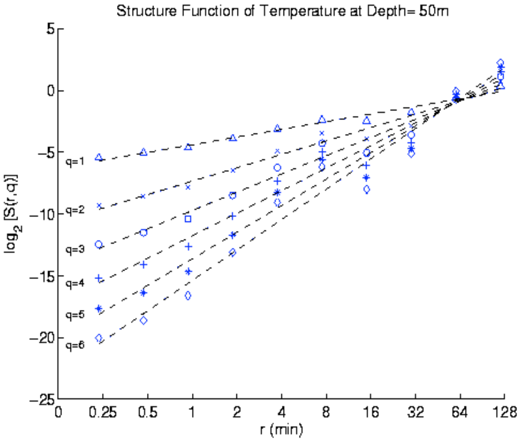

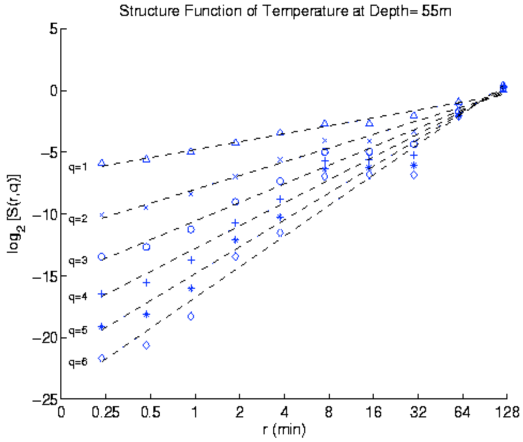
Structure Function of Temperature at Depth= 55m

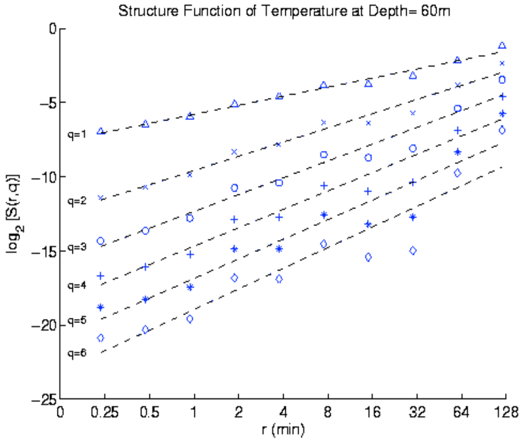
Structure Function of Temperature at Depth= 60m

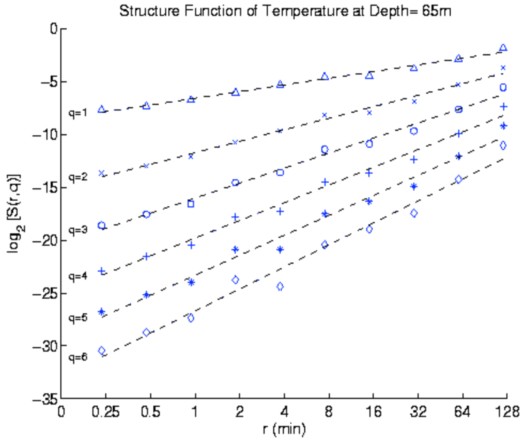
Structure Function of Temperature at Depth= 65m

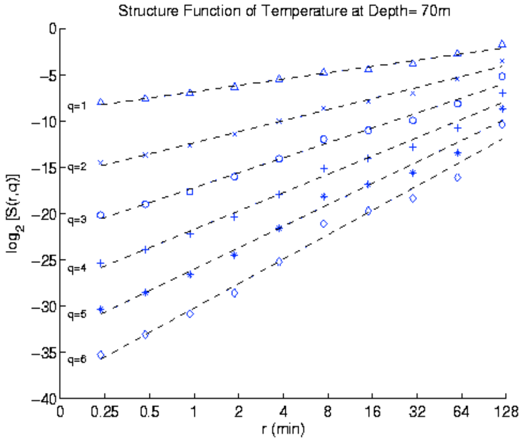
Structure Function of Temperature at Depth= 70m

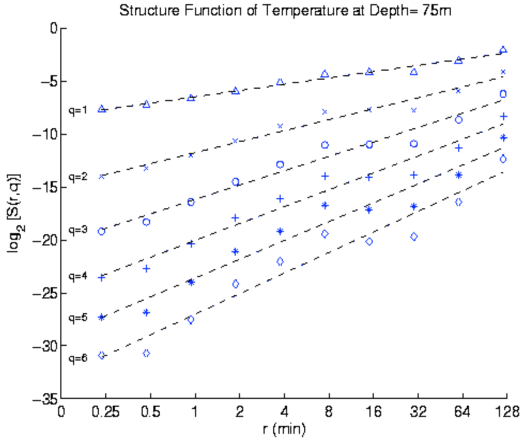
Structure Function of Temperature at Depth= 75m

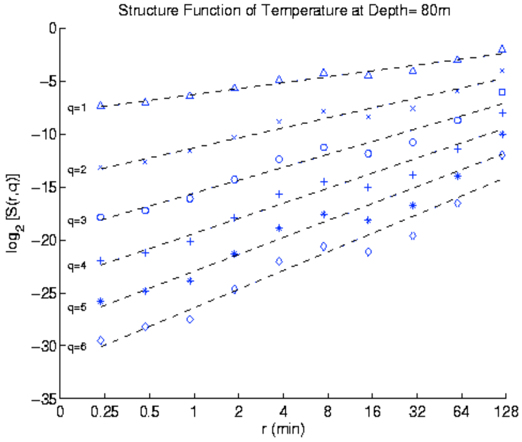
Structure Function of Temperature at Depth= 80m

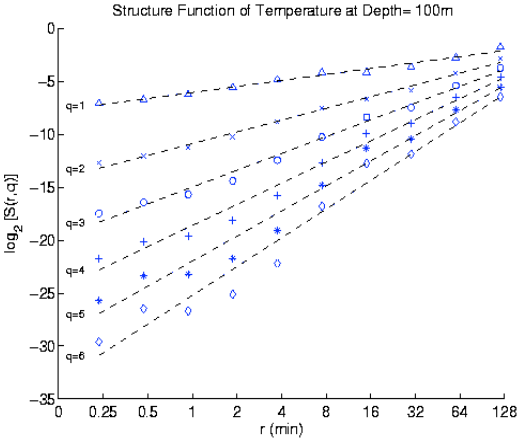
Structure Function of Temperature at Depth= 100m
log$_2$ [S(r,q)]
r (min)
0
-5
-10
-15
-20
-25
-30
-35
0
0.25
0.5
1
2
4
8
16
32
64
128
q=1
q=2
q=3
q=4
q=5
q=6

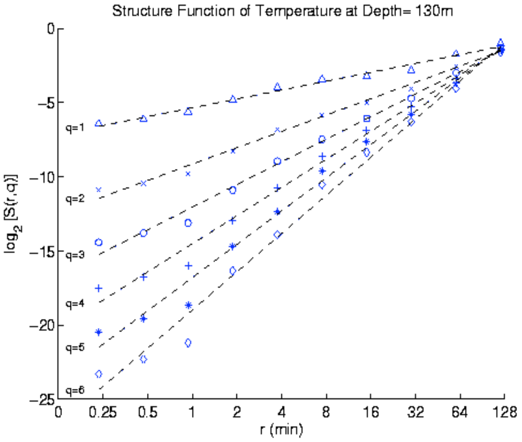
Structure Function of Temperature at Depth= 130m
log$_2$ [S(r,q)]
r (min)
0
-5
-10
-15
-20
-25
0
0.25
0.5
1
2
4
8
16
32
64
128
q=1
q=2
q=3
q=4
q=5
q=6

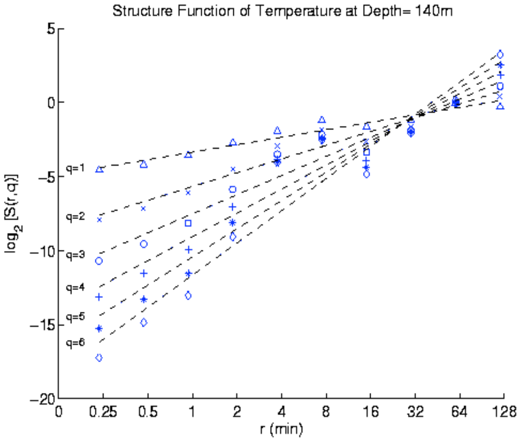
Structure Function of Temperature at Depth= 140m
log$_2$ [S(r,q)]
r (min)
5
0
-5
-10
-15
-20
0
0.25
0.5
1
2
4
8
16
32
64
128
q=1
q=2
q=3
q=4
q=5
q=6

2. WAVE B

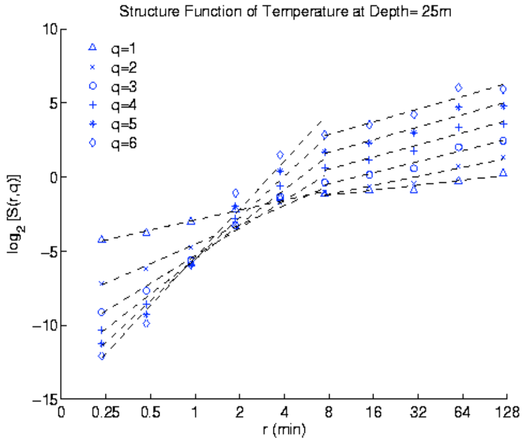
Structure Function of Temperature at Depth= 25m

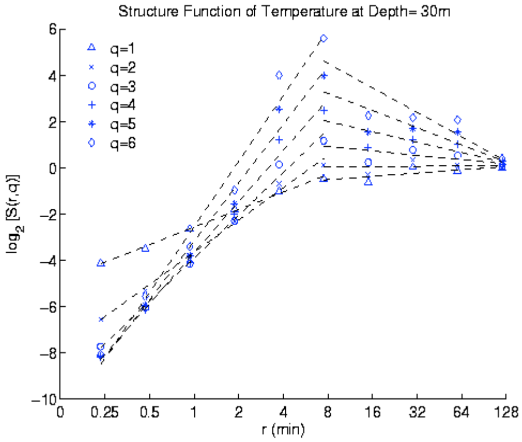
Structure Function of Temperature at Depth= 30m

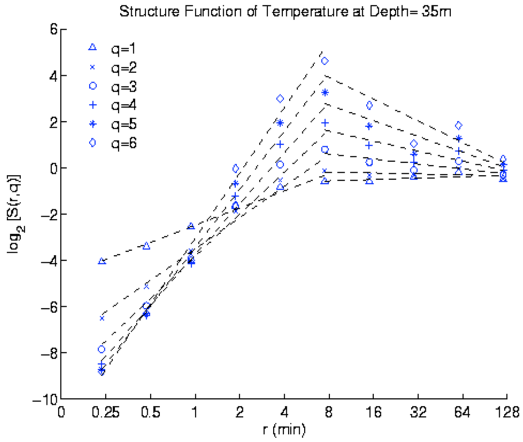
Structure Function of Temperature at Depth= 35m

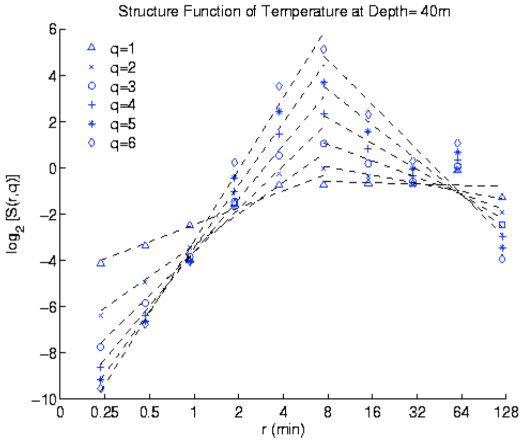
Structure Function of Temperature at Depth= 40m

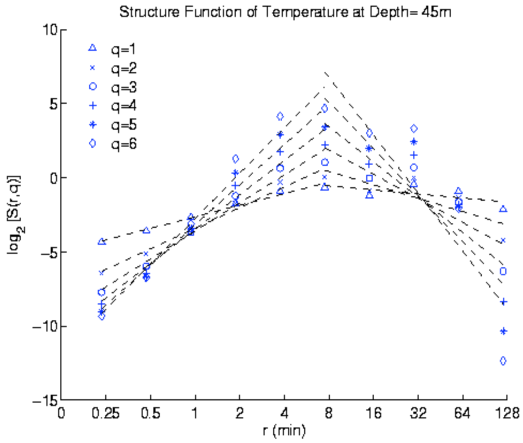
Structure Function of Temperature at Depth= 45m

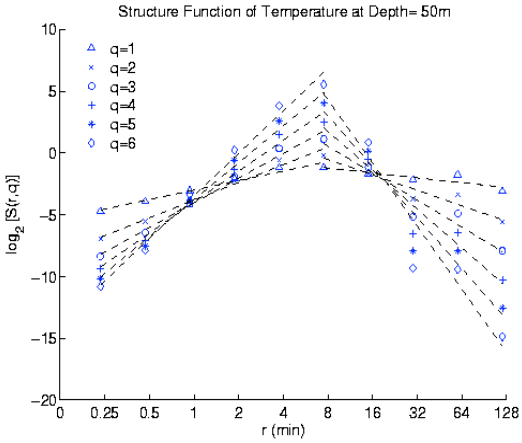
Structure Function of Temperature at Depth= 50m

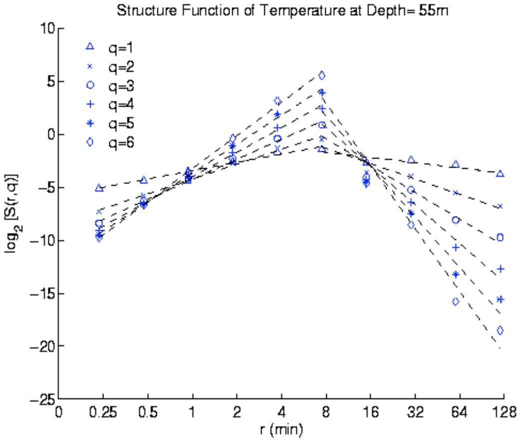
Structure Function of Temperature at Depth= 55m

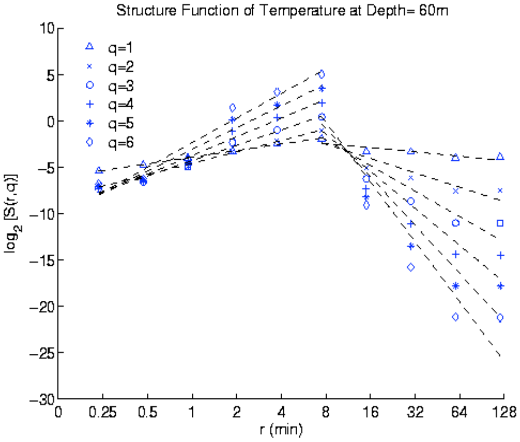
Structure Function of Temperature at Depth= 60m

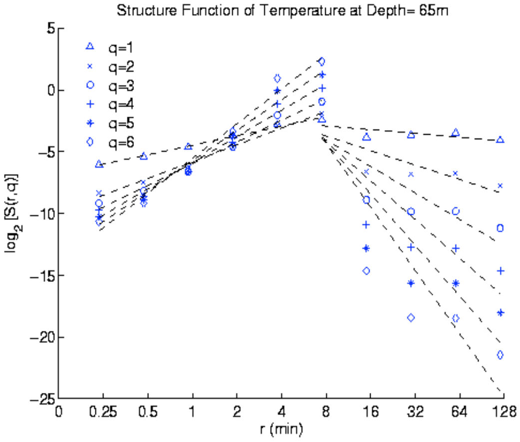
Structure Function of Temperature at Depth= 65m

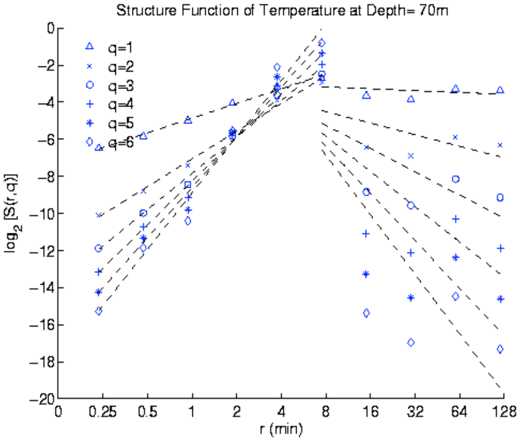
Structure Function of Temperature at Depth= 70m

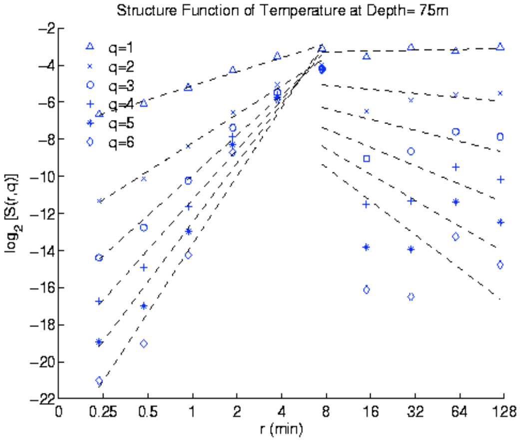
Structure Function of Temperature at Depth= 75m

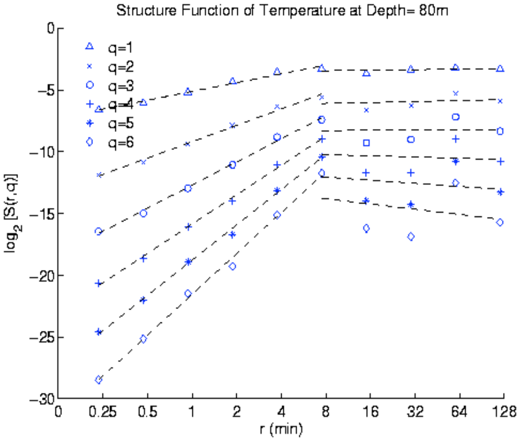
Structure Function of Temperature at Depth= 80m

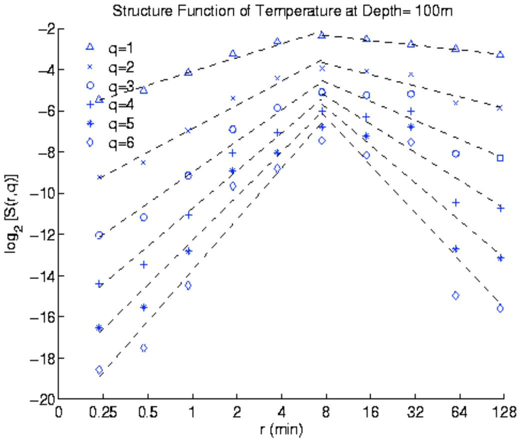
Structure Function of Temperature at Depth= 100m
q=1
q=2
q=3
q=4
q=5
q=6
log2 [S(r,q)]
−2
−4
−6
−8
−10
−12
−14
−16
−18
−20
0
0.25
0.5
1
2
4
8
16
32
64
128
r (min)

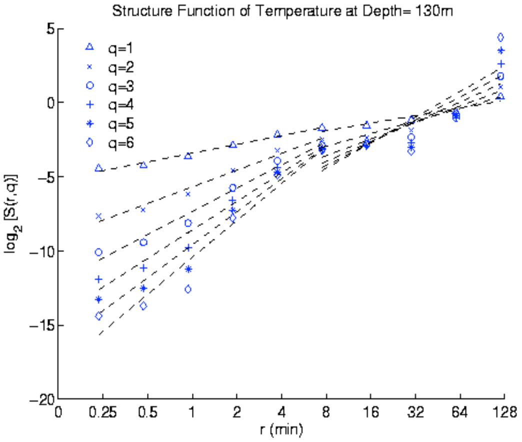
Structure Function of Temperature at Depth= 130m
q=1
q=2
q=3
q=4
q=5
q=6
log2 [S(r,q)]
5
0
−5
−10
−15
−20
0
0.25
0.5
1
2
4
8
16
32
64
128
r (min)

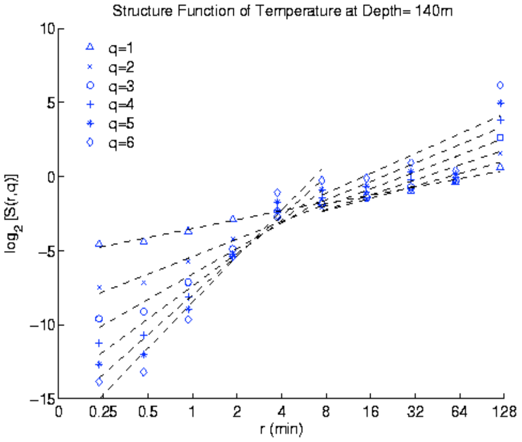
Structure Function of Temperature at Depth= 140m
q=1
q=2
q=3
q=4
q=5
q=6
log2 [S(r,q)]
10
5
0
−5
−10
−15
0
0.25
0.5
1
2
4
8
16
32
64
128
r (min)

3. WAVE C

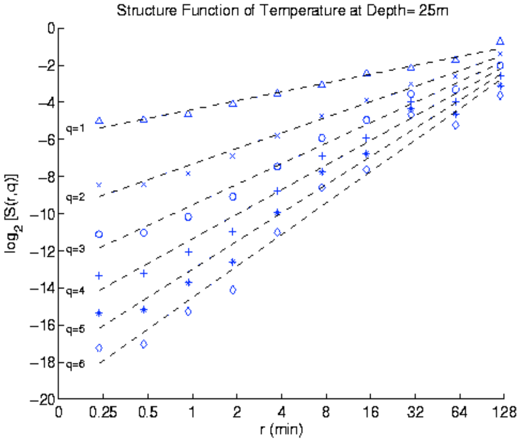
Structure Function of Temperature at Depth= 25m

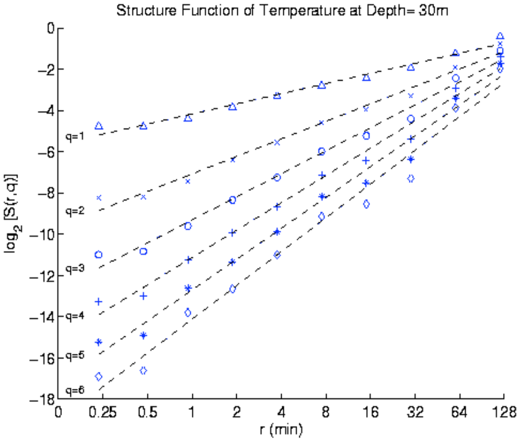
Structure Function of Temperature at Depth= 30m

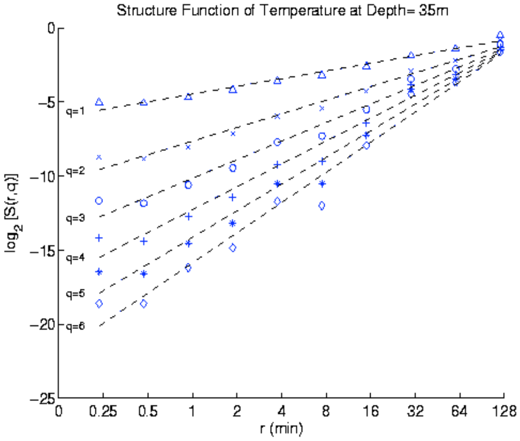
Structure Function of Temperature at Depth= 35m

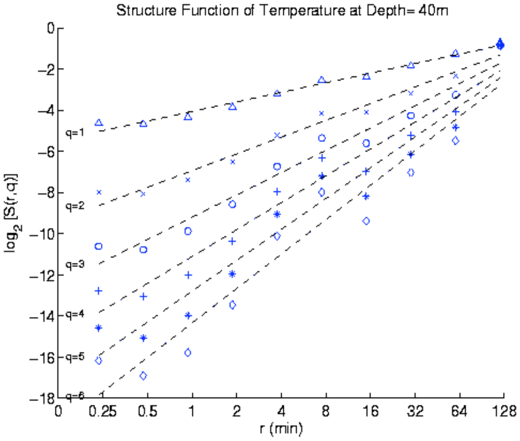
Structure Function of Temperature at Depth= 40m

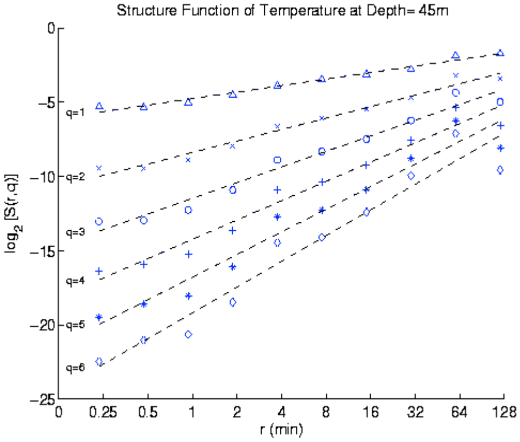
Structure Function of Temperature at Depth= 45m

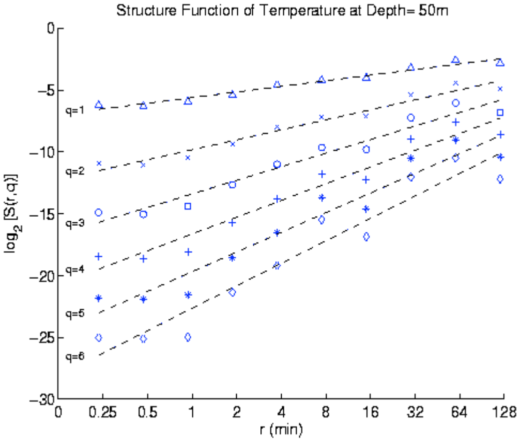
Structure Function of Temperature at Depth= 50m

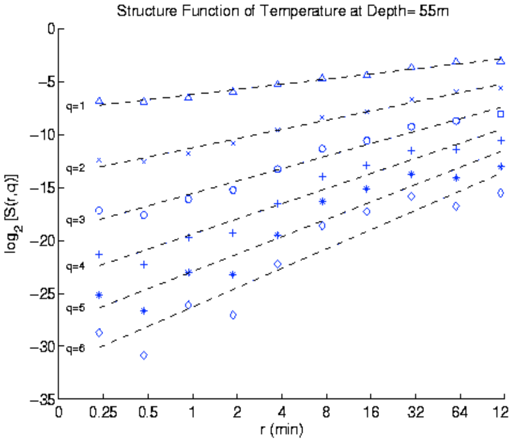
Structure Function of Temperature at Depth= 55m

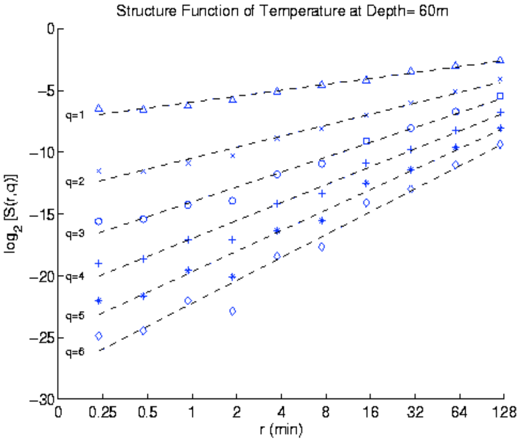
Structure Function of Temperature at Depth= 60m

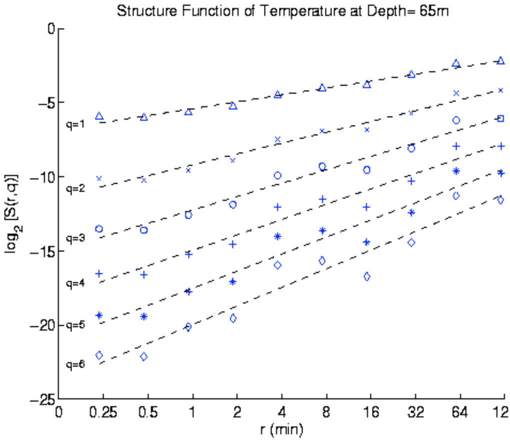
Structure Function of Temperature at Depth= 65m

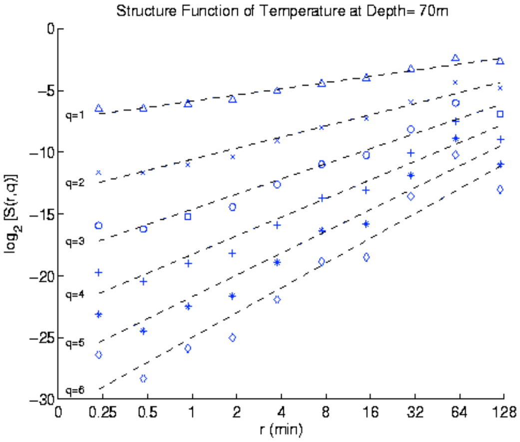
Structure Function of Temperature at Depth= 70m

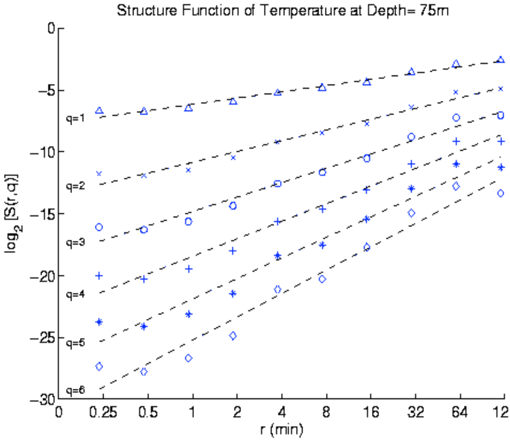
Structure Function of Temperature at Depth= 75m

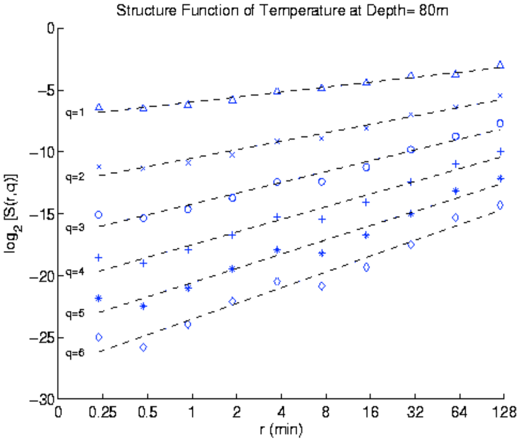
Structure Function of Temperature at Depth= 80m

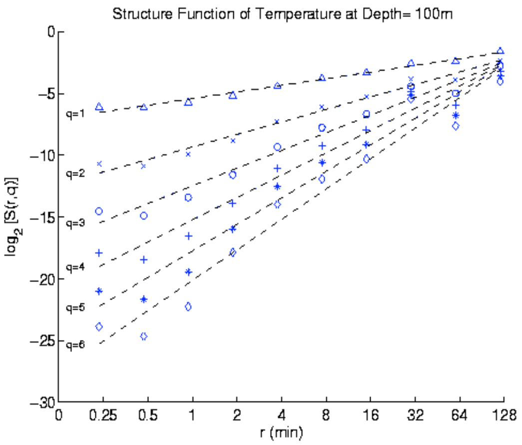

Structure Function of Temperature at Depth= 100m

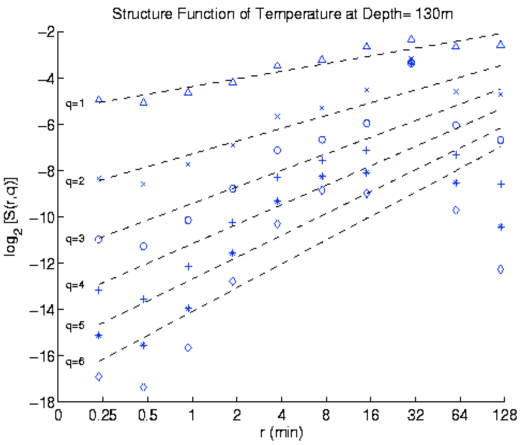

Structure Function of Temperature at Depth= 130m

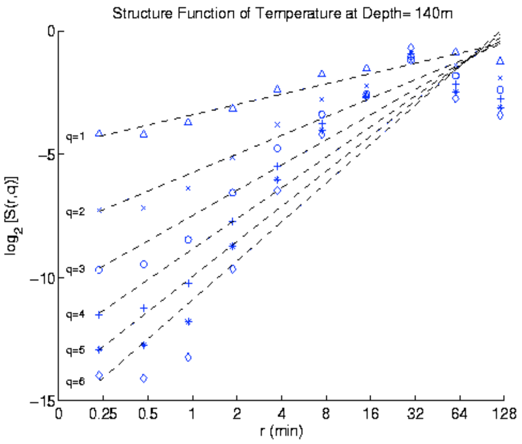

Structure Function of Temperature at Depth= 140m

4. WAVE D

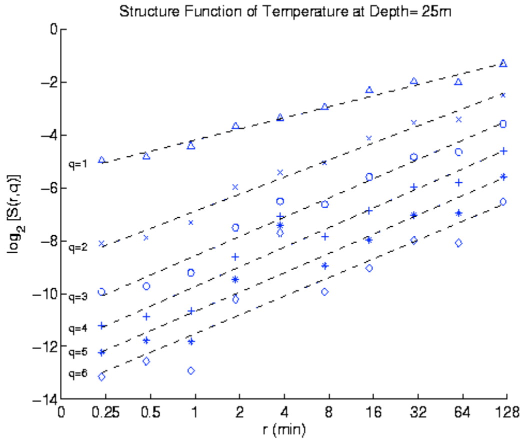
Structure Function of Temperature at Depth= 25m
log2 [S(r,q)]
0
−2
−4
−6
−8
−10
−12
−14
q=1
q=2
q=3
q=4
q=5
q=6
0
0.25
0.5
1
2
4
8
16
32
64
128
r (min)

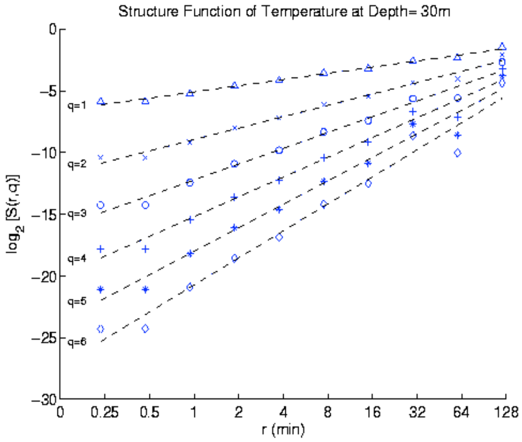
Structure Function of Temperature at Depth= 30m
log2 [S(r,q)]
0
−5
−10
−15
−20
−25
−30
q=1
q=2
q=3
q=4
q=5
q=6
0
0.25
0.5
1
2
4
8
16
32
64
128
r (min)

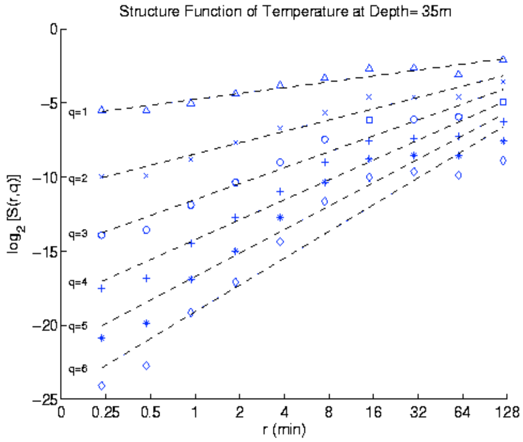
Structure Function of Temperature at Depth= 35m
log2 [S(r,q)]
0
−5
−10
−15
−20
−25
q=1
q=2
q=3
q=4
q=5
q=6
0
0.25
0.5
1
2
4
8
16
32
64
128
r (min)

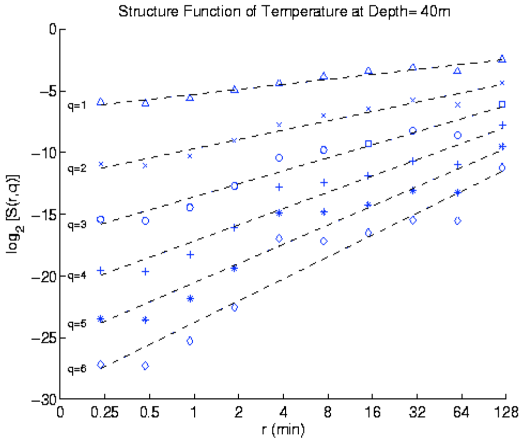
Structure Function of Temperature at Depth= 40m
log2 [S(r,q)]
0
−5
−10
−15
−20
−25
−30
q=1
q=2
q=3
q=4
q=5
q=6
0
0.25
0.5
1
2
4
8
16
32
64
128
r (min)

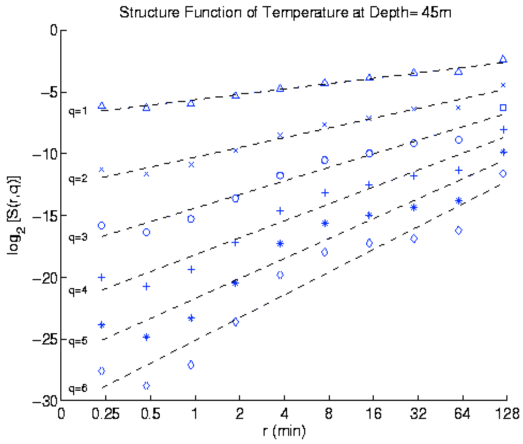
Structure Function of Temperature at Depth= 45m
log2 [S(r,q)]
0
−5
−10
−15
−20
−25
−30
q=1
q=2
q=3
q=4
q=5
q=6
0
0.25
0.5
1
2
4
8
16
32
64
128
r (min)

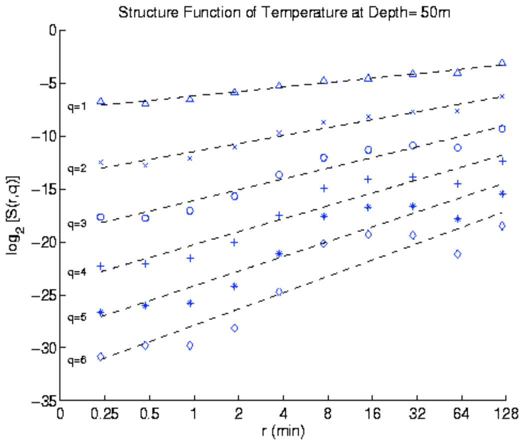
Structure Function of Temperature at Depth= 50m
log2 [S(r,q)]
0
−5
−10
−15
−20
−25
−30
−35
q=1
q=2
q=3
q=4
q=5
q=6
0
0.25
0.5
1
2
4
8
16
32
64
128
r (min)

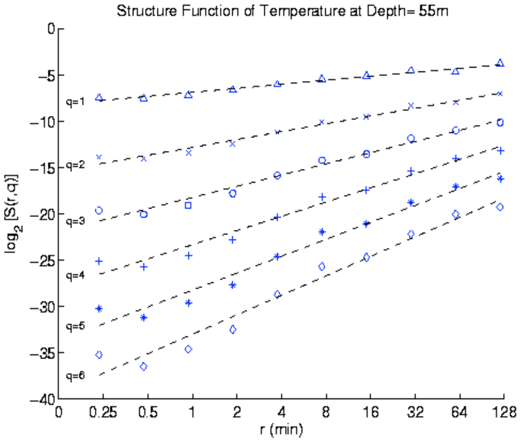
Structure Function of Temperature at Depth= 55m

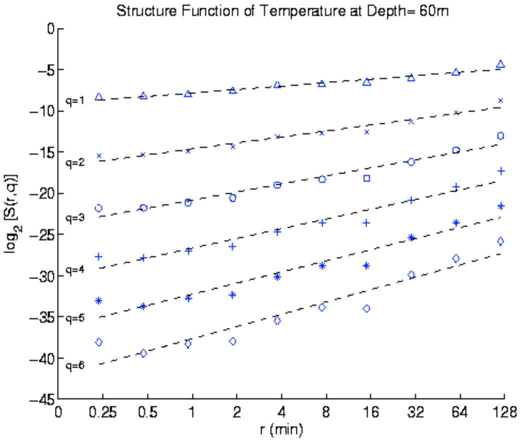
Structure Function of Temperature at Depth= 60m

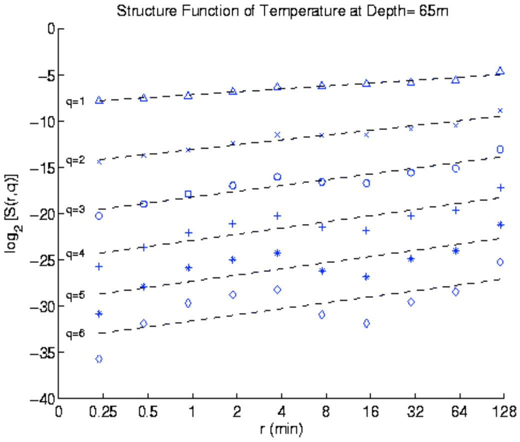
Structure Function of Temperature at Depth= 65m

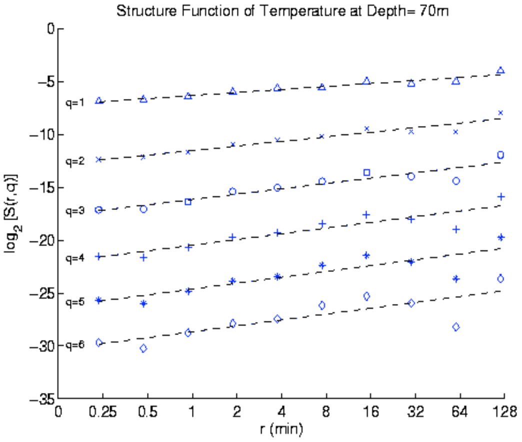
Structure Function of Temperature at Depth= 70m

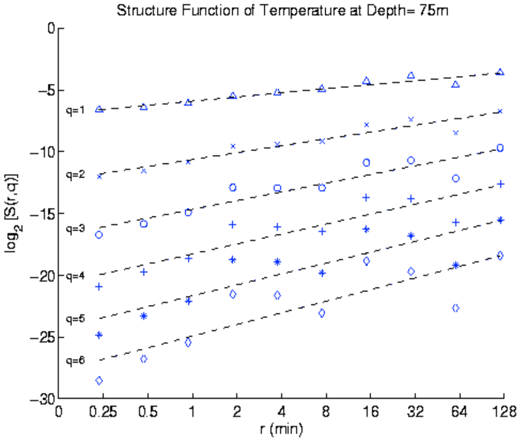
Structure Function of Temperature at Depth= 75m

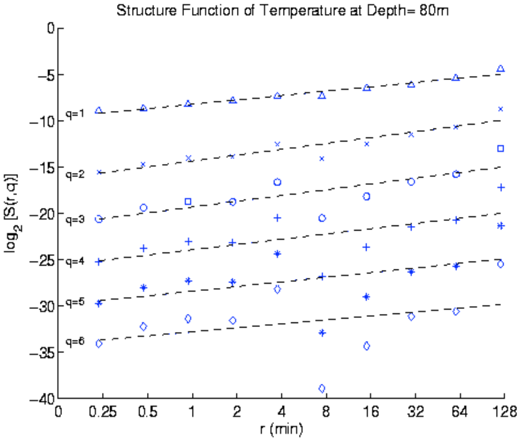
Structure Function of Temperature at Depth= 80m

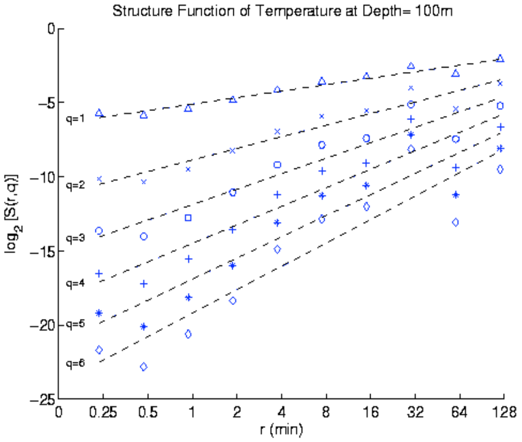
Structure Function of Temperature at Depth= 100m

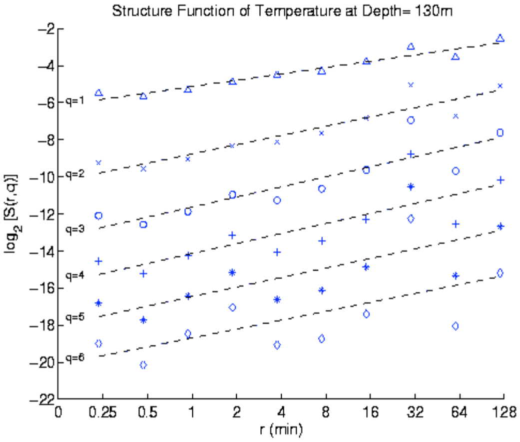
Structure Function of Temperature at Depth= 130m

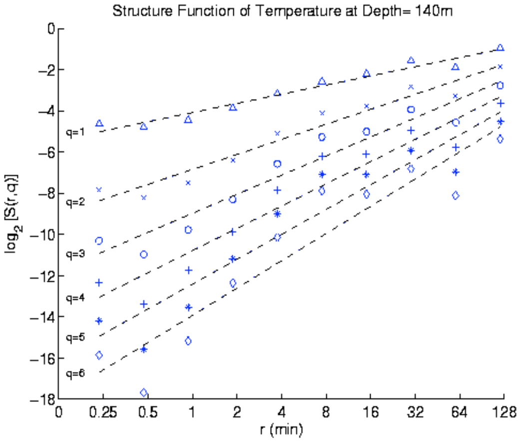
Structure Function of Temperature at Depth= 140m

APPENDIX D. SINGULAR MEASURE – TEMPERATURE

1. WAVE A

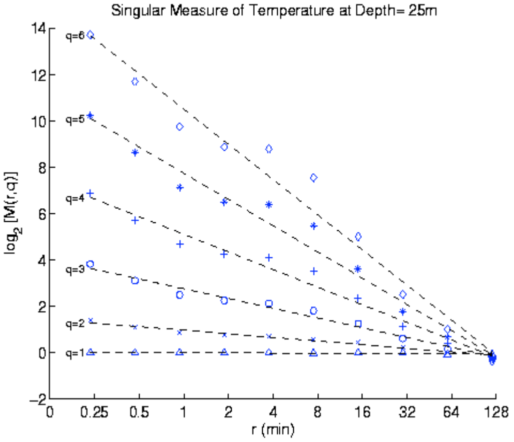

Singular Measure of Temperature at Depth= 25m

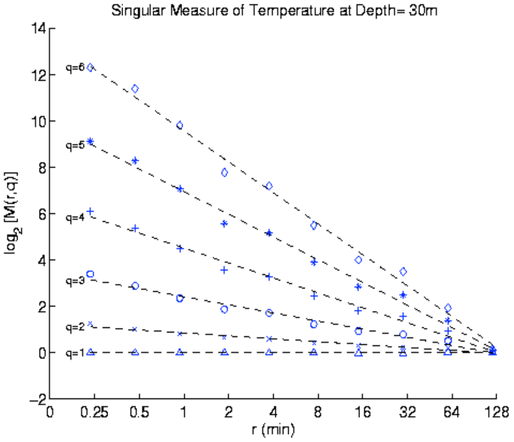

Singular Measure of Temperature at Depth= 30m

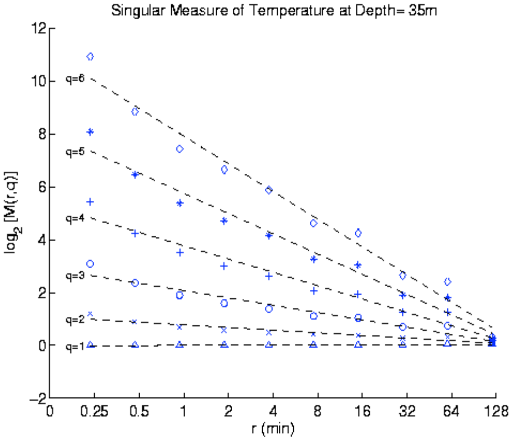

Singular Measure of Temperature at Depth= 35m

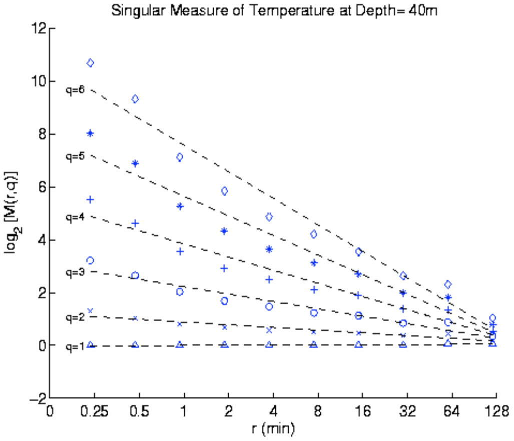

Singular Measure of Temperature at Depth= 40m

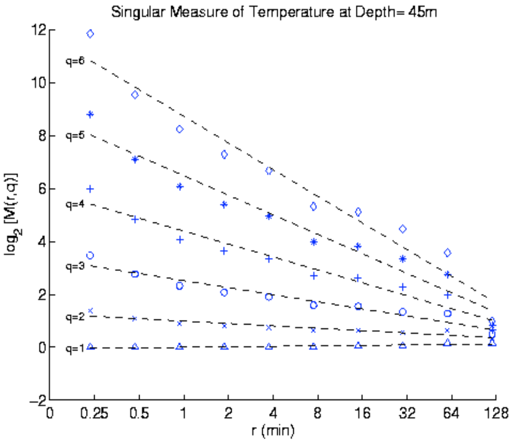

Singular Measure of Temperature at Depth= 45m

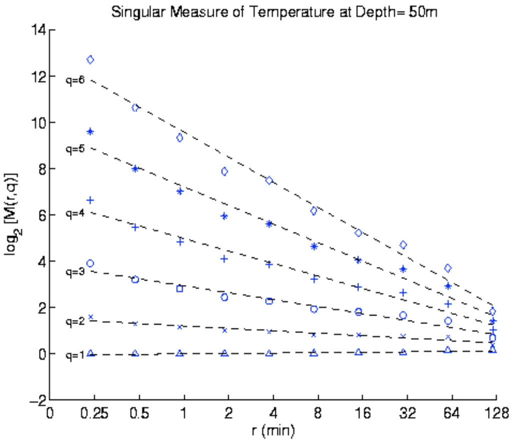

Singular Measure of Temperature at Depth= 50m

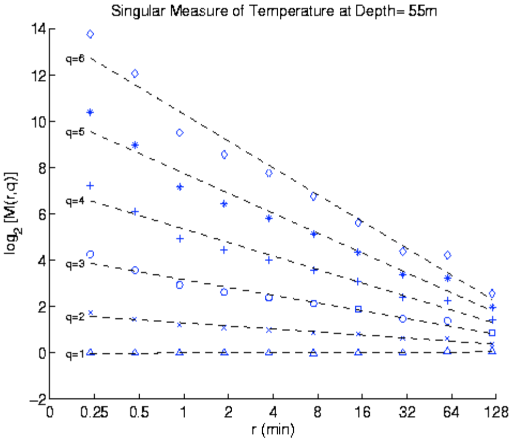
Singular Measure of Temperature at Depth= 55m
log$_2$ [M(r,q)]
r (min)
q=6
q=5
q=4
q=3
q=2
q=1
14
12
10
8
6
4
2
0
−2
0
0.25
0.5
1
2
4
8
16
32
64
128

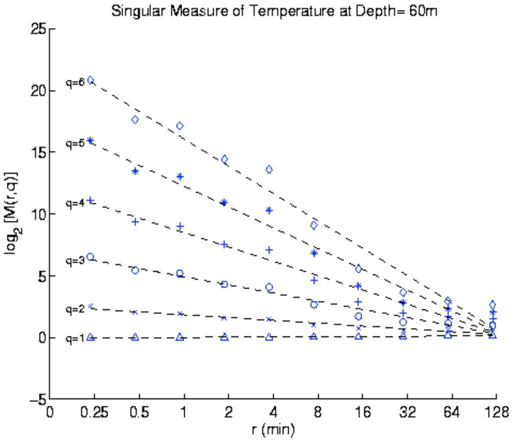
Singular Measure of Temperature at Depth= 60m
log$_2$ [M(r,q)]
r (min)
q=6
q=5
q=4
q=3
q=2
q=1
25
20
15
10
5
0
−5
0
0.25
0.5
1
2
4
8
16
32
64
128

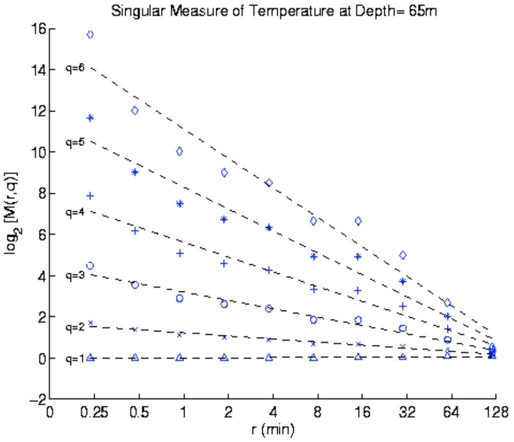
Singular Measure of Temperature at Depth= 65m
log$_2$ [M(r,q)]
r (min)
q=6
q=5
q=4
q=3
q=2
q=1
16
14
12
10
8
6
4
2
0
−2
0
0.25
0.5
1
2
4
8
16
32
64
128

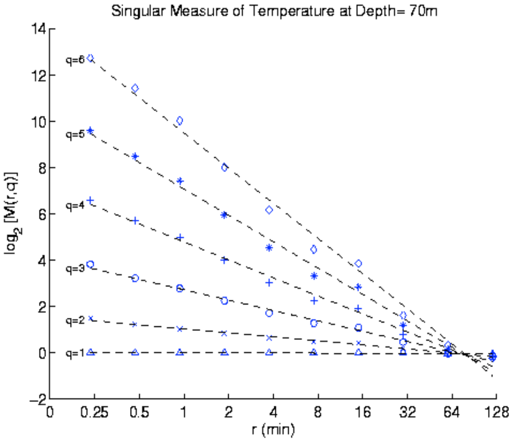
Singular Measure of Temperature at Depth= 70m
log$_2$ [M(r,q)]
r (min)
q=6
q=5
q=4
q=3
q=2
q=1
14
12
10
8
6
4
2
0
−2
0
0.25
0.5
1
2
4
8
16
32
64
128

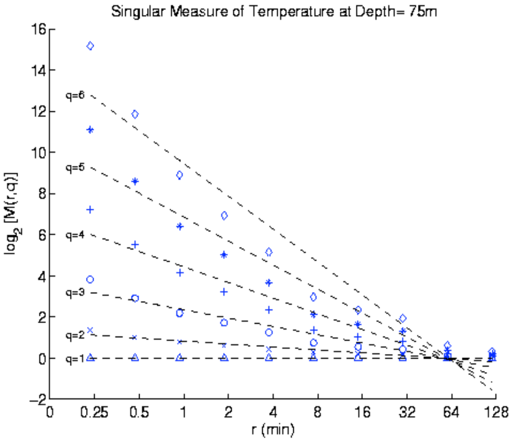
Singular Measure of Temperature at Depth= 75m
log$_2$ [M(r,q)]
r (min)
q=6
q=5
q=4
q=3
q=2
q=1
16
14
12
10
8
6
4
2
0
−2
0
0.25
0.5
1
2
4
8
16
32
64
128

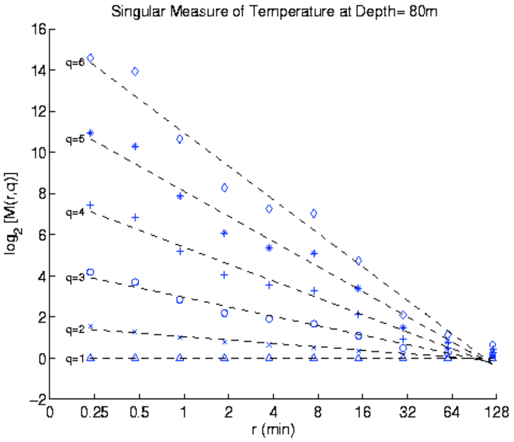
Singular Measure of Temperature at Depth= 80m
log$_2$ [M(r,q)]
r (min)
q=6
q=5
q=4
q=3
q=2
q=1
16
14
12
10
8
6
4
2
0
−2
0
0.25
0.5
1
2
4
8
16
32
64
128

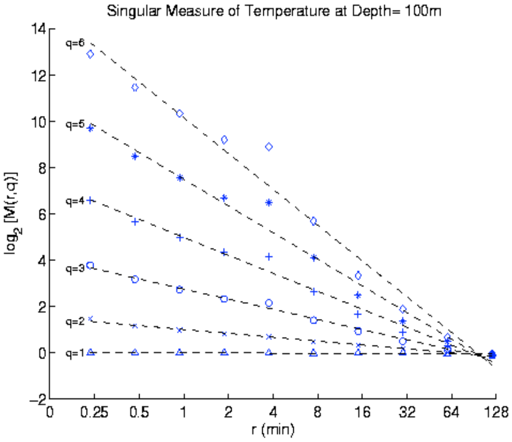
Singular Measure of Temperature at Depth= 100m
log$_2$ [M(r,q)]
r (min)
q=6
q=5
q=4
q=3
q=2
q=1
14
12
10
8
6
4
2
0
−2
0
0.25
0.5
1
2
4
8
16
32
64
128

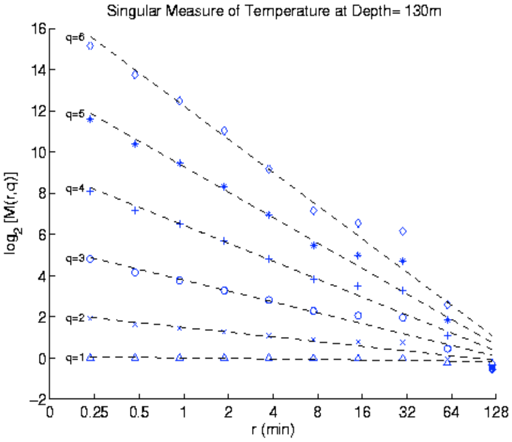
Singular Measure of Temperature at Depth= 130m
log$_2$ [M(r,q)]
r (min)
q=6
q=5
q=4
q=3
q=2
q=1
16
14
12
10
8
6
4
2
0
−2
0
0.25
0.5
1
2
4
8
16
32
64
128

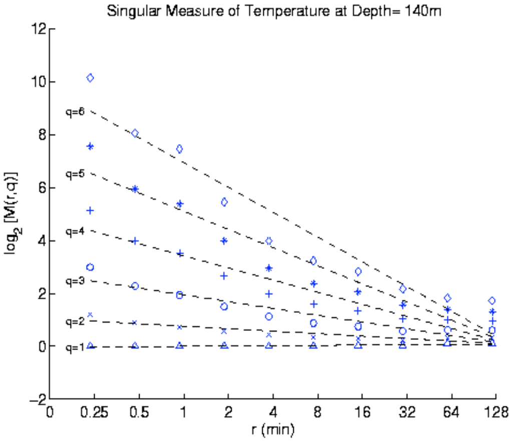
Singular Measure of Temperature at Depth= 140m
log$_2$ [M(r,q)]
r (min)
q=6
q=5
q=4
q=3
q=2
q=1
12
10
8
6
4
2
0
−2
0
0.25
0.5
1
2
4
8
16
32
64
128

2. WAVE B

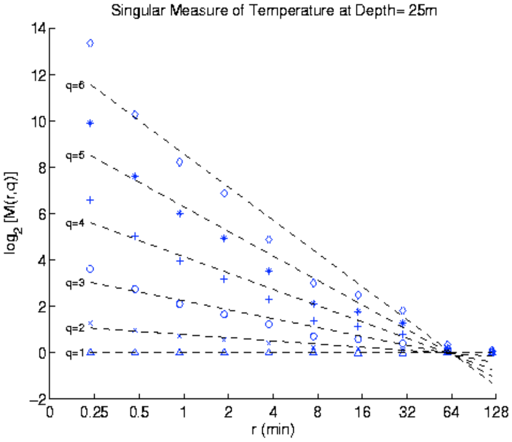
Singular Measure of Temperature at Depth= 25m

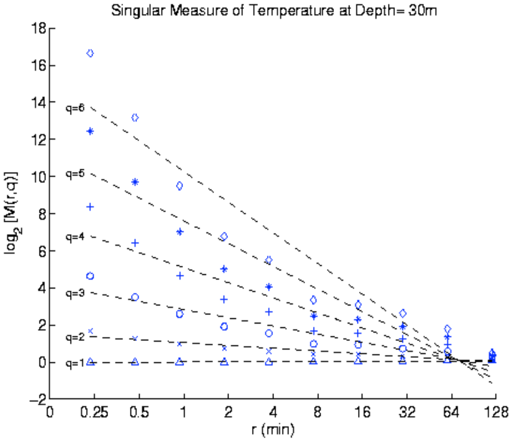
Singular Measure of Temperature at Depth= 30m

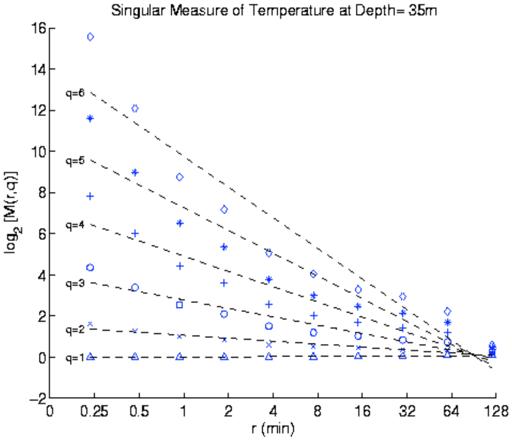
Singular Measure of Temperature at Depth= 35m

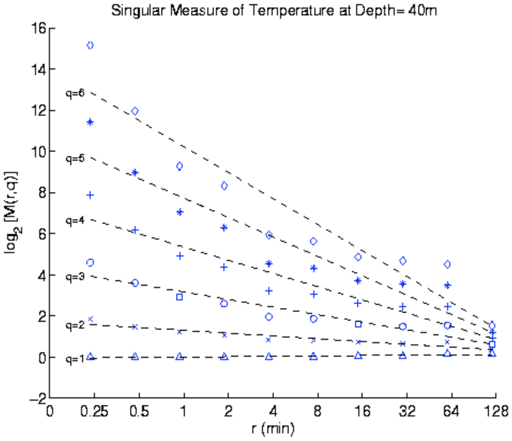
Singular Measure of Temperature at Depth= 40m

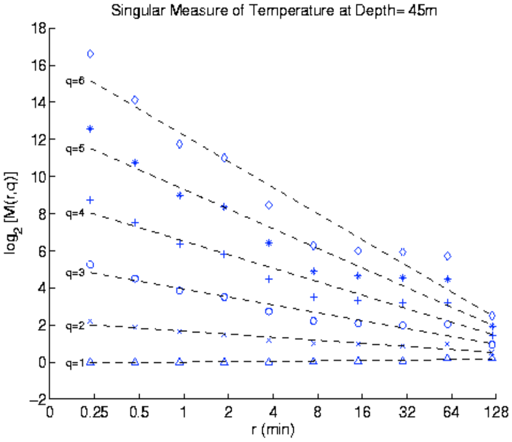
Singular Measure of Temperature at Depth= 45m

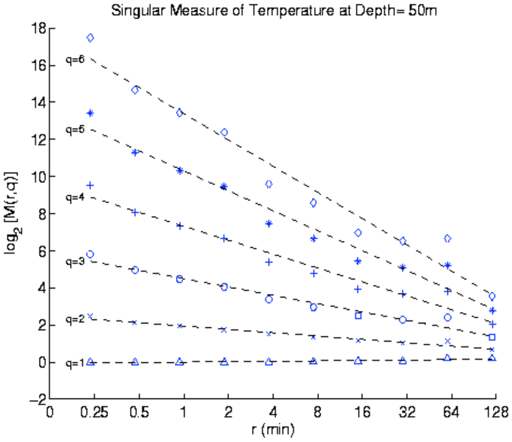
Singular Measure of Temperature at Depth= 50m

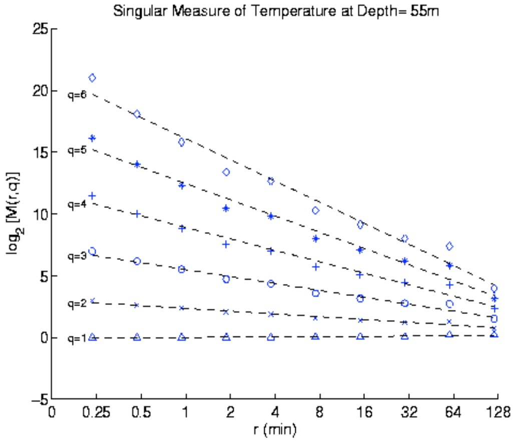
Singular Measure of Temperature at Depth= 55m

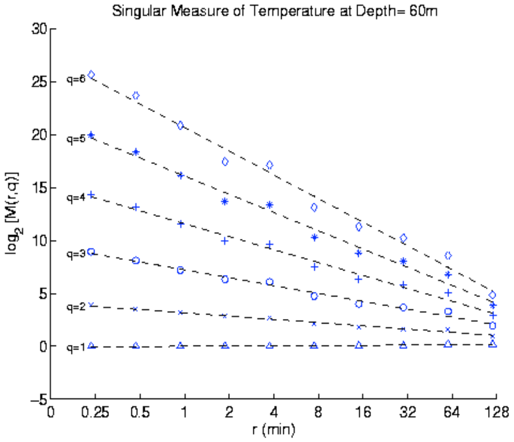
Singular Measure of Temperature at Depth= 60m

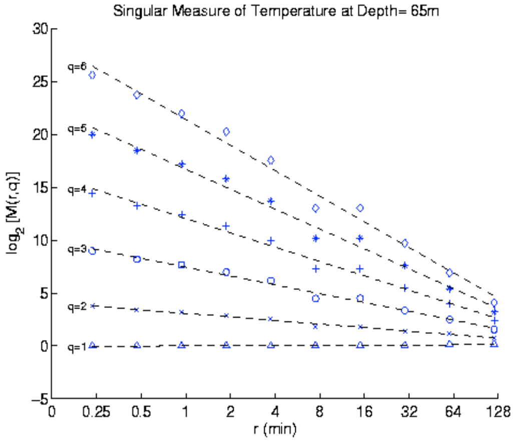
Singular Measure of Temperature at Depth= 65m

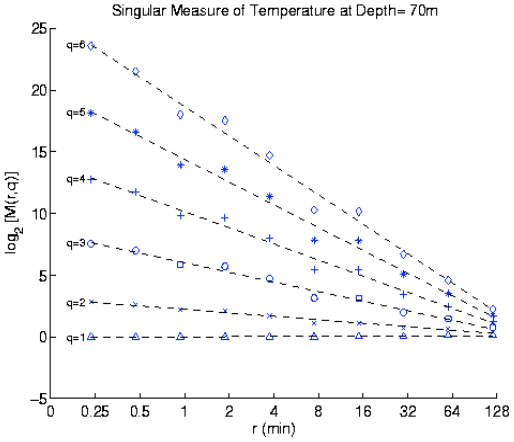
Singular Measure of Temperature at Depth= 70m

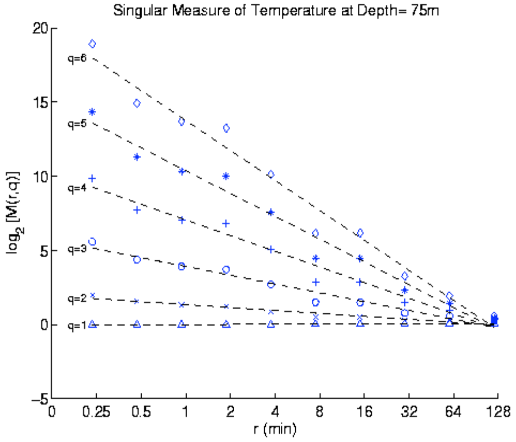
Singular Measure of Temperature at Depth= 75m

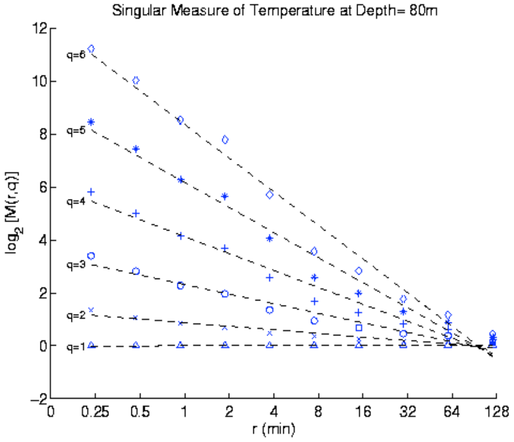
Singular Measure of Temperature at Depth= 80m

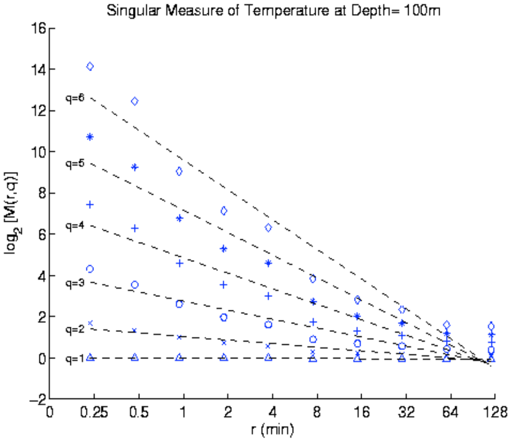
Singular Measure of Temperature at Depth= 100m
log$_2$ [M(r,q)]
r (min)
q=6
q=5
q=4
q=3
q=2
q=1
16
14
12
10
8
6
4
2
0
−2
0
0.25
0.5
1
2
4
8
16
32
64
128

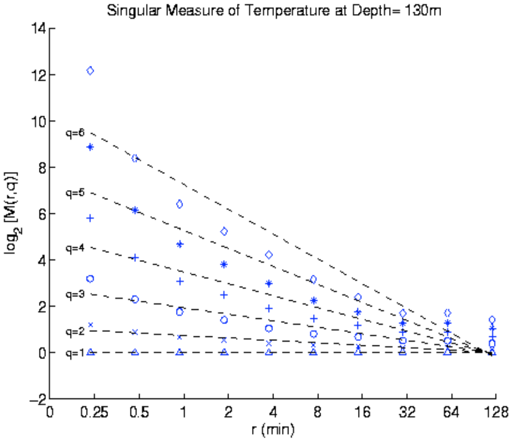
Singular Measure of Temperature at Depth= 130m
log$_2$ [M(r,q)]
r (min)
q=6
q=5
q=4
q=3
q=2
q=1
14
12
10
8
6
4
2
0
−2
0
0.25
0.5
1
2
4
8
16
32
64
128

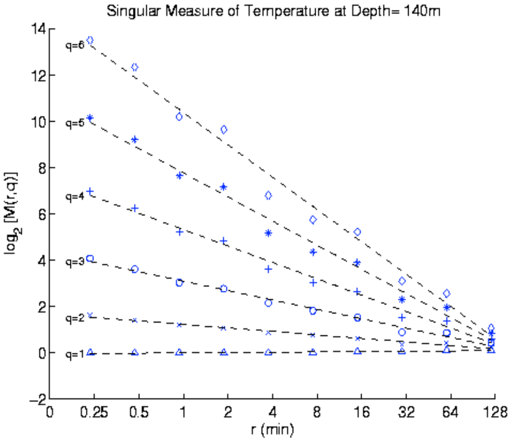
Singular Measure of Temperature at Depth= 140m
log$_2$ [M(r,q)]
r (min)
q=6
q=5
q=4
q=3
q=2
q=1
14
12
10
8
6
4
2
0
−2
0
0.25
0.5
1
2
4
8
16
32
64
128

3. WAVE C

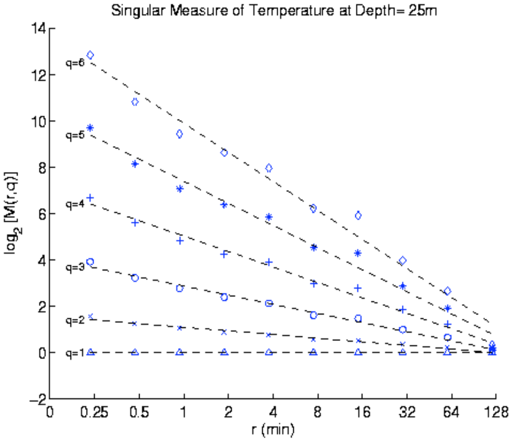
Singular Measure of Temperature at Depth= 25m
14
12
10
8
6
4
2
0
−2
log$_2$ [M(r,q)]
q=6
q=5
q=4
q=3
q=2
q=1
0
0.25
0.5
1
2
4
8
16
32
64
128
r (min)

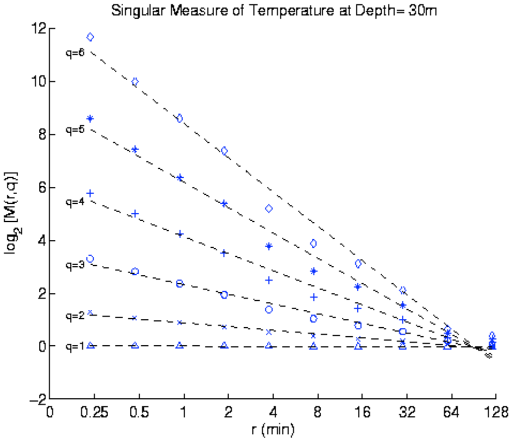
Singular Measure of Temperature at Depth= 30m
12
10
8
6
4
2
0
−2
log$_2$ [M(r,q)]
q=6
q=5
q=4
q=3
q=2
q=1
0
0.25
0.5
1
2
4
8
16
32
64
128
r (min)

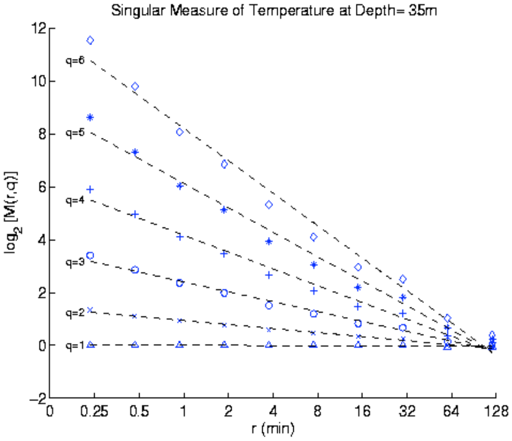
Singular Measure of Temperature at Depth= 35m
12
10
8
6
4
2
0
−2
log$_2$ [M(r,q)]
q=6
q=5
q=4
q=3
q=2
q=1
0
0.25
0.5
1
2
4
8
16
32
64
128
r (min)

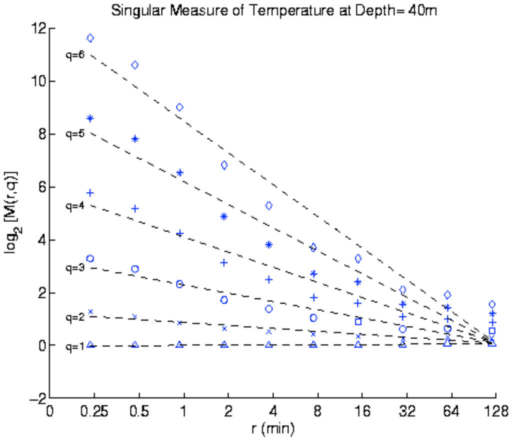
Singular Measure of Temperature at Depth= 40m
12
10
8
6
4
2
0
−2
log$_2$ [M(r,q)]
q=6
q=5
q=4
q=3
q=2
q=1
0
0.25
0.5
1
2
4
8
16
32
64
128
r (min)

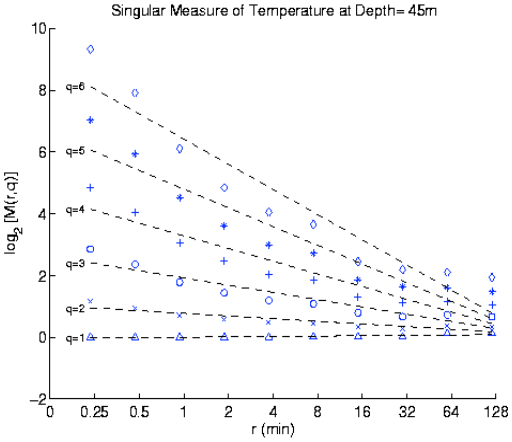
Singular Measure of Temperature at Depth= 45m
10
8
6
4
2
0
−2
log$_2$ [M(r,q)]
q=6
q=5
q=4
q=3
q=2
q=1
0
0.25
0.5
1
2
4
8
16
32
64
128
r (min)

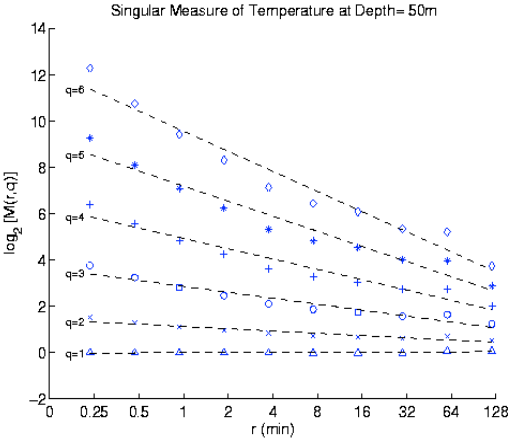
Singular Measure of Temperature at Depth= 50m
14
12
10
8
6
4
2
0
−2
log$_2$ [M(r,q)]
q=6
q=5
q=4
q=3
q=2
q=1
0
0.25
0.5
1
2
4
8
16
32
64
128
r (min)

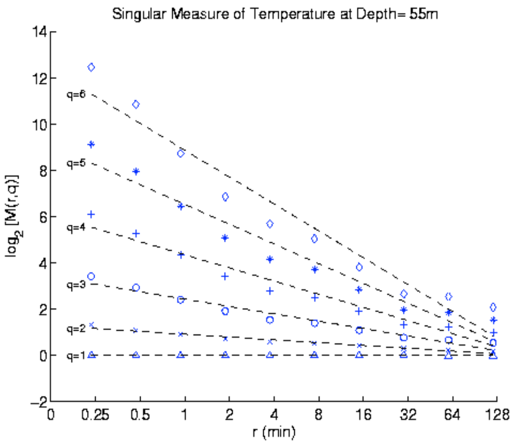
Singular Measure of Temperature at Depth= 55m
log$_2$ [M(r,q)]
r (min)
q=6
q=5
q=4
q=3
q=2
q=1
14
12
10
8
6
4
2
0
−2
0
0.25
0.5
1
2
4
8
16
32
64
128

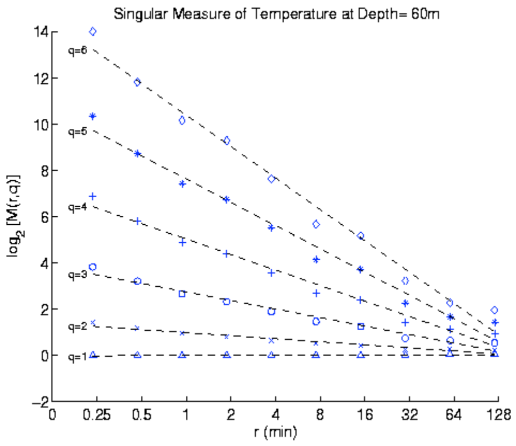
Singular Measure of Temperature at Depth= 60m
log$_2$ [M(r,q)]
r (min)
q=6
q=5
q=4
q=3
q=2
q=1
14
12
10
8
6
4
2
0
−2
0
0.25
0.5
1
2
4
8
16
32
64
128

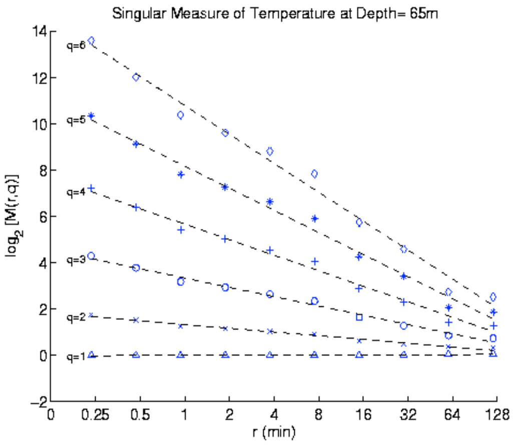
Singular Measure of Temperature at Depth= 65m
log$_2$ [M(r,q)]
r (min)
q=6
q=5
q=4
q=3
q=2
q=1
14
12
10
8
6
4
2
0
−2
0
0.25
0.5
1
2
4
8
16
32
64
128

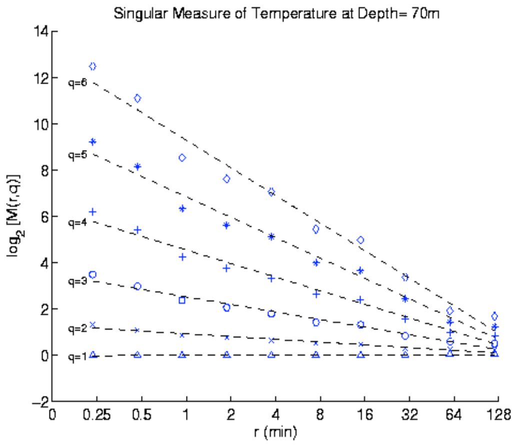
Singular Measure of Temperature at Depth= 70m
log$_2$ [M(r,q)]
r (min)
q=6
q=5
q=4
q=3
q=2
q=1
14
12
10
8
6
4
2
0
−2
0
0.25
0.5
1
2
4
8
16
32
64
128

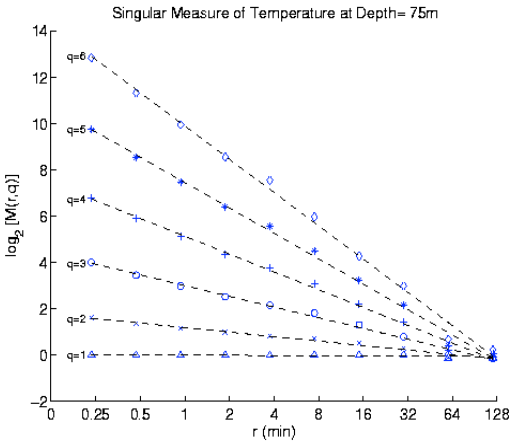
Singular Measure of Temperature at Depth= 75m
log$_2$ [M(r,q)]
r (min)
q=6
q=5
q=4
q=3
q=2
q=1
14
12
10
8
6
4
2
0
−2
0
0.25
0.5
1
2
4
8
16
32
64
128

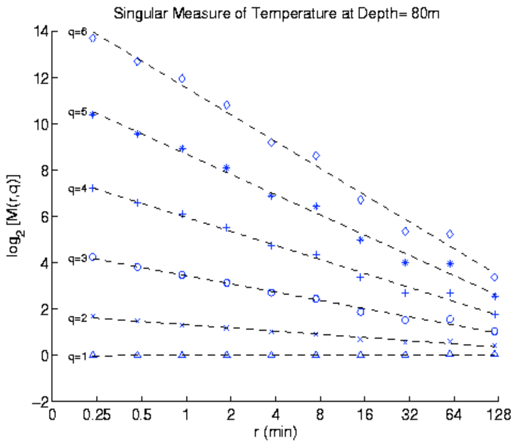
Singular Measure of Temperature at Depth= 80m
log$_2$ [M(r,q)]
r (min)
q=6
q=5
q=4
q=3
q=2
q=1
14
12
10
8
6
4
2
0
−2
0
0.25
0.5
1
2
4
8
16
32
64
128

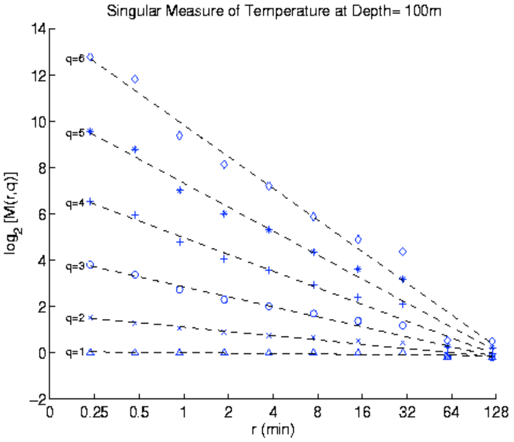
Singular Measure of Temperature at Depth= 100m
log$_2$ [M(r,q)]
r (min)
q=6
q=5
q=4
q=3
q=2
q=1
14
12
10
8
6
4
2
0
−2
0
0.25
0.5
1
2
4
8
16
32
64
128

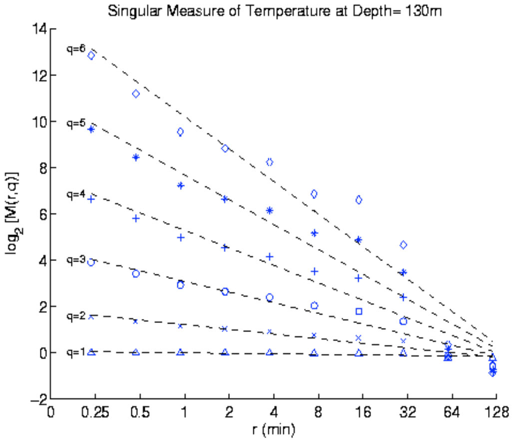
Singular Measure of Temperature at Depth= 130m
log$_2$ [M(r,q)]
r (min)
q=6
q=5
q=4
q=3
q=2
q=1
14
12
10
8
6
4
2
0
−2
0
0.25
0.5
1
2
4
8
16
32
64
128

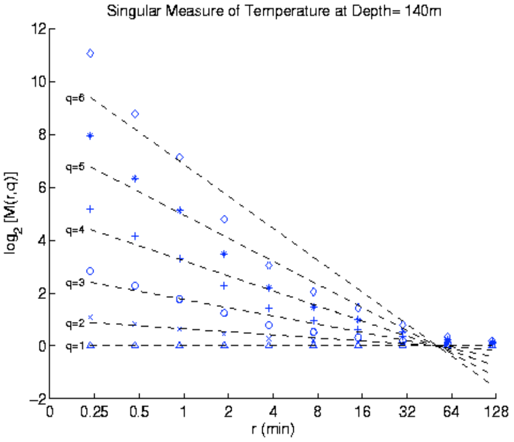
Singular Measure of Temperature at Depth= 140m
log$_2$ [M(r,q)]
r (min)
q=6
q=5
q=4
q=3
q=2
q=1
12
10
8
6
4
2
0
−2
0
0.25
0.5
1
2
4
8
16
32
64
128

4. WAVE D

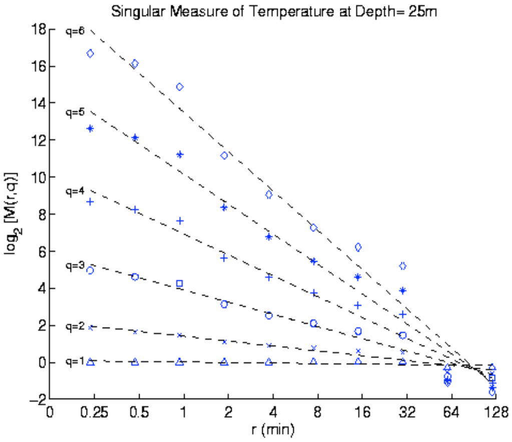
Singular Measure of Temperature at Depth= 25m

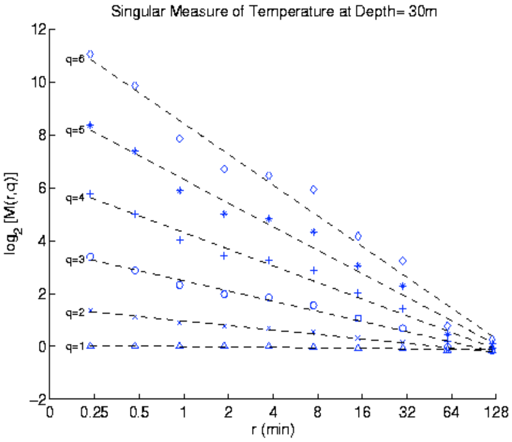
Singular Measure of Temperature at Depth= 30m

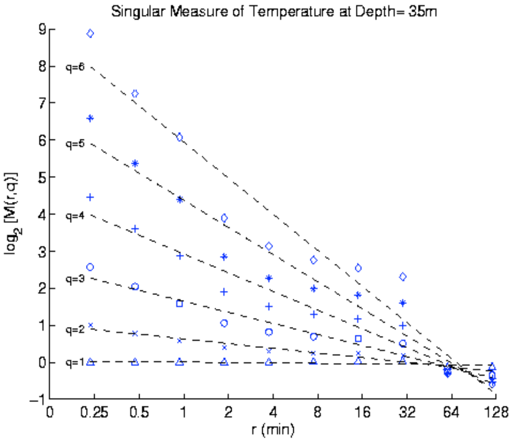
Singular Measure of Temperature at Depth= 35m

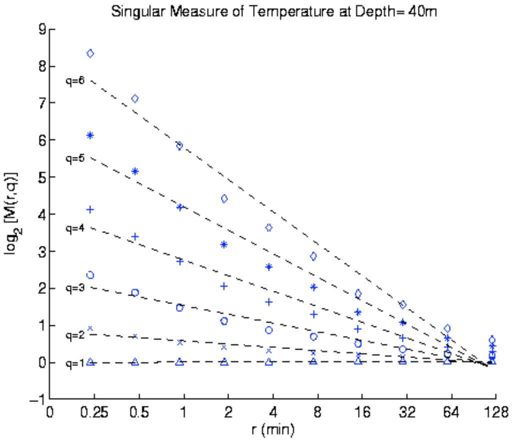
Singular Measure of Temperature at Depth= 40m

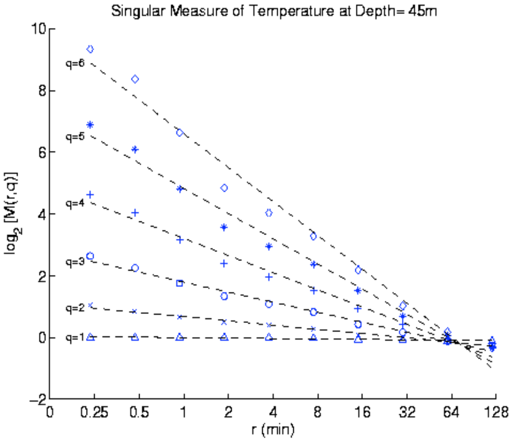
Singular Measure of Temperature at Depth= 45m

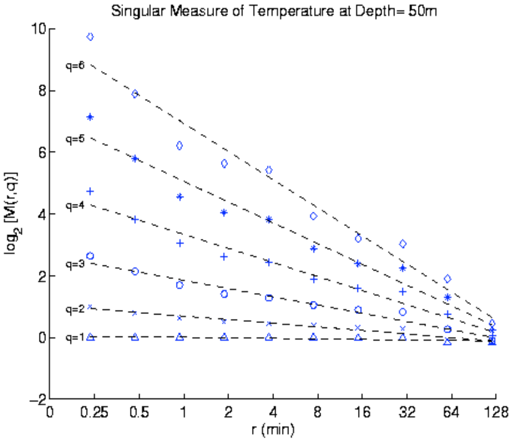
Singular Measure of Temperature at Depth= 50m

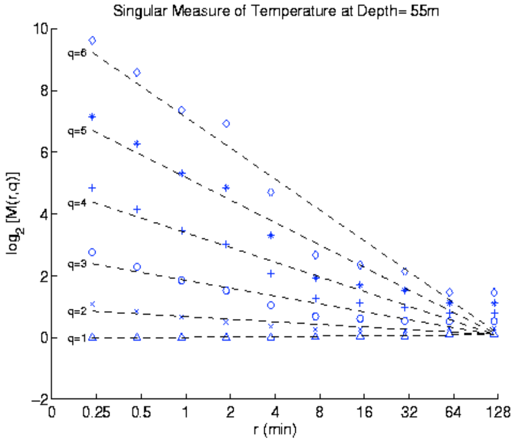
Singular Measure of Temperature at Depth= 55m

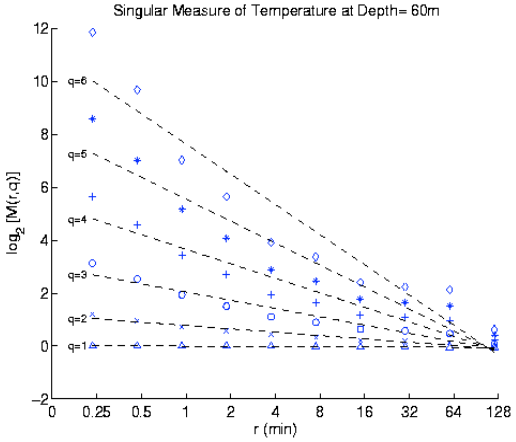
Singular Measure of Temperature at Depth= 60m

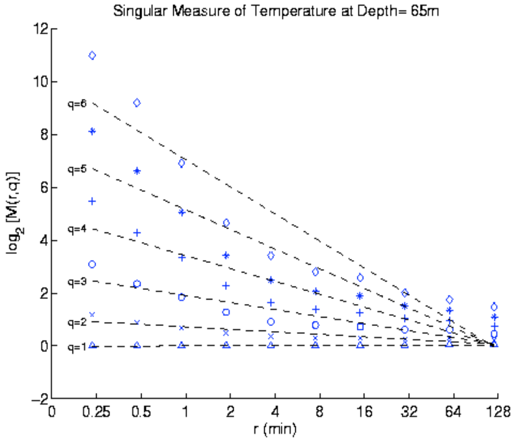
Singular Measure of Temperature at Depth= 65m

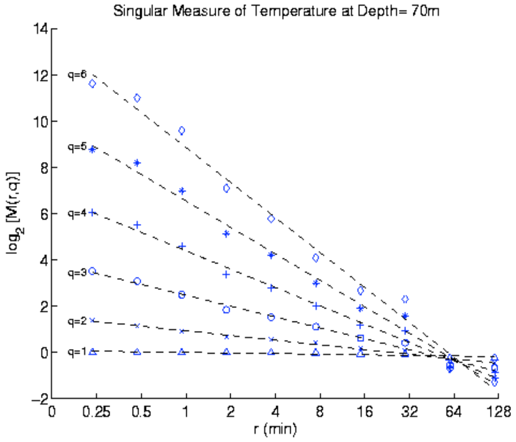
Singular Measure of Temperature at Depth= 70m

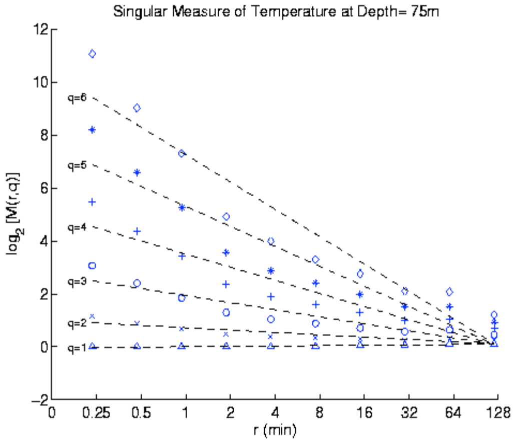
Singular Measure of Temperature at Depth= 75m

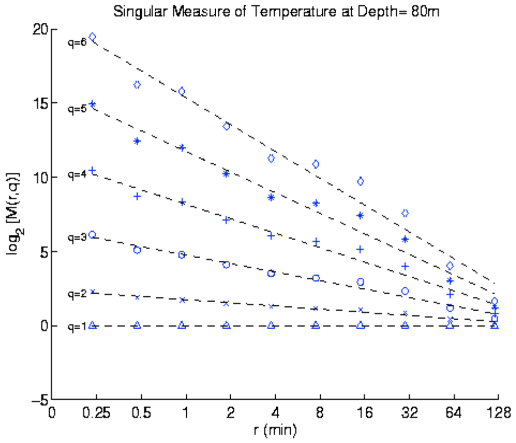
Singular Measure of Temperature at Depth= 80m

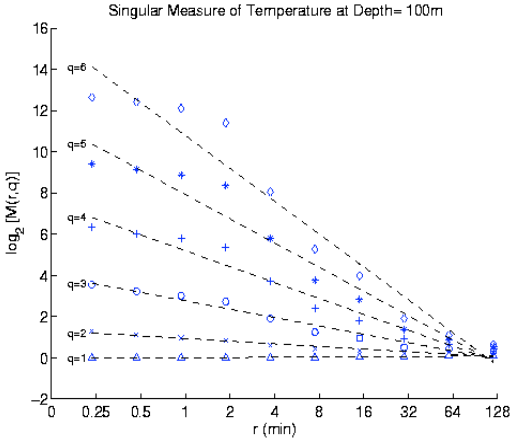
Singular Measure of Temperature at Depth= 100m
log2 [M(r,q)]
r (min)
q=6
q=5
q=4
q=3
q=2
q=1
16
14
12
10
8
6
4
2
0
−2
0
0.25
0.5
1
2
4
8
16
32
64
128

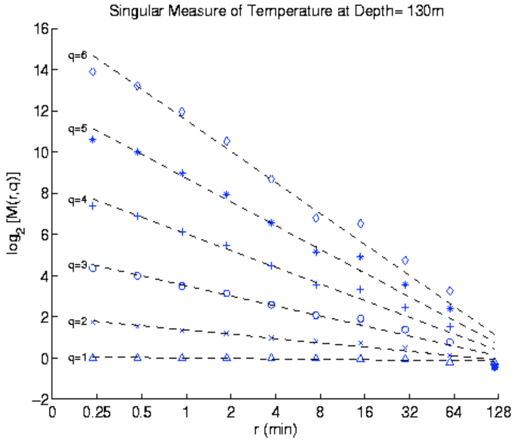
Singular Measure of Temperature at Depth= 130m
log2 [M(r,q)]
r (min)
q=6
q=5
q=4
q=3
q=2
q=1
16
14
12
10
8
6
4
2
0
−2
0
0.25
0.5
1
2
4
8
16
32
64
128

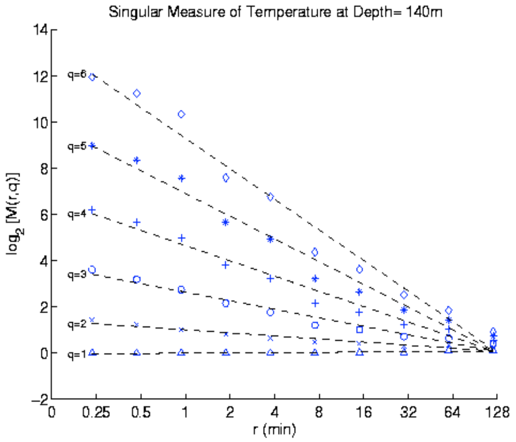
Singular Measure of Temperature at Depth= 140m
log2 [M(r,q)]
r (min)
q=6
q=5
q=4
q=3
q=2
q=1
14
12
10
8
6
4
2
0
−2
0
0.25
0.5
1
2
4
8
16
32
64
128

LIST OF REFERENCES

Aidala, F. E., Keenan, R. E., Weinberg, H., Modeling High-Frequency System Performance in Shallow-Water, Range-Dependent Environment with the Comprehensive Acoustic Simulation System (CASS), NUWC Division Newport Technical Digest, pp. 54–61, 1998.

Anstee, S., Use of Spherical Objects as Calibrated Mine Hunting Sonar Targets, Defense Technical Information Center Technical note, 2002.

Apel, J. R., Holbrook, J. R., Liu, A. K., Tsai, J. J., The Sulu Sea Internal Soliton Experiment.

Centurioni, L. R., Niiler, P. P., Lee, D. K., Observation of Inflow of Philippine Sea Surface Water into the South China Sea through the Luzon Strait, Journal of Physical Oceanography Vol. 34, pp. 113–121, 2004.

Chen, C.T., Huang, M. H., A Mid-Depth Front Separating the South China Sea Water and the Philippine Sea Water, Journal of Oceanography, Vol. 52, pp. 17–25, 1996.

Chotiros, N. P., Estes, J. M., Scarbrough, K. N., Pitt, S. P., Kilinksiek, R. V., Sonar Coverage Mapping, Application of Technology to Deming Part II Naval Mine Countermeasures, pp. 167–170, 2005.

Chu, P. C., Carlos C., Steven, D. H., Ruth, E. K., Acoustic Mine Detection Using the Navy's CASS/GRAB Model, Journal of Counter-Ordnance Technology (Fifth International Symposium Technology and Mine Problems), 2002.

Chu, P. C., Fan, C. W., Low salinity, cool-core cyclonic eddy detected northwest of Luzonduring the South China Sea Monsoon Experiment (SCSMEX) in July 1998, Journal of Ocenography, Vol. 57, pp. 549–563, 2001.

Chu, P. C., Li, R. F., South China Sea isopycnal surface circulation, Journal of Physical Oceanography, 30, 2419–2438, 2000.

Chu, P. C., Liu, Q. Y., Jia, Y. L., Fan, C. W., Evidence of a Barrier Layer in the Sulu and Celebes Seas, Journal of Physical Oceanography, Vol. 32, pp. 3299–3309, 2002.

Chu, P. C., Multi-fractal thermal characteristics of the southerwestern GIN sea upper layer. Chaos, Solitons and Fractals 19, pp. 275–284, 2004.

Chu, P.C., and Vares N. A., 2004: Uncertainty in Shallow Sea Acoustic Detection due to Environmental Variability. U.S. Navy Journal of Underwater Acoustics, 54, 347–367 (unclassified).

Dahl, P. H., Zhang, R., Miller, J. H., Bartek, L. R., Peng, Z. H. Ramp, S. R., Zhou, J. X., Chiu, C. S., Lynch, J. F. Simmer, J. A. Spindel, R. C., Overview of Results from the Asian Seas International Acoustics Experiment in the East China Sea, IEEE Journal of Oceanic Engineering, Vol. 29, No. 4, pp. 920–928,2004.

Global Ocean Associates, Oceanic Internal Waves and Solitons, An Atlas of Oceanic Solitary Waves, 2002.

Ikuo Kaneko, Yasushi Takatsuki, Hitomi Kamiya, Circulation of Intermediate and Deep Waters in the Philippine Sea, Journal of Oceanography, Vol. 57, pp. 397–420,2001.

Liu, A. K., Chang, Y. S., Hsu, M. K., Liang, N. K, Evolution of Nonlinear Internal Waves in the East and South China Seas, JGR, Vol. 103, No. C4, pp. 7995–8008, 1998.

Lium, A. K., Holbrook, J. R., Apel, J. R., Nonlinear Internal Wave Evolution in the Sulu Sea, Journal of Physical Oceanography, Vol. 15, pp.1613–1624, 1985.

Lynch, J. F. Ramp, S. R., Chiu, C. S., Tang, T. Y., Yanf, Y. J. Simmen, J. A., Research Highloght From the Asian Seas International Acoustics Experiment in the South China Sea, IEEE Journal of Oceanic Engineering, Vol. 29, No. 4, pp. 1067–1074, 2004.

Mandelbrot, B.B., 1982: The Fractal Geometry of Nature, pp. 460, W. H. Freeman, New York.

Mckinney, C. M., Acoustic Sensors For Minehunting, Application of Technology to Deming Part II Naval Mine Countermeasures, pp. 191–202, 2005.

Qu, T. D., Humio Mitsudera, Toshio Yamagata, A Climatology of the Circulation and Water Mass Distribution near the Philippine Coast, Journal of physical oceanography Vol. 29, pp. 1488-1505, 1998.

Qu, T. D., Humio Mitsudera, Toshio Yamagata, On the Western Boundary Currents in the Philippine Sea, JGR, Vol. 103, No. C4, pp. 7537–7548, 1998.

Rodriguez, O. C. Jesus, S., Stephan, Y., Demoulin, X., Porter, M. Coelho, E., Nonlinear Soliton Interaction with Acoustic Signals: Focusing Effects, Journal of Computational Acoustics, Vol. 8, No. 2,pp. 347–363, 2000.

Scarborough, K., Revesz, M., Thompson, M., Multiping Detection Performance Against Bottom Mines, Oceans ’02 MTS/IEEE, Vol. 3, pp. 1385-1393, 2002.

Shaw, P. T., The seasonal Variation of the Intrusion of the Philippine Sea Water into the South China Sea, JGR, Vol. 96, No. C1, pp. 8221–8228, 1991.

Sprintall J., Cronin, M. F., Upper Ocean Vertical Structure. In: J. Steele, S. Thorpe, and K. Turekian (eds.), Encyclopedia of Ocean Sciences, 2006.

Station, T. P., Ostrovsky, L. A., Observation of Highly Nonlinear Internal Solitons over the Continental Shelf, Geophysical Research Letters, Vol. 35, No. 14, pp. 2695–2698, 1998.

Su, J.L., and Lobanov, V. B., Eastern Asia, Kamchatka to the eastern coast of the Philippines coastal section (10, w). In The Sea, Vol. 11, the Global Coastal Ocean, edited by A. R. Robinson and K. H. Brink, John Wiley and Sons, Inc., New York, 415–427, 1998

Tubridy, L., Tactical Oceanography in Mines Countermeasures, Oceans ’02 MTS/IEEE, Vol. 3, pp. 1400–1406, 2002.

Urick, R. J., Principles of Underwater Sound for Engineers, McGraw-Hill, Inc, 1967.

Yves Desaubies, Gregg, M. C., Reversible and Irreversible Finestructure, Journal of Physical Oceanography, Vol. 11, pp. 541–556, 1981.

Zhou, J. X., Zhang, X. Z., Resonant interaction of sound wave with internal solitons in the coastal zone, Journal of the Acoustic Society of America, 90(4), pp. 2042–2054,1991.

THIS PAGE INTENTIONALLY LEFT BLANK

INITIAL DISTRIBUTION LIST

1. Defense Technical Information Center
   Ft. Belvoir, Virginia

2. Dudley Knox Library
   Naval Postgraduate School
   Monterey, California

3. Professor Mary L. Batteen
   Chairman, Department of Oceanography
   Naval Postgraduate School
   Monterey, CA

4. CDR James Berdeguez
   Chief of Naval Operations N75
   Washington, D.C.

5. Mr. Ronald E. Betsch
   Naval Oceanographic Office
   Stennis Space Center, MS

6. Professor Peter C. Chu
   Department of Oceanography
   Naval Postgraduate School
   Monterey, CA

7. Dr. Peter Fleischer
   Naval Oceanography Office
   Stennis Space Center, MS

8. CDR Eric Gottshall
   Office of Naval Research Global (ONRG)
   London, United Kingdom

9. Mr. Edward Gough
   Naval Meteorology and Oceanography
   Stennis Space Center, MS

10. CDR Van Gurley
    Naval Meteorology and Oceanography
    Stennis Space Center, MS

11. Mr. Steve Haeger
Naval Oceanography Office
Stennis Space Center, MS

12. CAPT Robert Kiser
Naval Meteorology and Oceanography
Stennis Space Center, MS

13. CDR Denise M. Kruse
Program officer USW/METOC/ECE/Applied Math
Naval Postgraduate School
Monterey, CA

14. Dr. Mike Richardson
Naval Research Laboratory
Stennis Space Center, MS

15. CAPT Chiu Peng Shiu
R.O.C. Navy
Kaohsiung, Taiwan (R.O.C.)

16. Dr. Philip Valent
Naval Research Laboratory
Stennis Space Center, MS

17. Dr. Linwood Vincent
Office of Naval Research
Arlington, VA

18. Mr. Melvin D. Wagstaff
Naval Oceanographic Office
Stennis Space Center, MS

19. Library
Chinese Naval Meteorological and Oceanographic Office
Kaohsiung, Taiwan (R.O.C.)